Structural modeling and computational mechanics of stingray inspired tesserae

vorgelegt von

M.Eng

Aravind Kumar Jayasankar

von der Fakultät III – Prozesswissenschaften
der Technischen Universität Berlin
zur Erlangung des akademischen Grades

Doktor der Ingenieurwissenschaften
– Dr. Ing. –

genehmigte Dissertation

Promotionsausschuss:
Vorsitzender: Prof. Dr. Dietmar Auhl
Gutachterin: Prof. Dr. Claudia Fleck
Gutachter: Prof. Dr. Dr. h.c. Peter Fratzl

Tag der wissenschaftlichen Aussprache: 15. Juli 2019

Berlin 2019

Abstract

Sharks and stingrays have a distinct skeletal system, which is predominantly made up of unmineralized cartilage, a material that is several orders of magnitude less stiff than the bone forming most vertebrate skeletons. The cartilage skeleton of sharks and rays is wrapped in a surface tessellation composed of minute polygonal tiles called tesserae, which are linked to each other by unmineralized collagenous fibers. The distinct combination of hard and soft tissues —and particularly the arrangements and structure of the tiled layer— is hypothesized to enhance the mechanical properties of this cartilage (which performs many of the same functional roles as bone) by providing either stiffness or flexibility, depending on the nature of the applied load.

This dissertation examines the effect of tesseral shape, ultrastructure and material properties on the mechanics of tessellated cartilage. In a first project phase, two-dimensional analytical models of arrays of different tile shapes (triangle, square and hexagon) surrounded by soft, fibrous joints were developed to evaluate the mechanical performance (effective modulus) of tessellations, as a function of their material and structural parameters. The two dimensional (2D) tiled composites were constructed from simple geometric shapes, and the overall composite effective modulus calculated by making a modification to the traditional Rule of Mixtures. The structural and material properties of joints (thickness, Young's modulus) and tiles (shape, area and Young's modulus) were altered to determine their effect on the mechanical performance of the whole composite. It was observed that for all shapes the effective modulus increases with decrease in joint thickness or increase of tile stiffness. Square tessellations were mechanically least sensitive and hexagons were most sensitive to changes in the modeled parameters. These observations indicate that mechanical performance (e.g. stiffness) of tessellated cartilage (and tiled composites in general) can be tuned and optimized through changes in joint and tile geometry and materials properties.

In a second project phase, three-dimensional (3D) tesserae were modeled with the ultrastructural features described in natural tessellated cartilage incorporated, and their mechanics evaluated using finite element analysis (FEA). Geometric aspects of these ultrastructural features were varied parametrically, and effective modulus of the whole

tessera was calculated. Some structural changes had no effect on tesseral stiffness, whereas an increase in contact surface area of two adjacent tesserae increased the effective stiffness of tesserae by 6%. It was observed that distinct hypermineralized features in tesserae (so-called 'spokes') experience maximum stress, but that their lamellated structure likely helps dissipate crack energy, making tesserae more damage-tolerant. Additionally, my models show that the tesseral center experiences high strain energy densities, suggesting that cells in this region in natural tesserae may be sensors of mechanical information. Building on my model of individual tesserae, modeled stress-strain curves of whole tesseral arrays show that changes in tesserae / joint shape and material properties can have pronounced effects on the mechanical behavior of the whole tiled composite. Maximum stresses in tension and compression occur in joints or within tesserae, respectively, supporting hypotheses of multi-functional properties of shark and ray tessellated cartilage.

The combined results of the two project phases are useful drivers of hypotheses regarding tesseral growth, mechanics, load management, prevention and 'directing' of cracks and tesseral contribution to cartilage mechanics. Further, these results lay a foundation for deriving guidelines and design principles for developing tunable tiled materials inspired from the tessellations found in shark and stingray skeletons.

Zusammenfassung

Haie und Stachelrochen haben ein besonderes Skelett das überwiegend aus nicht mineralisiertem Knorpel besteht, einem Material, dass um mehrere Größenordnungen weniger steif ist als Knochen im Skelett aller anderen Wirbeltiere. Dieses Knorpelskelett ist nur oberflächlich mineralisiert, eingehüllt in ein Mosaik aus winzigen polygonalen Kacheln, den sogenannten ‚Tesserae', die untereinander durch unmineralisierte Kollagenfasern miteinander verbunden sind. Erstaunlicher Weise erfüllt das so ‚gepanzerte Knorpelskelett', dieselbe Funktion wie sein viel härteres, knöchernes Pendant. Es wird angenommen, dass die spezifische Kombination von Hart- und Weichgewebe –insbesondere die Anordnung und Struktur von Tesserae– die mechanischen Eigenschaften des Knorpelskeletts verbessern indem je nach Art der Belastung (Druck oder Zug) entweder Steifigkeit oder Flexibilität erreicht wird.

In dieser Dissertation wird der Einfluss von Form, Ultrastruktur und Materialeigenschaften der Tesserae auf die Mechanik der oberflächlich gekachelten Skelettelemente untersucht. In einer ersten Projektphase wurden zweidimensionale (2D) analytische Modelle von Anordnungen unterschiedlicher Kachelformen (Dreieck, Quadrat und Sechseck) entwickelt, bei denen die einzelnen Kacheln durch flexible Gelenke miteinanderverbunden sind. Im Anschluss wurde das mechanische Verhalten (zB. Young's Modulus) der verschiedenen Verbundwerkstoffe in Abhängigkeit von ihren Material- und Strukturparametern bewertet. Der Elastizitätsmodul des Verbundwerkstoffs wurde dabei mit Hilfe einer Abwandlung der traditionellen ‚Rule of Mixtures' aberechnet. In den Experimenten wurden die Struktur- und Materialeigenschaften der Gelenke (zB. Dicke und Elastizitätsmodul) und der Kacheln (zB. Form, Fläche und Elastizitätsmodul) geändert, um deren Einfluss auf die mechanische Leistung des gesamten Verbundwerkstoffs zu bestimmen. In allen Modellen, unabhängig der Kachelform, nahm der effektive Elastizitätsmodul bei abnehmender Gelenkdicke oder zunehmender Steifigkeit der Kacheln zu. Jedoch im Vergleich der mechanischen Leistung waren Mosaike bestehend aus quadratischen am wenigsten bzw. sechseckigen Kacheln am meisten empfindlich gegenüber Veränderungen der modellierten Parameter. Diese Beobachtungen deuten darauf hin, dass die Steifigkeit von gekachelten Verbundwerkstoffen durch Änderungen der Kachel- und Gelenkform und deren Materialeigenschaften abgestimmt bzw. optimiert werden kann.

In der zweiten Projektphase wurden dreidimensionale (3D) Mosaiksteine mit ultrastrukturellen Merkmalen (abgeleitet von den Beschreibungen der natürlichen Tesserae) modelliert und ihr mechanisches Verhalten mittels Finite-Elemente-Analyse (FEA) analysiert. Zu den inneren Merkmalen der Tessserae zählen hochmineralisierte ‚Spokes' [ähnlich den Speichen eines

Rades] aufgebaut aus Lamellen, und ein homogenes Zentrum dessen Radius variiert. Geometrische Aspekte dieser ultrastrukturellen Merkmale (Lamellenanzahl und –dicke, Radius des homogenen Zentrums, und Gelenkkontaktfläche) wurden variiert (durch parametrisches Modellieren) und der effektive Elastizitätsmodul des Verbundwerkstoffes berechnet. Die Änderung der ‚Spoke'-Lamellenzahl und des Radius des homogenen Zentrums hatte keinen Einfluss auf die Steifigkeit der Tesserae, während eine Vergrößerung der Kontaktfläche von zwei benachbarten Tesserae deren effektive Steifigkeit um 6% erhöhte. Die maximale Spannung wurde innerhalb der Spokes beobachtet, in Form eines oszillierenden Spannungsmusters, aufgrund des periodisch variierenden Moduls der Lamellen. Ebenso nahm die Wellenlänge der modellierten Spannungsschwankungen mit zunehmender Lamellendicke ab. Letzteres unterstützt gängige Theorien, dass periodische Schwankungen der Materialeigenschaften in natürlichen Materialien dazu führen können die Ausbreitung von Rissen zu beeinflussen oder gar zu verhindern. Meine Modelle zeigen weiterhin, dass das Zentrum von Tesserae eine hohe Dehnungsenergiedichte aufweist, was darauf hindeuten könnte, dass die Zellen in dieser Region in den natürlichen Tesserae als Sensoren für mechanische Informationen fungieren. Aufbauend auf meinen individuellen Tessera-Modellen, zeigen modellierte Spannungs-Dehnungskurven zusammengesetzter Mosaike, dass Veränderungen der Größe von Tesserae und deren Gelenken sowie ihren Materialeigenschaften signifikante? Auswirkungen auf das mechanische Verhalten des Verbundwerkstoffs (des Mosaiks) haben. Maximale Zug- und Druckspannungen treten jeweils in den Gelenken bzw. in Mosaiksteinen auf und stützen somit Hypothesen über die multifunktionalen Eigenschaften des Mosaikknorpels von Haien und Rochen. Die kombinierten Ergebnisse der beiden Projektphasen bieten nützliche Daten für die Erstellung von Hypothesen über das Wachstum, dem mechanischen Verhalten unter Last, sowie der Prävention und Regulierung von Brüchen in Tesserae und ihrem Beitrag zum mechanischen Verhalten von oberflächlich gekachelten, knorpeligen Skelettelementen. Die hier gezeigten Ergebnisse bilden darüber hinaus die Grundlage für die Ableitung von Gestaltungsprinzipien für die Entwicklung artifizieller Kachellungen von 3D Objekten, die sich an den Tesserae-Netzwerken in Haifisch- und Rochenskeletten orientieren.

Table of Contents

1. Introduction

Man has continually looked to nature for inspiration, in disciplines as diverse as art, medicine, architecture, and engineering. Nature holds particular promise for engineering, having evolved mechanically- and energy-efficient structures, which can handle the complex mechanical functions posed by the organism(Barthelat and Zhu, 2011). For example, several natural structures such as honeycomb, trabecular bone, cuttle fish bone uses minimal material density yet the exhibit exemplary mechanical behavior, capable of absorbing high-energy impacts without failing (Yamashita and Gotoh, 2005). The ability of nature to produce such efficient composites with enhanced mechanical behavior lies in the combination of material and structural properties.

The skeletal system of vast majority of the vertebrates are made up of stiff bones, which provides rigid frame work for the organism, also they support in high load bearing activities of the animal such as locomotion and feeding. However the skeletal system of sharks and rays (elasmobranch fishes) consists predominantly of unmineralized cartilage (Dean et al., 2009b; Kemp and Westrin, 1979b; Seidel et al., 2016a), a skeletal tissue which is far less stiff than bone (Wegst and Ashby, 2004b), yet these cartilaginous skeletons are involved in high load-bearing activities, such as swimming, benthic locomotion along the seafloor, and feeding, even on very hard foods (Wilga and Motta, 2000). It is hypothesized that the distinct outer mineralized layer of the skeleton — comprised of a composite mix of soft fibrous material and minute, mineralized, polygonal tiles called tesserae (Dean and Schaefer, 2005; Dean et al., 2016; Kemp and Westrin, 1979b; Seidel et al., 2016a)— enhances the mechanical properties of the cartilage, (Fratzl et al., 2016a). In particular, the tessellation is believed to help manage loads (1) through the ultrastructural architectures and geometries of individual tesserae [Seidel, Knoetel] and (2) through the interaction of tesserae on a larger scale, allowing the skeleton to be either flexible or rigid, depending on the nature of the applied load (Liu et al., 2010a; Liu et al., 2014a). These mechanisms, however, had never been demonstrated explicitly in the actual tissue, nor in bio-accurate models.

The several previous studies, which explored the mechanics of tessellated cartilage, fell into one of two types, each with different limitations. On the one hand, there were

computational studies that assumed tesserae to be homogeneous blocks (Ferrara et al., 2011a; Wilga et al., 2016a), largely ignoring their natural variation in geometry, ultrastructure and material (Seidel et al., 2016a). On the other hand, several mechanics studies focused largely on the mechanics of whole skeletal elements (either through mechanical testing or finite element modeling) without considering the role of the tessellation. These limitations were likely due to two factors: (1) the intricate structure and minute size of tesserae (Seidel et al., 2016a), which make in situ tesserae-focused mechanical experiments very difficult to perform; and (2) the previous lack of information on tesserae ultrastructure and geometry, making the construction of accurate computational models difficult. As a result, the effect of tesserae shape and role played by the tesserae ultrastructure on cartilage mechanics were never investigated.

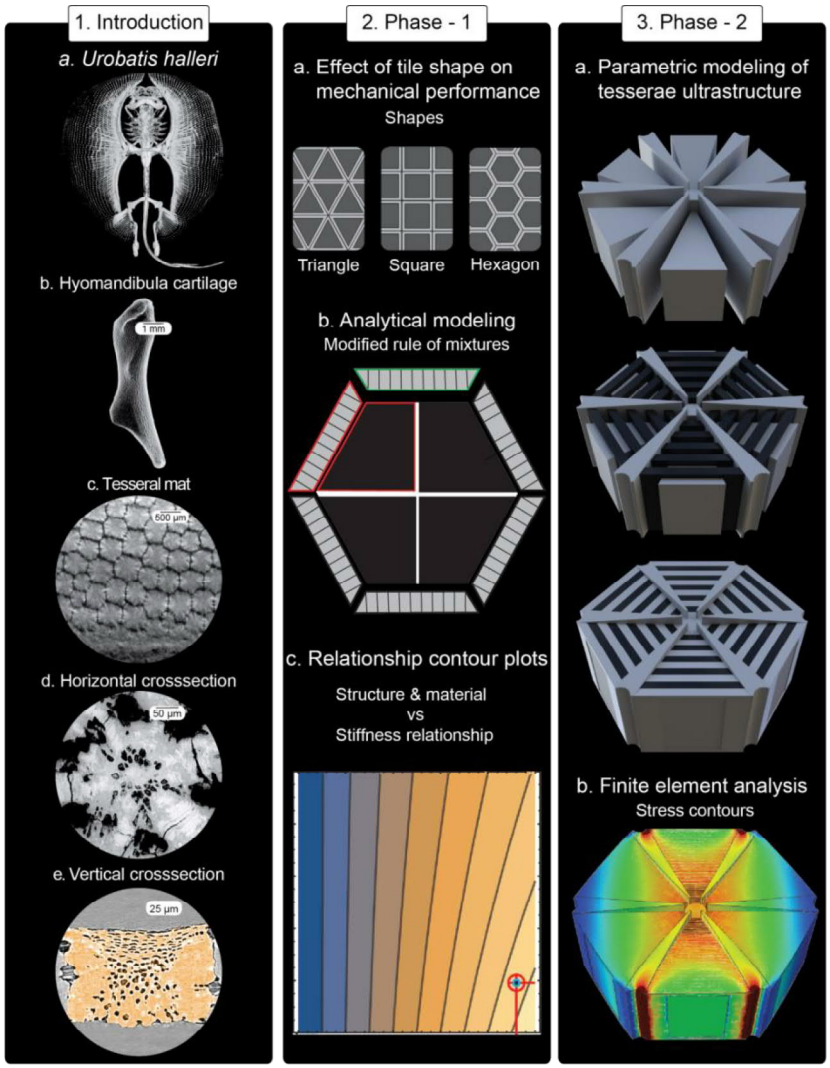

Figure 1: Visual summary of introduction and project phases of the dissertation.

Introduction panel: The tessellated cartilage of sharks and rays - moving from top to bottom, the magnification increases, showing the tesseral mat tiling the outside of the skeleton and then horizontal/vertical sections of tesserae, showing the intricate ultrastructure present in them (images 1.a to 1.c: microCT; d: scanning electron microscopy (SEM) and e: microCT). Phase-1: 2.a. Effect of tile shapes on the effective modulus of the composite. 2. b. The partitions are created on the tiled composites and subjected to the modified rule of mixtures. 2. c. The relationship between structure, material, and stiffness of the composite is derived using contour plots. Phase-2: 3. a. Stepwise parametric modeling of tesserae incorporating all the ultrastructural and material information. 3. b. By subjecting these models to finite element analysis, the stress information can be obtained to analyze the role of ultrastructure in tesserae and cartilage mechanics. (Images are reproduced with permission from (Jayasankar et al., 2017a; Seidel et al., 2016a)

This dissertation addresses, in two project phases, the role played by tesserae in contribution towards cartilage mechanics using mathematical modeling, parametric CAD modeling and computational structural mechanics. In the first project phase, two-dimensional analytical models of tesserae are developed, inspired from the tessellated cartilage of round stingray (*Urobatis halleri*), to observe the effects of tesserae shape, joint/tesserae size, and material properties on the mechanical behavior of the composite material. In the second project phase, the ultrastructural features of tesserae are incorporated into models, their features varied using parametric digital modeling techniques, and the simulated tissue responses to biologically-relevant loads quantified using computational structural mechanics. This second study, therefore will allow us to understand the effect of tesserae ultrastructure on the global mechanics of the tessellated cartilage.

The combined results of these studies will help in understanding the functional importance of the materials and morphologies observed in the tesserae of sharks and stingrays. Furthermore, they help in deriving hypothesis regarding the growth and development of this tissue, and the strategies evolved to prevent skeletal damage, while framing guidelines for the successful development of bio-inspired composites.

2. State of the art

2.1 Introduction to tilings

Tilings are surfaces subdivided into a continuous field of smaller elements that are geometrically congruent to their neighbors and with which they may interact to varying degrees (Oxman, 2010). Tilings are available everywhere around us, in natural systems like the patterns and scales of animal skin and manmade architectures like pavement on the streets. Tiling patterns from nature —and tessellations, a specific case where no gaps or overlaps exist in the tiling— have led many architects, artists and mathematicians to derive inspirations for their work (Schattschneider and Emmer, 2003). The use of architectural tiling patterns dates back to ancient civilizations in Egypt, Rome and Persia. Ancient Romans used tessellated mosaics to decorate their floors and also used square stones to pave their roads (Chang, 2018a; Chang, 2018b; Charbonnier and Cammas, 2016; Khaira, 2009). Tessellation patterns observed in nature inspired the Dutch graphic artist, M.C. Escher, to frequently use tessellations in his artwork (e.g. Fig. 1d) (Schattschneider and Emmer, 2003). Similarly, tessellations have intrigued many mathematicians, interested in understanding the role played by the geometry of shapes in tessellating a surface (Chang, 2018b; Deger et al., 2012). Thus tessellations are found widely in various art forms and engineering structures.

Apart from the aesthetic purpose of tessellations, they often play functional and mechanical roles as well. For example, the ancient Romans recognized that stone-paved roads had a functional advantage over roads with continuous surfaces. Whereas the latter tended to crack in extreme weather conditions and allowed cracks to propagate easily (Charbonnier and Cammas, 2016), the former would prevent crack propagation, due to cracks losing energy when they encountered a gap between two stone tiles in the road's discontinuous surface (Fratzl et al., 2007a; Fratzl et al., 2016a). Since Roman times the strategy of paving roads with stone tiles has been followed and can still be found in many countries in the world where they experience extreme weather conditions. As such, there are entire sub-disciplines in mathematics, topology and

architecture devoted to understanding the properties of tessellations and their ability to cover surfaces.

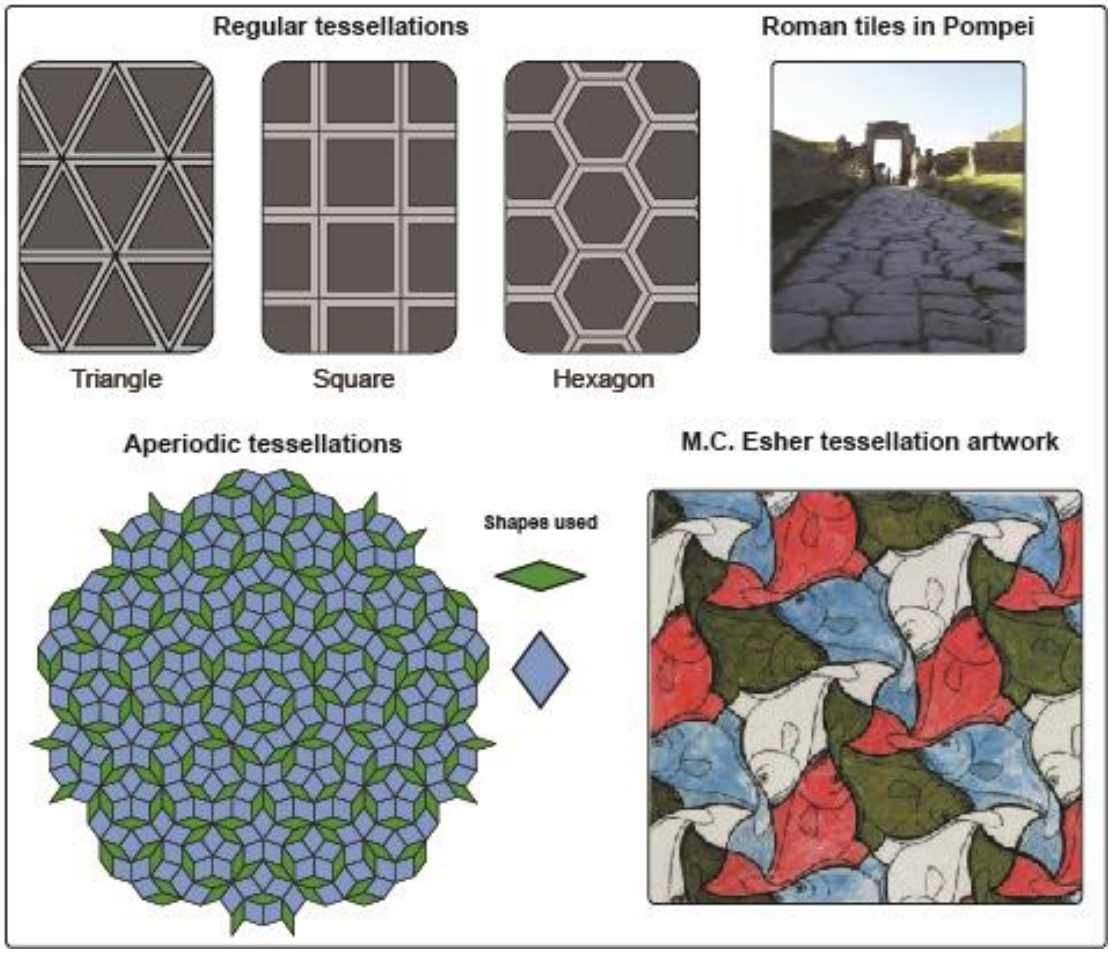

Figure 2: Classification of tessellations based on their symmetry.

a. Regular/periodic tessellations: triangle, square and hexagon where each polygon is surrounded identical polygon meeting at a vertex to vertex. b. Example to irregular/aperiodic tessellations in architecture where stone tiles are used to cover a street surface in an archeological site at Pompei, Italy. Reproduced with permission from (Charbonnier and Cammas, 2016). c. Penrose tessellation, an example of semi-regular/aperiodic tessellation where two or more polygons are combined to tessellate a surface. Reproduced with permission from (Soto, 2009). d. Example of M.C. Escher's artwork irregular/periodic tessellations in art. Reproduced with permission from (Schattschneider and Emmer, 2003).

Tessellations can be classified in a variety of ways, for example, based on their dimensions (either two- or three-dimensional tessellations) or their tile shapes (regular, semi-regular or irregular tessellations) or their tiling symmetry (periodic and aperiodic tessellations) (Chang, 2018b; Oxman, 2010). Regular tessellations are entirely made up

of identical regular polygons where all the polygons meet at vertex to vertex (Chang, 2018b). An example of regular tessellations patterns can be found in the square tilings on the bathroom floors (Chang, 2018a). The regular tessellations are shown in Fig. 1a. There are only three shapes, which can be used for regular tessellations and they are triangle, square and hexagon and they can tessellate in a periodic fashion. Based on the tiling symmetry the regular tessellations can be classified as periodic tessellations (Boots et al., 1999; Grunbaum and Shephard, 1977). Whereas the semi-regular tessellations are formed by two or more convex regular polygons are used and polygons of the same order surround each polygonal vertex. Semi-regular tessellations are aperiodic in nature and an example of aperiodic tessellation would be a Penrose tiling (it is an example of non-periodic tiling generated by an aperiodic set of prototiles)(Boots et al., 1999; Grunbaum and Shephard, 1977; Khaira, 2009; Oxman, 2010). The next classification by shape is irregular tessellation where any kind of geometrical shapes can be used to cover a surface (Boots et al., 1999). An ideal example would be Roman tiles in Pompeii as shown in fig. 1b. Even though there are further classifications of tessellations based on their symmetry, they are not discussed because they lie beyond the scope of this dissertation.

In this thesis, in order to make more intuitive the modelling of tessellations found in a natural system, I focus on the construction and mechanics of idealized tessellations that are regular and periodic.

2.2 Introduction to natural tilings

Natural tessellations and tilings are often associated with biological armors against predation and body damage or related to the locomotory mechanics of the animal (Chen et al., 2015a; Hosseini et al., 2018; Porter et al., 2017; Yang et al., 2013b; Yang et al., 2012). In this way, natural tilings offer interesting systems for exploring form-function relationships. The tessellations and tilings found in biology offer a mechanical advantage to organisms by combining protection/stiffness with flexibility, typically mutually exclusive properties (Achrai and Wagner, 2013a; Chen et al., 2015a; Liu et al., 2014a; Wang et al., 2016b; Yang et al., 2015). There are many examples of natural tilings in a variety of size scales from the micron-scale plates in the layers of nacre in mollusk shells

(Barthelat and Zhu, 2011), to the sub-millimeter mineralized tiles (tesserae) sheathing the cartilages of sharks and rays (Seidel et al., 2016a), to the macroscopic plates in the body armors of boxfish (Hosseini et al., 2018; Marcroft, 2015; Porter et al., 2017; Yang et al., 2015) and turtle shells (Chen et al., 2015a; Damiens et al., 2012; Krauss et al., 2009a; Rhee et al., 2009; Rivera and Stayton, 2011).

Most natural tessellations have not been classified in terms of the mathematical definitions for tessellations stated above (i.e. based on symmetry and dimensions). As a result, in this dissertation I build a new classification for natural tessellations and tilings with respect to common variation in structure and arrangement of tiles in organisms (Table 1). Relevant variables relate to the size of tiles, their arrangement and interaction (e.g. whether tiles overlap, interlock or are stacked on top of each other), the stiffness (Young's modulus) of the tiles, and the nature and modulus of the softer connections that anchor or link tiles (e.g. skin, collagen fibers) (Chen et al., 2015a; Gao and Li, 2019; Vernerey et al., 2014; Yang et al., 2015; Zhu et al., 2012). The hard and soft phase components present in the tiling architecture are listed along with the specific tile interface mechanism (e.g. in turtle shell the tile/hard phase is an osteoderm, the soft phase is comprised of collagen fibers, and the interaction between tile interface is called a suture interfaces (Chen et al., 2015a). Since there is not much data available for the soft phase component in these tilings but, because this phase often contains an appreciable amount of collagen, the Young's modulus of the soft component was assumed to be 0.05 GPa, similar to the modulus of boxfish collagen fibers in tension (Yang et al., 2015).

The ratio of tile/hard phase modulus to joint/soft phase modulus is plotted versus tile size in Fig. 2, to provide a perspective on the broader construction and mechanics of natural tiled systems. From the plot shown in Fig. 3 one can observe that the combination of hard and soft phases in tiling architecture plays a huge role in adding stiffness to the composite. It should be noted that the organisms with smaller tile size (e.g. nacre and millet) have higher modulus ratio when compared to the organisms with higher tile size (e.g., Glyptodon, Alligator). The decrease in modulus ratio is either due to the composite material composition and the structural arrangement within the tiles or ratio of size with respect to tile and the soft interface, (e.g., alligator osteoderms are comprised of a mix of collagens and mineral and have porous structure). This plot helps

in getting a general idea about how the combination of hard and soft phase in the composite and the possible mechanical roles they could contribute to the composite.

Animal	Organization	Subunit size μm	Tilings			Tile modulus GPa	Subunit : Interface Modulus ratio	Reference s
			Hard phase	Soft phase	Interface between hard and soft phase			
Glyptodon (Mammal)	Tilings	10^4	Osteoderm (Dermal bone)	Collagen fibers	Tethered w/ collagen fibers	5.2+	104*	(Wang et al., 2016)
Turtle (Reptile)	Tilings	10^4	Osteoderm (Dermal bone)	Collagen fibers	Wavy suture interlocking interface	20	400*	(Chen et al., 2015; Damiens et al., 2012)
Alligator (Reptile)	Tilings	10^4	Osteoderm (Dermal bone)	Collagen fibers	Tethered w/ collagen fibers	0.47	9.4*	(Chen et al., 2014; Yang et al., 2013)
Alligator gar (Fish)	Overlapping tilings	10^4	Scales (Ganoine + Dentin)	Collagen fibers	Attached to skin	5.2	104*	(Yang et al., 2013)
Pangolin (Mammal)	Overlapping tilings	10^4	Scales (Keratin)	Attached to skin	Attached to skin	1.5	30*	(Wang et al., 2016)
Armadillo (Mammal)	Overlapping Tilings	10^3	Osteoderm (Keratin)	Collagen fibers	Tethered w/ collagen fibers	0.43	8.6*	(Chen et al., 2011)
Bichir (Fish)	Over lapping tilings	10^3	Scales (Ganoine+ Dentin)	Attached to skin	Attached to skin using collagen fibers	17	340*	(Bruet et al., 2008; Yang et al., 2013)
Teleost fish scales	Over lapping tilings	10^3	Elasmoid scales (Dermal bone)	Collagen fibers	Attached to skin	1.2	24*	(Vernerey et al., 2014; Zhu et al., 2012)
Sharks and stingrays (Fish)	Tessellations	10^2	Tesserae (Calcified cartilage)	Collagen fibers	Tethered with collagen fibers	25	500*	(Ferrara et al., 2013; Seidel et al., 2016; Wroe et al., 2008)
Boxfish (Fish)	Tilings	10^2	Scutes (Dermal bone)	Collagen fibers	Interlocking toothed suture interface	15+	300*	(Yang et al., 2015)
Common millet seed (Plants)	Tilings	10^1	Epidermal cells (Silica)	Organic biopolymers (Yang et al., 2015)	Wavy suture interlocking interface	10	200*	(Hasseldine et al., 2017a)
Mollusc Shell Nacre	Stacked tilings	10^0	Polygonal tablets (Aragonite)	Protein and polysaccharide	Full overlap, stacked layers	70	1400*	(Meyers et al., 2008)

Table 1: Animals and a plant species classified in terms of the organization of tilings present in them.
The examples are arranged in the order of decreasing tile size, listing the name of the organism, the hard subunit (scales, osteoderms, scutes, epidermal cells and aragonite tablets) and the soft phase component (typically collagen). Reported material properties (Young's modulus) for hard phases are provided from literature or estimated based on similar tissues. The material properties of the soft phases in the examples for most examples are not available, and so the modulus for collagen fibers of boxfish armor is used (~0.05 GPa). From this a modulus ratio for hard vs. soft components are estimated. The symbol + denotes that the corresponding hard phase values are estimated based on other similar organisms.

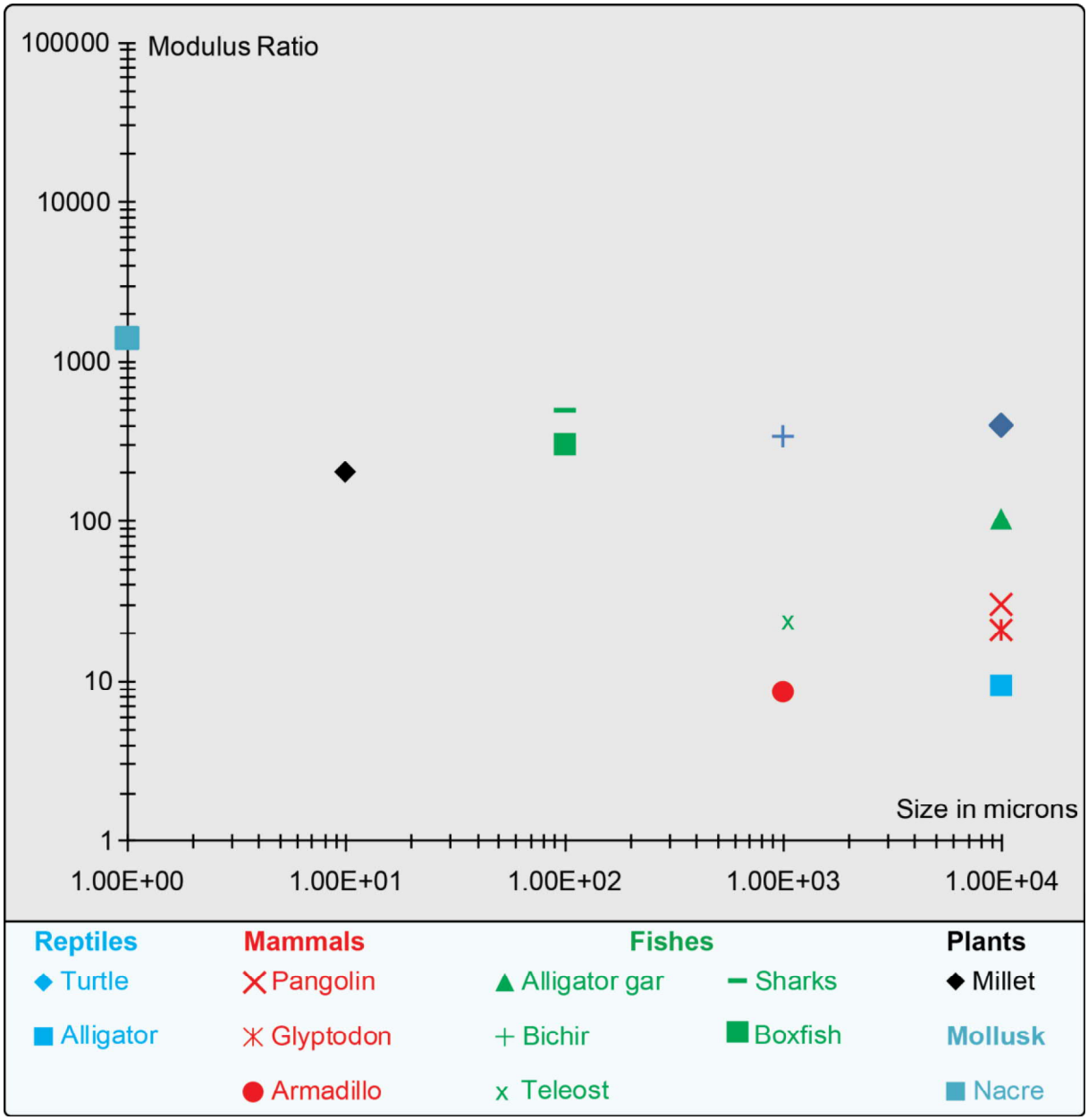

Figure 3: Plot showing the relationship between material property and size.

The plot shows the modulus ratios (hard modulus phase/soft phase) (y-axis) of various organisms and their corresponding size scale (x-axis) in microns. The organisms are classified as reptiles, fishes, mammals, and plants.

In the next section specific examples of natural tilings (turtle, boxfish and armadillo) are discussed. The sections deal with findings from previous studies, which analyzed the role played by the hard/soft phase and tile interfaces in the mechanics of the natural composite found in these animals. This gives more understanding in the context of form-function behavior of hard and soft components in these natural composites, while also

highlighting that natural tessellations often are characterized by interesting emergent properties (e.g. combinations of flexibility and stiffness).

2.3 Examples of biological tilings

2.3.1 Boxfish

Boxfish (*Lactoria cornuta*) belong to a family of fishes called the Ostraciidae, which includes trunkfish and porcupinefish. Members of the Ostraciidae are characterized by their boxy appearance and their bodies are defined by a carapace of rigid, external scutes. The boxfish's carapace exhibits a tessellation, which predominantly consists of hexagonal scutes (~78%) (Yang et al., 2015). The scutes interlock with each other at the triangular suture interfaces along their vertices and are tethered with each other using collagenous fibers as shown in Fig. 4 (Marcroft, 2015; Yang et al., 2015). The vertices push against each other and there by not allowing the scutes from sliding apart. The flexibility and resistance to predation (bite force of predators) of the boxfish scutes were tested by performing micromechanical tests involving tension and puncture. These tests are useful in observing failure of the scutes and it was observed that the failure primarily occurs in the collagen layers between scutes, rather than within the scutes themselves (Yang et al., 2015). Thus, scutes play a vital role in protecting the boxfish when it is subjected to sharp impact loads generated due to the bite forces of the predators.

Sutured interfaces are observed widely in many plant and animal species (e.g. Table 1) and the suture geometry were varied widely from simple triangular shaped sutures to complex wavy designs (Gao and Li, 2019; Lin et al., 2014b). In order to understand the effect of suture morphology on the mechanics of the structure, several studies analyzed the effect of suture shape on failure mechanisms (Li et al., 2011, 2012; Lin et al., 2014a; Lin et al., 2014b). Several suture designs (triangular, trapezoidal, anti-trapezoidal and rectangular) were analyzed using analytical models and 3D printed physical prototypes (Lin et al., 2014a; Lin et al., 2014b). On subjecting 3D printed prototypes to mechanical tension tests, triangular shape sutures demonstrated uniform distribution of tensile and tangential shear stress in the interface. The tangential forces enable the scutes to interlock with each other as shown in Fig. 4. In the case of boxfish scutes, the triangular

sutures are believed to resist penetration and crushing forces by predator's teeth (Li et al., 2011, 2012; Lin et al., 2014a; Lin et al., 2014b; Porter et al., 2017; Yang et al., 2015).

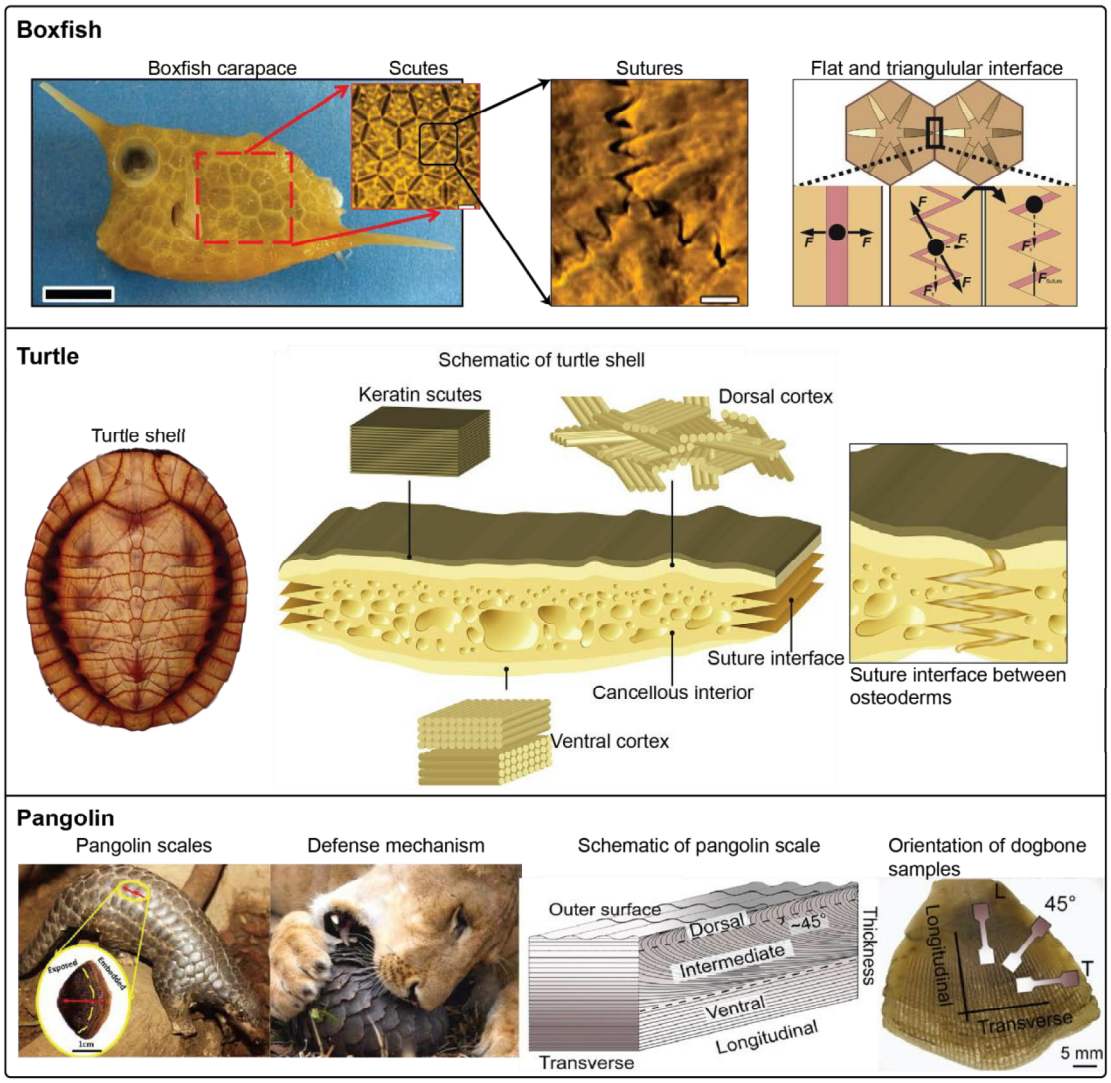

Figure 4: Examples of biological tilings

Boxfish: Triangular-sutured scutes on the carapace of boxfish. A theoretical comparison of forces acting on straight (left) and triangular suture interfaces (right) show that the latter leads to interlocking of scutes while the former leads to separation of scutes. Boxfish images are reproduced with permission form (Yang et al., 2015) Turtle: The schematic of turtle shell shows the architecture within the osteoderm and suture interface between these osteoderms. Images are reproduced with permission from (Achrai and Wagner, 2013b). Pangolin: Orientation of scale and defense mechanism of the pangolin. Pangolin curl into a ball when in danger, shielding their body and projecting their scales, which prevent the penetration of the predator's teeth. The schematic of the pangolin scale shows the orientation of lamellae distribution in the different regions within the scale. The fig. 4 shows orientations of dogbone samples in longitudinal and traverses orientations, which were used for mechanical testing. Pangolin images are reproduced with permission from (Liu et al., 2016; Wang et al., 2016b).

Thus the combination of hard tiles attached to each other using soft collagen creates a flexible armor that protects boxfish against predators and, aided by a triangular suture interface, the boxfish's scutes has higher resistance to penetration forces (Yang et al., 2015).

A hydrodynamic analysis of boxfish carapace was performed by fabricating 3D printed models of carapace shape and subjecting them to flow tank measurements (drag: the forces which resist forward motion) and it was validated with computational fluid dynamics. It was observed that due to the boxy shape, the carapace experiences destabilizing forces which in turn increases the drag experienced by the fish. However these destabilizing forces enable the boxfish to have better maneuverability (Marcroft, 2015; Porter et al., 2017; Van Wassenbergh et al., 2015). In this case, the tessellation of scutes not only adds protection but also, by forming a complex and boxy body form, enhances the maneuverability of the fish. The predominantly hexagonal scutes of the boxfish (Yang et al., 2015) suggest that scute geometry may play an important role in tessellation and mechanics of the surface. However, the effect of tile shape and the variation of material combinations on the mechanical performance of the biological composite were never investigated in this system.

2.3.2 Turtle shell

Turtle shells are tessellated by bony plates called osteoderms, which fit together to form a domed shield for the body. The shell protects the turtles from predatory attacks and a study performed on leatherback turtles showed that tessellations also provides a flexible surface for maneuverability (Chen et al., 2015a). The osteoderms comprise the dorsal side (carapace) and the ventral side (plastron) of the animal's shell (Achrai and Wagner, 2013a; Chen et al., 2015a; Krauss et al., 2009a). Each osteoderm is composed of a bone-like tissue consisting of collagen helices and hydroxyapatite nanocrystals, and the osteoderms are connected to each other by fibrous joints called sutures (Fig. 4) (Chen et al., 2015a; Krauss et al., 2009a; Rhee et al., 2009; Rivera and Stayton, 2011). At the sutural interface, adjacent osteoderms interlock through complex, zig-zagging tongue-and-groove architectures (e.g. a conical projection from one osteoderm fits into a conical cavity in the other), with osteoderms tethered together by collagenous fibrous material.

Several studies demonstrated the various mechanisms employed by turtle carapace to resist damage, crack propagation and failure. They employed mechanical testing methods and computational approaches to effectively understand the contribution of this tiling (effect of material, shape and structure) to the mechanical behavior of the turtle shell. The structural features were examined using scanning electron microcopy and micro-computed tomography and nanoindentation tests were performed (Chen et al., 2015a) (Achrai and Wagner, 2013a; Damiens et al., 2012). Nanoindentation experiments typically involve pushing a very small, hard tip (e.g. with a tip radius of hundreds of nanometers) into a material to examine hardness and elastic modulus at very small scales. The estimated structural and mechanical characterization of turtle carapace from nano-indentation showed that they are able to resist impact loads, and also designed to withstand sharp and blunt impacts (Achrai and Wagner, 2013a).

Suture morphology plays an important role in turtle's shell mechanics and it is important to note that the triangular suture interface provides a balance between tensile strength of the osteoderm and the shear strength of the connecting collagen fibers. This provides more flexibility to the shell in spite of its rigid component (osteoderm) (Chen et al., 2015a; Krauss et al., 2009a; Rivera and Stayton, 2011). The soft collagenous suture interface acts as a crack arrester, preventing cracks from passing from one hard osteoderm to another (Chen et al., 2015a; Fratzl et al., 2007a). Another study, simulating the compressive behavior of turtle shells showed that they undergo non-linear deformation behavior. The results from the turtle shell indicate that they are able to withstand high impact loads and yet they provide flexibility (Damiens et al., 2012). These studies indicate the turtle shell can be used as an inspiration for deriving guidelines for bioinspired structures, combining maneuverability and stiffness.

2.3.3 Pangolin scales

Pangolins are mammals, which have overlapping scales covering the majority of their skin and they are predominantly found in tropical and subtropical regions of Asia and Africa. In contrast to tessellations found in turtles and boxfish, the pangolin achieves flexibility and stiffness in the protective armor in the form of overlapping keratinous scales. The keratinous scales are arranged in such a way that each scale is in the center of neighboring scales arranged in a hexagon pattern (Chon et al., 2017; Liu et al., 2016;

Wang et al., 2016b). The arrangements of the scales are shown in Fig. 4 where for each scale the internal surface partially covers three lower scales and the external surface is partially covered by upper three scales (Wang et al., 2016b). When predators, threaten pangolins, as a defense mechanism pangolins curl up into a ball, protecting their bodies and projecting their hard- and sharp-edged scales outwards, thereby protect them against the sharp bites of predators' teeth (Fig. 4) (Chon et al., 2017; Liu et al., 2016; Spearman, 1967; Wang et al., 2016b; Yang et al., 2013b).

The material property and the arrangement of pangolin scales allow them to be both rigid and flexible. A scale of a pangolin can be divided into three different regions of lamellar arrangement throughout the scale's thickness. The ventral, intermediate and dorsal layers. In the ventral (bottom) region of the scale, the lamellae are parallel to each other and they are stacked with a tight curvature. In the intermediate layer the lamellar structure are parallel near the ventral region and the lamella asymptote when they approach the dorsal region (Liu et al., 2016; Wang et al., 2016b). The schematic of a pangolin scale is shown in Fig. 4 (Chon et al., 2017). In order to understand the effect of lamellar organization, indentation tests were performed on orientations with respect to scale growth and scale thickness directions (transverse and longitudinal orientations, shown in Fig. 4). Small dogbone samples were cut out from the whole scale in transverse and longitudinal orientations and subjected to mechanical testing methods like microindentation and tensile/compression testing, to test the effect of loading orientation on scale mechanics. In both orientations, scales showed similar microhardness, indicating an isotropic nature of the scale. Similar isotropic behavior was found in the tensile and compression tests for different orientations, in spite of the varied keratinous lamellae structure (Chon et al., 2017). Additionally, due to the viscoelasticity of the keratinous scales, the materials are stiffer and stronger at high loading rates, while capable of absorbing high energy at low strain rates (Wang et al., 2016b), thus making the pangolin scales a useful bio-inspiration for making armors against a variety of projectiles.

2.4 Introduction to mechanical modeling of tilings

The examples in the previous section demonstrated the tiling morphologies and mechanics in different organisms and the form-function relationships of natural tiled

composites. Many of these studies used analytical and computational models to understand the mechanics of the natural structures. The current section deals with analytical and computational modeling of natural systems and how they are used to interpret the mechanics and form-function relationships.

2.4.1 Analytical modeling

Analytical mathematical methods are valuable tools for testing form-function relationships in biology, particularly in their ability to simplify the complex structure of biological systems and estimate the effect of structural and material variables of the system on the overall mechanics. Such methods are also useful in choosing an optimal model for fabrication and further mechanical testing especially when the fabrication costs are high. Additionally, mathematical methods can be used to build hypotheses of mechanical performance even in the absence of detailed structural and material information, through the exploration of the effects of ranges of properties/morphologies.

For example, the sutural interfaces in various seed coats of millet seed, turtle osteoderms, and boxfish scutes exhibit a wide degree of structural variations (Gao and Li, 2019). Mathematical models of the sutures were developed to understand their contribution to overall stiffness, strength and fracture toughness of the composite (Gao and Li, 2019; Hasseldine et al., 2017; Li et al., 2011, 2012), by introducing variations in sutural structure/morphology and its material property. For example, in an examination of turtle osteoderms, the suture's morphology was varied and the performance of a hypothetical rectangular suture was compared to that of the natural triangular suture to understand their contributions to osteoderm mechanics (Chen et al., 2015a). It was found that the triangularly shaped sutures have maximum strength when compared to rectangular shaped suture teeth (Chen et al., 2015a).

Similar triangular sutures are also found in the interfaces of boxfish scutes and they are dimensionally different when compared to the sutural structures found in turtles. The boxfish scutes have wavy sutures in larger wavelengths with smaller angles at the intersection of triangle sides at the suture interface. Wavy suture interfaces has higher resistance to the bite force of the predators when they were compared with the

hypothetical model with a straight interface (Porter et al., 2017; Yang et al., 2015). As observed in Fig. 4, when a sharp tooth enters a flat interface, the force exerted will separate the scutes whereas in the triangular suture interface, the force exerted will cause the scutes to interlock with each other. Thus scutes with triangular sutures can resist inter-scute penetration better than a straight interface (Yang et al., 2015). Thus the triangular suture interface plays an essential role in creating an interlocking mechanism between the scutes and preventing the failure of the composite (Yang et al., 2015).

Furthermore there are complex sutural structures in seed coats of common millet, where the hard epidermis cells are articulated with wavy intercellular sutures to form a compact layer to protect the kernel inside, as shown in Fig. 5 (Gao et al., 2018; Gao and Li, 2019; Li et al., 2011). In order to evaluate the mechanical properties of the seed coat, an analytical model was developed with a two-phase composite, involving a hard phase (epidermal cell) and soft intercellular suture layer (Gao et al., 2018; Gao and Li, 2019; Hasseldine et al., 2017). In this analytical model, structural dimensions were varied with respect to suture morphology (wavelength and amplitude of suture) and evaluated using constitutive equations, allowing easy variation of sutural morphology for hypothesis testing (Gao et al., 2018; Hasseldine et al., 2017). The constitutive equations also allow estimation of the material properties of the whole seed coat, which can be further used in computational analysis (Hasseldine et al., 2017). Analytical models predicted that the waviness of the sutural interface also plays an essential role in protecting the kernel by resisting the loads in different directions (Hasseldine et al., 2017).

Although analytical models allow us to perform quick estimation of mechanical behavior, however, they have their drawbacks. Analytical models cannot consider all the biotic (e.g., internal forces acting within the organism) or abiotic parameters (e.g., environmental pressure, temperature), which an organism experiences in nature. However analytical models provide useful estimates and validation for experimental testing and computational modeling. In many cases, however, experimental testing is challenging or impossible, especially if an organism or its tissues have complex structure. This is where computational structural mechanics like finite element analysis can be useful and this is discussed in the section below.

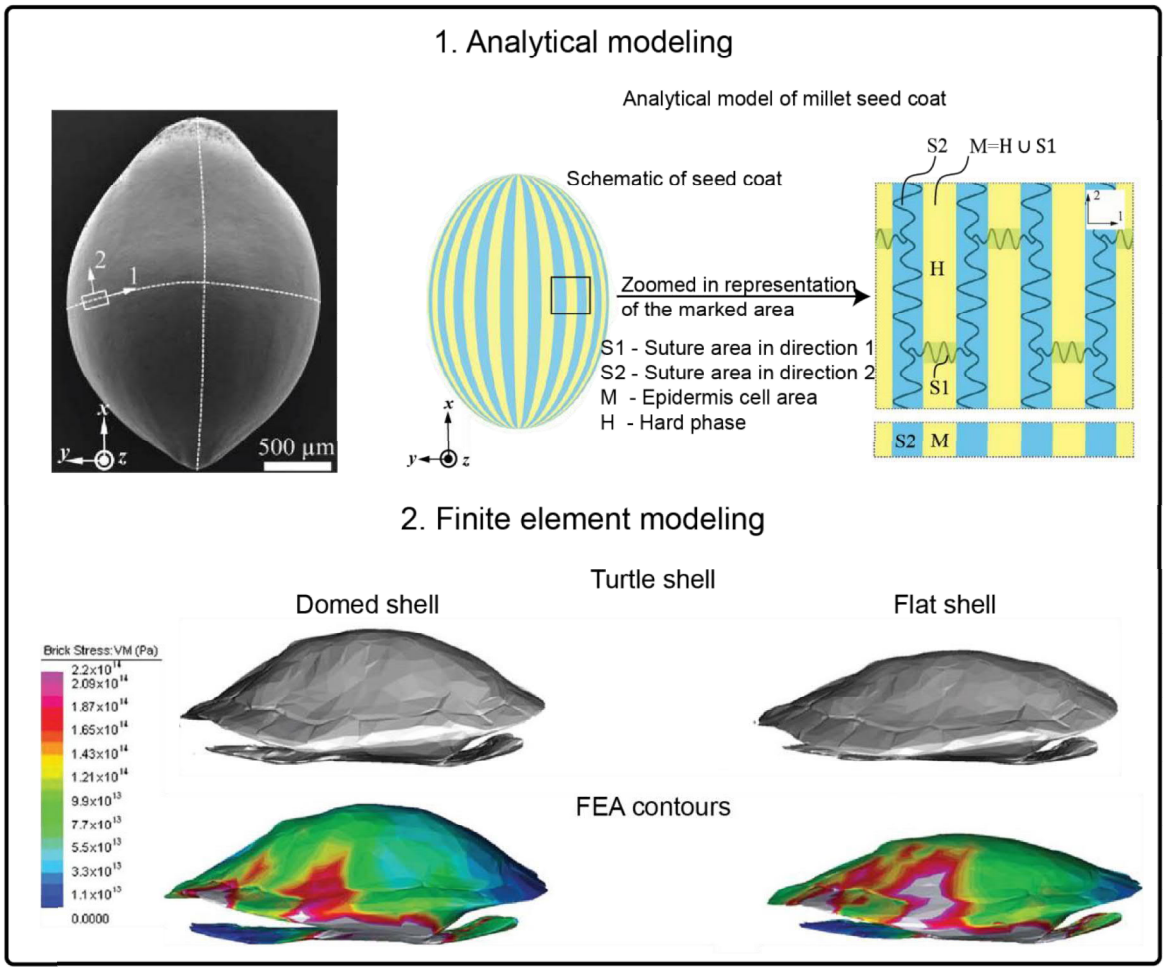

Figure 5: The Fig. shows examples of analytical modeling and finite element modeling.

1. SEM image of a common millet (*Panicum miliaceum*) seed with seed coat. The analytical model of a millet seed coat developed with material and structural features. The zoomed-in region shows the structural orientations of sutures, epidermis cells and hard phase. The zoomed in area can be used to model the behavior of the seed coat using constitutive equations. Reproduced with permission from (Hasseldine et al., 2017; Yang et al., 2015). 2. The digital model of two different types of turtle shell (domed vs. flat shell) were subjected to finite element analysis with appropriate material properties and loading regime. The stress contours of the flat shell show it experiences more stress when compared to the domed shell. Reproduced with permission from (Rivera and Stayton, 2011).

2.4.2 Finite Element Analysis

Finite element analysis (FEA) is used extensively to mathematically model and numerically solve structural problems involving intricate and complex geometrical structures, to validate mechanical experiments and/or to test structures which otherwise cannot be tested using mechanical experiments. To model a biological object (e.g., a piece of the skeleton), the geometry is imported into FEA software (e.g., from CT

scan data), assigned appropriate material properties and loading conditions (e.g., tension, compression), and then divided into smaller parts called finite elements in a process called meshing. The mesh contains all the material and structural information about the model. By dividing a complex problem into simpler parts, meshing enables simulation of a composite structure's reactions to forces, and visualization of parameters like stress and strain at very specific regions of interest. This enables one to simulate the behavior of complex biological geometries and test the effects of alternative morphologies. Additionally, the data from FEA can also provide visual estimates of stress distributions within a biological system (e.g. Fig. 5, turtle shell images).

Because of these advantages, FEA has been used considerably to investigate the mechanical performance of biological systems and validate experimental data. In tiled biological systems, for example, FEA and mechanical testing of various turtle species' shells were compared to understand mechanical properties and the role shell shape plays in overall mechanics (Chen et al., 2015a; Damiens et al., 2012; Rivera and Stayton, 2011) (Fig. 5). The turtle shells are multiphase composites arranged in a multiscale hierarchy (Rhee et al., 2009) making them interesting model systems for mechanical testing to understand their structural mechanics. The data obtained from mechanical tests estimated the strength and elastic modulus of various regions of the carapace (Achrai and Wagner, 2013a; Rhee et al., 2009; Rivera and Stayton, 2011) and were validated by comparing with results from finite element models (Damiens et al., 2012). FE models also provided insight into the regions of failure within the shell, which can be observed from the stress distribution contours provided by FE data (Damiens et al., 2012; Rivera and Stayton, 2011). Finite element analysis was also useful in analyzing the hydrodynamic behavior of the turtle shell. Stress contours obtained from FE analysis showed that the morphological features of the turtle's shell have a direct implication on the hydrodynamics of the animal. From the FE data, it was observed that shells having a flattened surface have higher hydrodynamic efficiency by reducing the drag forces (the force that resists forward movement of the animal when they swim) when compared to domed shell species (Rivera and Stayton, 2011). However, from the FE data, it was observed that the shell strength of the flattened shell is lower when compared to domed shell morphology (Rivera and Stayton, 2011), illustrating a trade-off between hydrodynamics and strength in the performance of different shell shapes.

A similar simulation approach was used to investigate the carapace of boxfish, where the role of carapace shape was analyzed using computational fluid dynamics (CFD), a similar technique to FEA, which is used to compute problems involving fluid flow and hydrodynamics. It was found that the boxy shape of the carapace generates destabilizing forces, which overall increase the drag experienced by the fish (Van Wassenbergh et al., 2015). However, these destabilizing forces allow the fish to maneuver easily, where they can make a complete rotation of their body at an angle of 180° in a short area span. This allows the boxfish to navigate through coral reefs, which are often obstacle-rich (Porter et al., 2017; Van Wassenbergh et al., 2015), again illustrating a performance trade-off, in this case between maneuverability and hydrodynamics.

Computational tools like FEA and CFD play an essential role in determining, understanding and validating the mechanical behavior of biological systems. As most biological systems are intricate, they cannot be validated using physical experiments. For instance, the development of cracks within a structure often cannot be visualized in real-time, due to the small scale of cracks and the rapid speed of their evolution. However, with FEA it is possible to build hypothesis regarding their failure and also predict the propagation of cracks within the structure. Similarly, hypotheses can be derived concerning the mechanobiology of an animal during growth, by analyzing and comparing natural changes in structural morphologies across age. Thus computational simulations are not only useful in testing these systems but also to develop hypotheses regarding biologically relevant factors (e.g. the growth, development, and failure of tissues).

2.5 Shark and Ray Tessellated Cartilage

This section (2.5) “Shark and Ray Tessellated Cartilage” is modified from the chapter ***“The Multiscale Architectures of Fish Bone and Tessellated Cartilage and Their Relation to Function”*** where I am an author, published in the book “***Architectured Materials in Nature and Engineering” (Seidel et al., 2019a)***. I contributed in writing the **Mechanics section** and proof reading the structure. The text and the figures are used with permission from the publishing company.

This section explores the state of knowledge of the structure and mechanics of tessellated shark and stingray cartilage before the work of my thesis. The following sections lay fundamental groundwork and identify unanswered questions with respect to shark and stingray cartilage structure-function and why they are important.

2.5.1 Structure

Sharks and rays are often referred to as the 'cartilaginous fishes' , indicating what sets the skeletons of these fishes apart from the bony skeletons of the vast majority of other vertebrates. Like most vertebrates, sharks and rays develop an embryonic unmineralized cartilage skeleton; however, this is never replaced by bone during ontogeny, and instead remains mostly cartilaginous throughout their lifetime (Fig. 6a–c). Bone and unmineralized cartilage are clearly quite different materials for building skeletons, exhibiting major differences in in: (1) tissue organization (bone and cartilage are patterned on type- I and type-2 collagen, respectively), collagen, respectively); (2) material properties (bone is about 10,000 times stiffer than cartilage in most physiological loading regimes); and (3) response to tissue damage (unlike bone, cartilage has a limited vascular and neural supply and can't heal) (Currey, 1999; Ashhurst, 2004; Hall, 2014).

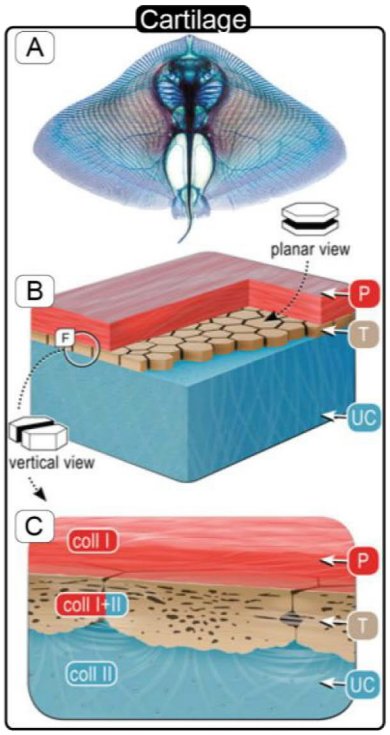

Figure 6: General organization of mineralized skeletal tissues in shark and ray tessellated cartilage.

A. Cleared and stained butterfly ray skeleton (Gymnura sp.). Specimen is young and not yet fully mineralized: blue color shows the cartilage of the skeleton, which will form a mineralized layer later in life. B, C. Structure of tessellated cartilage of sharks and rays, comprising mineralized tiles (tesserae) covering the skeletal cartilage. Abbr.: DL = disordered layer; coll = collagen; LB = layered bone; P = Perichondrium; T = Tesserae; TU = Tubules; UC = uncalcified cartilage.

We believe the distinct structural patterning of shark and ray skeletons allows the cartilage to perform many of the same mechanical roles that bone performs in the other 98% of vertebrates: each piece of the cartilaginous endoskeleton is covered in a thin layer of thousands of mineralized, polygonal tiles called tesserae, typically hundreds of microns wide and deep (Kemp & Westin, 1979; Dean et al., 2009; Seidel et al., 2016) (Fig. 7). This tessellated crust of mineralized tissue is sandwiched between the unmineralized cartilage core of the skeleton and an outer fibrous perichondrium wrapping each skeletal element, resulting in a layered fibro-mineral composite. This unique endoskeletal tiling typically occupies only 30% or less of each skeletal element by volume (Seidel et al., 2017b), yet appears to be an important evolutionary innovation of elasmobranch fishes. Tesserae have characterized elasmobranch skeletons for more than 400 million years (Maisey, 2013) and are vital to shark and ray skeletal biology. Tesserae not only permit interstitial growth of the mineralized layer— via deposition of new mineral at the margins of tesserae (Dean et al., 2009; Macesic & Summers, 2012; Seidel et al., 2016), a growth mechanism impossible with a continuously mineralized crust that cannot remodel—but also afford stiffness to skeletal elements. The dogfish *Scyliorhynus canicula* and round stingray *Urobatis halleri* are the best-studied elasmobranch species as far as the general development and ultrastructure of the tessellated endoskeleton are concerned (e.g. Clement, 1992; Dean et al., 2009; Enault et al., 2015; Seidel et al., 2016; 2017b; 2017a). During development, tesserae first appear in the embryonic skeleton as isolated platelets of cartilage calcification, embedded in and separated by unmineralized cartilage. The individual tiles grow by mineral accretion on their existing surfaces, a process reflected in periodic, concentric layers of varying mineral density (Liesegang lines) in the mineralized tissue (Kemp & Westin, 1979; Seidel et al., 2016; 2017b) (Fig. 7d–g). This accretionary growth eventually brings young tesserae into contact with one another at their lateral edges. Once this occurs, pronounced high mineral density features, known as ‘spokes’, develop at the regions of

direct contact of two adjacent tesserae (Fig. 7d, h, i). Spokes are laminated structures, comprised of densely packed layers of oscillating mineral density, stacked parallel to intertesseral contact surfaces. As the animal and its skeleton grows, tesserae continue to enlarge by accretion, spokes lengthen, radiating outward from tesseral centers like spokes on a wheel (Fig. 7c). The growth mechanisms behind the striking repeated structural pattern in spokes are unknown, but the association of spokes with zones of intertesseral contact argues that the mechanical interaction of tesserae may be a guiding factor.

Both Liesegang lines and spokes illustrate that tesserae are more than simply homogeneous mineralized blocks, instead having local mineral density variation as heterogeneous as that seen in bone (Seidel et al., 2016; Currey et al., 2017). Unlike mammalian bone, however, there is no evidence of remodeling or repair in tesserae (Ashhurst, 2004; Seidel et al., 2016; 2017b). If tessellated cartilage —which apparently performs many of the same functional roles as bone—truly is a deposition-only tissue with no healing capacity, it may also possess in-built strategies for avoiding catastrophic damage, similar to the neoteleost bone described in the previous section. This is an enticing suggestion of the potential for tessellated cartilage as an inspiration for manmade design, since the mechanical performance of the tissue might be reproducible by mimicking structural and material properties, rather than biological action (e.g. cellular involvement, tissue remodeling).

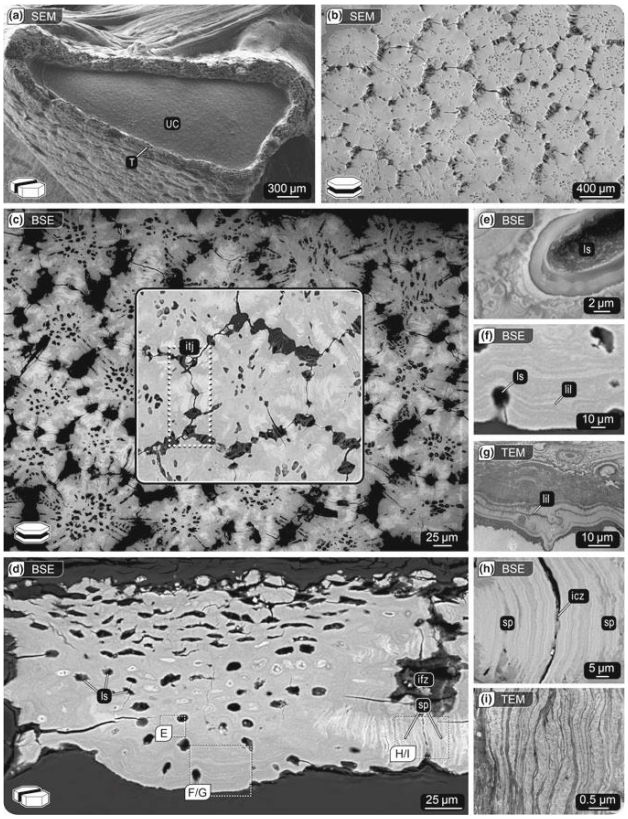

Figure 7: Tessellated cartilage of elasmobranch fish (sharks and rays).

Note icons showing section orientation, introduced in Fig. 6. a Cryo-electron microscopy image of an elasmobranch skeletal piece in cross-section showing the unmineralized cartilage core (UC) sheathed in a thin of mineralized tiles, called tesserae (T). b, c Planar and d vertical views of the tesseral layer, showing abutting tesserae from an adult specimen (b SEM; c, d backscatter SEM imaging, showing only mineralized tissue), revealing the variation in the shapes of tesserae and their intertesseral joints (comprised of regions of direct contact and gaps of fibrous connection between tesserae; see Fig. 8). Note the regional variation in cell lacunae shape and in gray value within tesserae in b, reflecting local differences in mineral density and showing regions of high mineralization associated with zones of intertesseral contact. The most prominent, diagnostic features of tesserae are magnified in e–i using backscatter and transmission electron microscopy, showing e filigree mineralization pattern surrounding a lacuna, f, g Liesegang lines of accretive growth and h, i the laminated, hypermineralized 'spokes' reinforcing intertesseral contact zones. All samples from the round stingray, *Urobatis halleri*.Abbr.: ICZ = intertesseral contact zone; IFZ = intertesseral fibrous zones; ITJ = intertesseral joint; LIL = Liesegang lines; LS = lacunar space; SP = spokes

Our understanding of the features driving tessellated cartilage mechanical properties are in their infancy, but the tissue's performance appears to hinge to a large degree on the interactions and spatial arrangements of softer and harder materials (Fig. 8). There is some evidence, for example, that the serial laminae in spokes, by possessing differing mineral densities, introduce interfaces to redirect cracks and dissipate their energy

(Seidel et al., 2016). At a larger scale, the interactions between tesserae are also characterized by material heterogeneities: the sides of tesserae exhibit smooth patches where they come in direct contact with their neighbors, but these are surrounded by regions of densely aligned collagenous fibers, tethering the tesserae together (Seidel et al., 2016; 2017b) (Fig. 8a–d). The bipartite nature of intertesseral joints is thought to impart an interesting mechanical anisotropy to the skeleton as a whole, providing stiffness or flexibility to the tessellated composite layer, depending on the loading conditions. However, these interactions have never been expressly visualized, largely due to technical constraints challenges of visualizing movements of small features in 3D, at adequate resolution and in hydrated conditions—issues that have been addressed with conditions. Recent high-resolution synchrotron micro-CT (Fig. 8e–g), e–g) and circumvented to some degree in modeling studies of tessellated cartilage (see below) are making headway overcoming these difficulties.

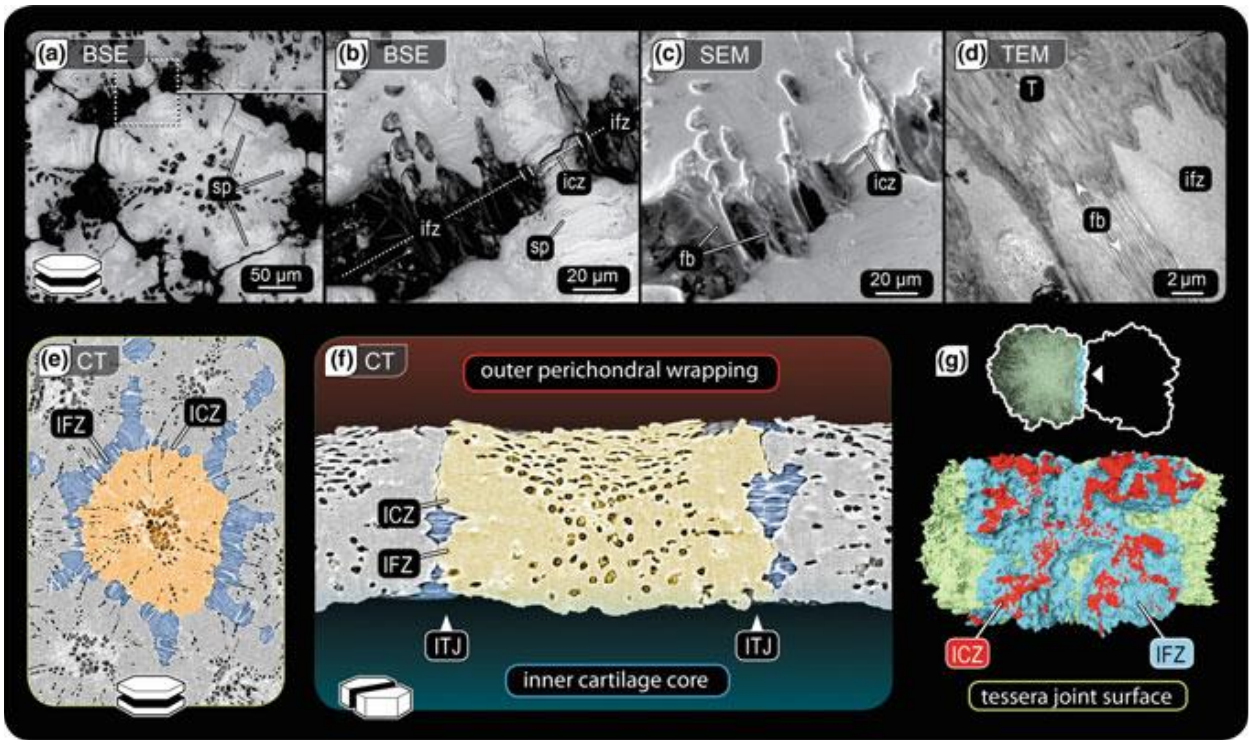

Figure 8: Flexible linkage of tesserae—collagen fibers at the intertesseral joints.

a–d Backscatter SEM, environmental SEM and TEM images showing the structural complexity of a joint of two abutting tesserae in planar section: a, b joints are comprised of regions where tesserae are in direct contact (ICZ) and gaps (IFZ) filled with cells and densely aligned fiber bundles (fb) linking adjacent tesserae. e–g High-resolution synchrotron µCT scans show no macroscopic tesseral overlapping or interdigitation, but fibrous and contact zones interact in complex ways as illustrated in g viewed from the perspective of the neighboring tessera. See abbreviations in the previous Figure.

The general structural features and tissue arrangements of tessellated cartilage described above appear to be largely universal for sharks and rays (Seidel et al., 2016). Our high-resolution electron microscopy and synchrotron tomography data, however, indicate that the shape and structure of tesserae can vary, both within individuals (e.g., between different regions of the skeleton) and among species, in ways that further suggest that the interactions between tesserae are functionally important. For example, the tesserae of different shark and ray species have been shown to vary enormously in size (~100–500 µm (from <100 µm to nearly 1 mm in width and thickness) and shape, ranging from disc-like plates to cuboid blocks (Maisey, 2013; Seidel et al., 2016). The shapes of tesserae also appear to vary according to their location on a skeletal element (e.g. depending on the skeleton's local surface curvature; Dean et al., 2016; Seidel et al., 2016) and according to the skeletal element they cover (e.g. consistently cuboid in the rostral cartilages of some sharks and specific regions of the jaws of some rays; (Maisey, 2013;) (Fig. 9a). These observations are strongly suggestive of a form-function relationship between the shape of tesserae, their joints and the effective mechanical behavior of the tesseral mat and whole skeletal elements, but these, links are only beginning to be established.

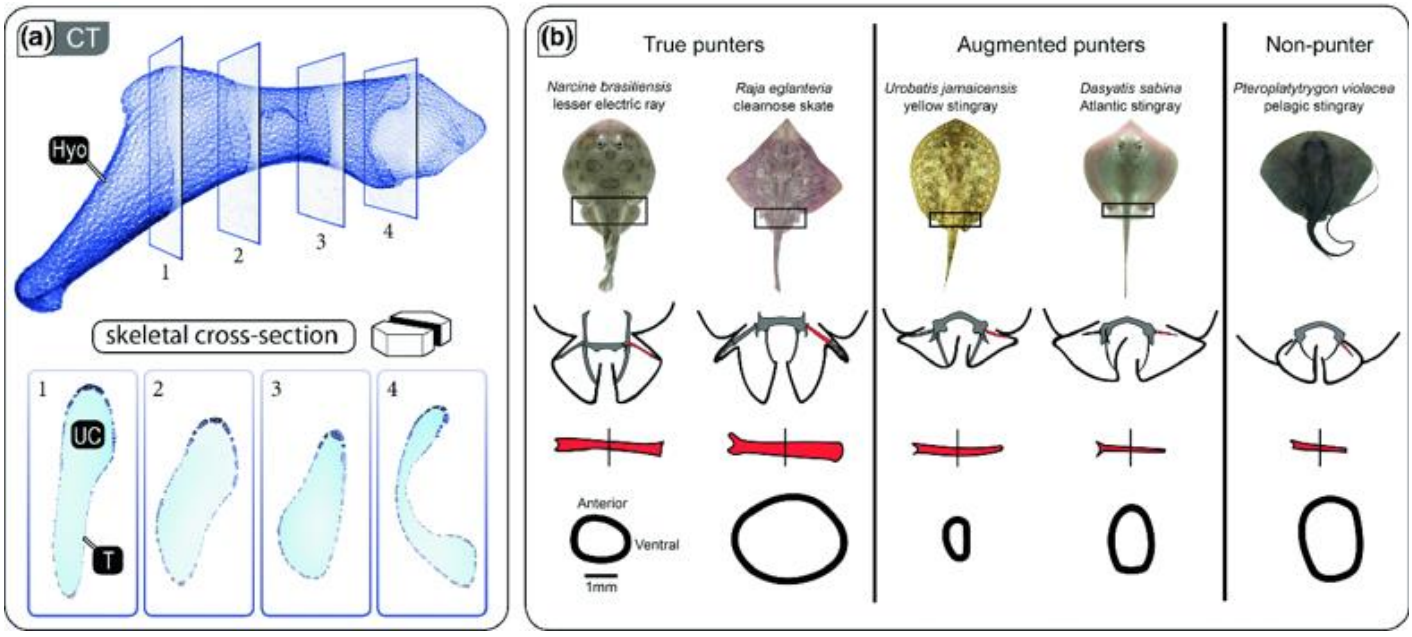

Figure 9: Local variation in tesserae form and suggested relationship to function.

a. Microcomputed tomography of a stingray hyomandibula (Hyo; skeletal piece connecting the jaws with the skull), virtually sectioned in 4 different anatomical positions, showing thicker tesserae (T) in convex

regions. Abbr: UC = unmineralized cartilage. b Cross-sections of pelvic propterygia (skeletal piece supporting the pelvic fins) from different species, showing cross-sectional shape variation according to the species' reliance on 'punting' behavior (use of pelvic fins to move along the sea floor).

2.5.2 Mechanics

In general, the study of tessellated cartilage mechanics lags far behind the study of skeletal anatomy and tesseral ultrastructure. However, the results of several works, taken together, begin to paint a picture of how the structural and mechanical properties of elasmobranch cartilage interrelate and how tesserae play an important role in tailoring skeletal properties to specific ecological roles and high load-bearing activities.

An understanding of the global mechanical properties of tessellated cartilage—a composite with relatively discrete material phases—demands characterization of the properties of the primary tissue constituents: uncalcified cartilage, unmineralized joint fibers and mineralized tissue. Capturing in vivo properties, however, is complicated by the fine scale 3D structural arrangements of tessellated cartilage and the need for testing conditions that mimic physiological conditions (e.g. hydration and load rates). Available evidence indicates that elasmobranch uncalcified cartilage has a proteoglycan and collagen content similar to mammalian hyaline cartilage and suggests that it can be at least as stiff, if not several orders of magnitude stiffer for similar loading rates (mammalian: 0.45–19 MPa vs. elasmobranch: 2-775 MPa - Ferrara et al., 2011; Porter et al., 2013; Liu et al., 2014). These properties depend apparently on the species and the skeletal element tested; more rigorous studies are required to understand the relationships between mechanical properties and composition, loading rate and phylogeny.

Whereas covering a cartilage-like gel with a hard, continuous shell is expected to increase the stiffness but decrease the flexibility of a composite, there is some indication—from tessellated cartilage , but also fabricated arrays (e.g. Martini, Balit, & Barthelat, 2017)—that a tessellated shell with interacting tiles and soft joints can be a 'best of both worlds' configuration, maximizing desirable properties of both tissue phases. (Fahle and Thomason, 2008) showed that compared with embryonic (non-tessellated) small-spotted catsharks (*S. canicula*), adult individuals have jaw cartilage that has a higher ability to damp mechanical energy, but it is also stiffer. A large portion

of the stiffness is surely due to the tessellated layer in adult animals (Egerbacher et al., 2006; Dean et al., 2009; Enault et al., 2015; Seidel et al., 2016). From the biological perspective, this change in properties permits adults to consume harder prey than newborns (Fahle & Thomason, 2008), but is also particularly intriguing for engineering considerations since stiffness and damping are typically negatively correlated in manmade materials. The arrangement of the tessellated layer relative to the direction of loading plays a considerable role in elasmobranch skeletal tissue mechanics. Tessellated cartilage cubes from blue sharks (*Prionace glauca*) loaded normal to the tesseral mat (in stress relaxation experiments) behaved similarly to non-tessellated cubes, being ~45 times softer than tessellated cubes with the load applied in-plane with the tesseral mat (Liu et al., 2014) (Fig. 10). These results are supported by indentation experiments performed on hydrated jaw samples from two large sharks (*Carcharodon carcharias, Carcharias leucas*) (Ferrara et al., 2013). Nanoindentation experiments typically involve pushing a very small, hard tip (e.g. with a tip radius of hundreds of nanometers) into a material to examine hardness and elastic modulus at very small scales. However, as the indenter used by Ferrara et al. was very large (100 µm) and approached the dimensions of some tesserae (Applegate, 1967; Dean et al., 2009; Seidel et al., 2016), we believe their data are more representative of the properties of the composite material (e.g. tesserae and their surrounding soft tissues), in that they report values considerably softer than either the tesserae themselves (Wroe et al., 2008; Liu et al., 2014) or whole skeletal elements of the cartilage (Macesic & Summers, 2012). Deeper investigation into the relationship between local properties and emergent skeletal properties is required to untangle the contradictions in available data.

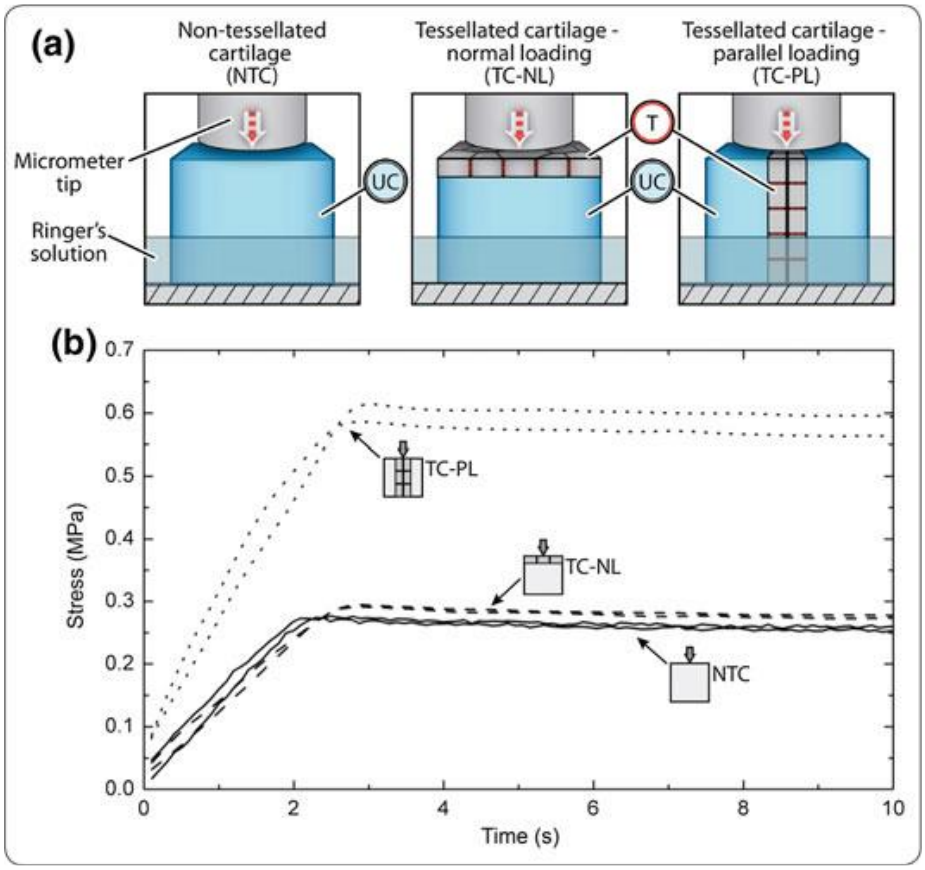

Figure 10: Contribution of the tesseral layer and its orientation to mechanical properties.
Stress relaxation behavior of blue shark (*Prionace glauca*) cartilage was tested with tesserae (T) under normal (TC-NL) and parallel (TC-PL), or without tesserae (NTC). Stress relaxation behavior of nontessellated cartilage (NTC) and tessellated cartilage under normal loading (TC-NL) were similar, but the behavior of tessellated cartilage samples under parallel loading (TC-PL) was far stiffer, indicating that the performance of tessellated cartilage is strongly dependent on the orientation of loads relative to the tesseral layer.

Variations around the generalized tessellated cartilage anatomy described above, when interpreted in the context of animal ecology, also provide perspectives on in vivo skeletal performance, as well as the functional limits of the tissues. For example, in addition to the outer tessellated layer, the jaws of many batoid fishes (rays and relatives) contain hollow tessellated struts (trabeculae) , typically hundreds of microns in diameter, spanning the uncalcified cartilage-filled lumen of the jaws (Summers, 2000; Summers & Ketcham, 2004; Dean & Summers, 2006) (Fig. 11). These appear to be arranged along lines of principal loading, often in narrow regions of the jaws or jaw joints (Dean, pers. obs.), and are therefore structurally and functionally convergent with the trabecular bone found in tetrapods. The importance of trabeculae to the reinforcement of tessellated cartilage is underlined by the high density of trabeculae in

the jaws of species that experience high skeletal loads during feeding, such as the lesser electric ray which uses explosive jaw protrusion to retrieve buried prey (Dean & Summers, 2006) or myliobatid stingrays which employ high bite forces to crush hard shelled mollusks (Summers, 2000; Summers & Ketcham, 2004; Kolmann:2015, see also Fig. 1 in Seidel et al., 2017b).

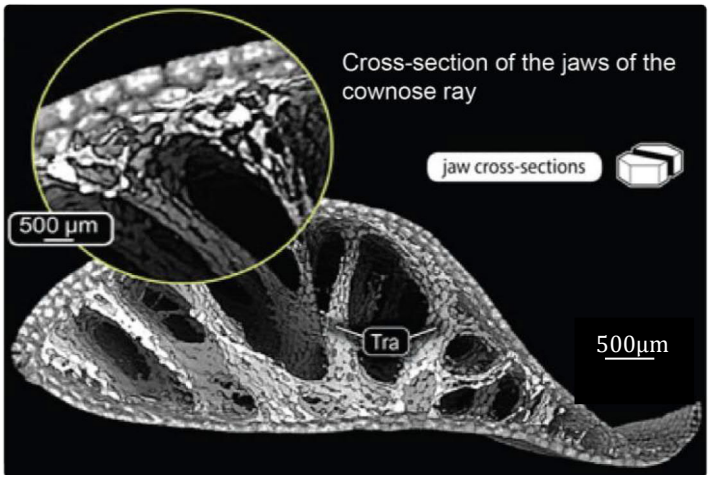

Figure 11: Methods of reinforcement of tessellated cartilage.

Cross-section of a microCT of the jaws of the cownose ray (*Rhinoptera bonasus*), a hard prey specialist, showing mineralized trabeculae (struts) running through the jaw, reinforcing the primary biting direction. Alternatively, tessellated cartilage can be reinforced by multiple tesseral layers, as in the outer layers of the cownose ray jaw. Abbr: Tra = Trabeculae;

Additional mechanisms described for reinforcing tessellated cartilage against bending involve either thickening of the skeleton's hard, outer cortex (i.e. the tesseral layer) or modifications to the cross-sectional shape of skeletal elements. In the former, the tesseral layer is often locally thickened (e.g. the tesserae in skeletal cross-sections in Fig. 2 of (Seidel et al., 2016) vary up to 4× in thickness), particularly in regions in line with principal loading or in areas of high curvature (Dean, Huber, & Nance, 2006; Balaban, Summers, & Wilga, 2014; Dean et al., 2016; Dean et al, in press; Wilga et al., 2016; Seidel et al., 2016). The cortex can also be thickened via introduction of additional tesseral layers, particularly in the jaws of large carnivorous sharks (Dingerkus & Seret, 1991), the "saws" of sawfish (Summers, 2000; Seidel *et al.*, 2017b), or the jaws of species with diets containing large proportions of hard shelled prey (Summers & Ketcham, 2004; Seidel et al., 2017b; Dean et al, in press). Up to 10 supernumerary tesseral layers have been recorded in the jaws of some extant species (Dean et al, in

press). High flexural stiffness in whole skeletal elements appears to result from either high mineral content (a proxy for the proportion of tesserae in an element or crosssection), skeletal cross-sectional shapes with high second moment of area or combinations of the two (Macesic & Summers, 2012; Balaban et al., 2014; Wilga et al., 2016; Huang et al., 2017). Skeletal element flexural stiffness has also been shown to be correlated with differences in ecology—for example, supporting specific locomotion (Macesic & Summers, 2012; Huang et al., 2017) or feeding modes (Balaban et al., 2014)—but mineral content and cross-sectional shape/size do not always vary predictably (e.g. animals with large skeletal cross-sections can have either very high or very low mineral content Macesic & Summers, 2012; Balaban et al., 2014; Wilga et al., 2016). This indicates that tessellated cartilage has evolved to be 'modular', where functionally and ecologically relevant skeletal mechanical properties can be achieved through a variety of structural mechanisms (e.g. cortical thickening, increased second moment of area, introduction of trabeculae), rather than compositional alterations to the apatite mineral in the tessellated layer (e.g. the introduction of heavier elements as can occur in invertebrate tissues Degtyar et al., 2014).

The mechanical influence of the tessellation itself—the tiling of the cortex and the varying patterns formed by tesserae —has yet to be investigated in situ, likely due to the experimental difficulties posed by the size of tesserae and their complex tissue connections. Several studies, however, have incorporated existing materials and/or structural data from the biological tissue in computational simulations and mathematical models of tessellated cartilage, helping to shape informed and testable hypotheses relating to tissue growth and mechanics. Empirical models of tessellated cartilage cross sections, for example, based on biological material and ultrastructural data, suggest that the tessellation plays a role in controlling the stress distribution within the skeletal tissue during bending (Liu et al., 2010; Fratzl et al., 2016). This is a function of the narrow joints between tesserae, the structure of which is hypothesized to result in strikingly different properties in tension than compression (Fig. 12). In a hypothetical laminated tessellated cartilage beam—a monolithic core of unmineralized cartilage sandwiched between two thin tessellated layers—subjected to bending, the tesserae on the side of the beam loaded in tension should pull apart from one another, whereas tesserae on the compressive side of the beam should readily collide. Such a

compression-tension asymmetry would impart a constrained flexibility in tessellated cartilage that could also play a role in the tissue's ability to resist damage. In general, the combination of a stiff outer cortex and a soft inner core will tend to ensure that higher stresses are concentrated more safely in the stiffer cortical/mineralized tissue rather than the softer core/unmineralized tissue (Liu et al., 2010; Ferrara et al., 2011; Fratzl et al., 2016). This is true, even if the cortex is continuous rather than tessellated, as was simulated in Finite Element models of the jaws of two large shark species subjected to biologically-relevant bite forces (Ferrara *et al.*, 2011).

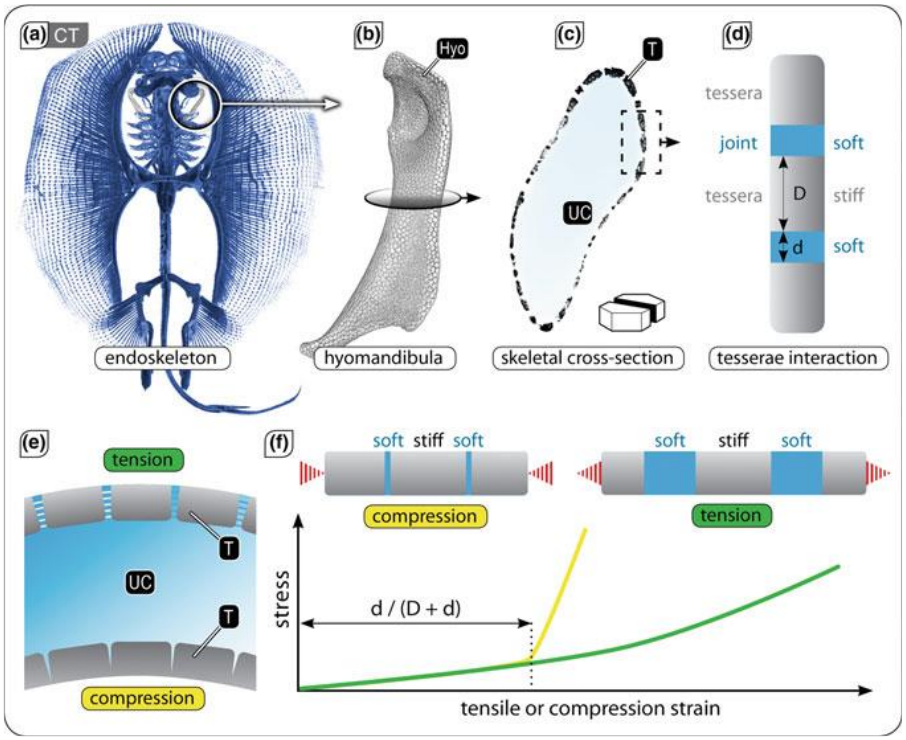

Figure 12: Proposed compression-tension asymmetry in tessellated cartilage.

a–c Micro-CT scan of the skeleton and hyomandibula (Hyo) of a stingray (*Urobatis halleri*) illustrating the composite nature of tessellated cartilage, formed by stiff mineralized tiles (T) separated by softer unmineralized joints. Abbr: UC: unmineralized cartilage. d Schematic of alternating soft and hard constituents in a tessellated system. e Schematic section of tessellated skeletal element in bending, with the top and bottom tessellated layers experiencing tension and compression, respectively. f Hypothetical stress-strain curves illustrating the proposed tension-compression asymmetry of a tessellation. In tension, the deformation will be dominated by the stretching of the soft joint interlayer (yellow line), whereas in compression, the behavior is stiffer (green line), dominated by the stiff tiles colliding once the thickness of the soft interlayer is exhausted [at a compressive strain of approximately d/(D + d)].

Tessellating the cortex, however, serves additional functions, such as protecting the mineralized tissue from fracture on the tension side of the skeleton by localizing tensile

stresses in the intertesseral joint fibers rather than in tesserae. At the same time, the compressive stiffness of tesserae should shift the skeleton's neutral axis of bending closer to the compressive side of the skeleton, concentrating potentially damaging compressive stresses in the tessellated layer rather than the unmineralized cartilage (Liu et al., 2010; Fratzl et al., 2016). In this way, the tessellation can manage bending loads and increase resistance to damage by distributing the highest stresses to the tissues and loading regimes best able to bear them. Stresses may also be mitigated by the properties of the unmineralized cartilage itself, which Wroe et al. [49] showed would tend to result in considerably lower stresses and higher strains than simulated shark jaws made of bone and subjected to the same bite forces (Fig. 13). The hypothesized stress-management behavior of tessellated cartilage may therefore serve a protective function, in a skeletal tissue that apparently cannot heal (Ashhurst, 2004; Dean et al, in press ; Seidel et al., 2016; Seidel et al., 2017c), although it is surely cyclically loaded a massive number of times over an animal's lifetime during swimming and feeding behaviors.

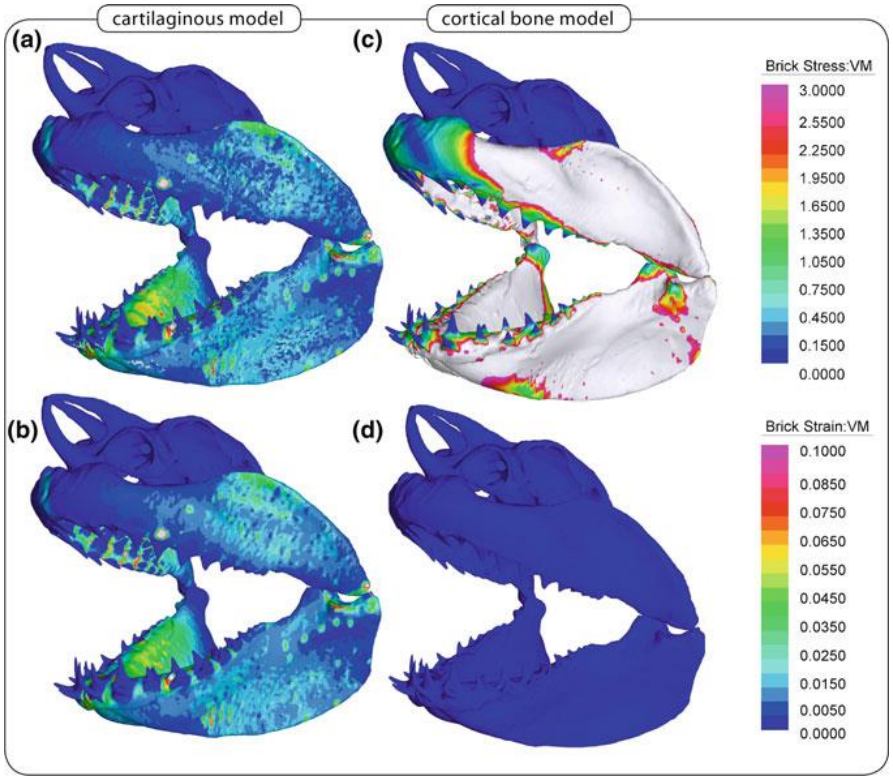

Figure 13: Simulation of feeding mechanics in white shark jaws with varying material properties.
a, c VonMises stress and b, d strain distributions for maximal bilateral bites in Finite Element simulations of jaws with tessellated cartilage properties (a, b) and cortical bone properties (c, d). Note that stress is much lower, but strain is much higher in the cartilaginous model.

Most models of tessellated cartilage have focused largely on the mechanical result of combining soft and hard tissues; the geometry of the tessellation —the distribution of shapes and sizes of tesserae —surely also plays an important role in the mechanics of the skeleton, yet this has hardly been investigated. Tesserae are typically polygonal in shape and apparently predominantly hexagonal, but have been observed to vary in the regularity of their form and range from squares to twelve sided polygons (Dean & Schaefer, 2005; Dean et al., 2016; Seidel et al., 2016; Dean, pers. obs.). But the effect of shape and the ultrastructure on tesserae mechanics were not studied before.

In this dissertation, two project phases were developed. The first project phase analyses the effect of tiling shape, structure and material properties on the mechanical behavior (specifically, the effective stiffness) of the composite material. In the second project phase, the parametric CAD models of tesserae are developed with ultrastructural features incorporated in them. The ultrastructural features are parametrically varied in the CAD models and then subjected to finite element analysis. The results obtained from finite element analysis help in determining the effect of ultrastructural features on tesseral mechanics and their contribution to biological functions related to growth and load management within the tesserae, and both the project phases are discussed in the following sections.

3. Phase 1

The phase 1 project has been published as a paper titled "***Mechanical behavior of idealized, stingray-skeleton-inspired tiled composites as a function of geometry and material properties" (Jayasankar et al., 2017a)*** where I am the first author. The text and the figures are used with permission from the journal.

3.1 Introduction to phase 1

The tiling of surfaces with repeated geometric elements is a common structural motif in biological tissues and one that transcends phylogeny. Structural tilings have evolved independently in multiple systems and at a variety of size scales: from the micron-scale plates in the layers of nacre in mollusc shells (Barthelat and Zhu, 2011), to the sub-millimeter mineralized tiles (tesserae) sheathing the cartilages of sharks and rays (Seidel et al., 2016a), to the macroscopic plates in the body armors of boxfish (Chen et al., 2015a; Yang et al., 2015) and turtle shells (Chen et al., 2015a; Krauss et al., 2009b) as shown in Fig. 14a. The mechanical characteristics of tiled natural composites are typically impressive amalgamations of those of their mineralized and organic component parts, resulting in natural armors that can be both lightweight and puncture resistant, but also flexible and tough (Chen et al., 2013; Chen et al., 2014; Chen et al., 2015a; Krauss et al., 2009b; Liu et al., 2010a; Liu et al., 2014a; Martini and Barthelat, 2016; Rudykh et al., 2015; Yang et al., 2013a; Yang et al., 2013b; Yang et al., 2012). The shapes and materials of the tiling subunits, their spatial arrangement, and their physical interactions control composite functional properties, guiding deformation and hindering damage propagation (Chen et al., 2015a; Krauss et al., 2009b; Liu et al., 2010a; Vernerey and Barthelat, 2010; Yang et al., 2015). Analytical and experimental models of suture behavior, for instance, show that simple adjustments to the geometry and/or attachment areas of sutural teeth can be used to tune the mechanical properties (e.g. stiffness, strength, toughness), deformation or failure behaviors of a structured composite (Achrai and Wagner, 2013b; Atkins et al., 2014; Balaban et al., 2015; Cadman et al., 2013; Chen et al., 2013; Chen et al., 2014; Ferrara et al., 2013; Krauss et al., 2009b; Lin et al., 2014a; Lin et al., 2014b; Liu et al., 2014a; Seidel et al., 2014; Studart, 2012; Van

Wassenbergh et al., 2015; Yang et al., 2013a; Yang et al., 2013b; Zhang et al., 2013b; Zhang et al., 2014).

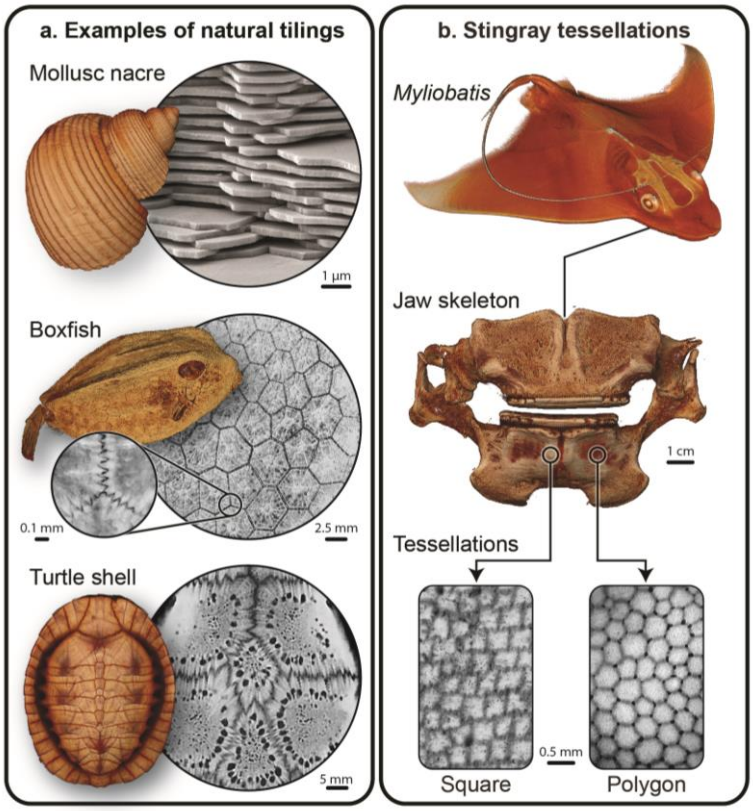

Figure 14: Examples of natural tilings and stingray tessellations.

a. Examples of natural tilings, none of which are true tessellations due to overlapping (mollusc nacre) or interdigitating (turtle shell, boxfish scute) morphologies. b. Polygonal and square tessellations found in stingray cartilage. Organism and tissue images are compiled from a variety of species: a. *Turbo caniculatus* (mollusc shell), *Haliotis rufescens* (nacre*); Phrynops geoffroanus* (turtle shell); *Ostracion rhinorhynchos* (boxfish and scute inset; MCZ4454), *Lactoria cornuta* (interdigitations). b. *Myliobatis freminvillei* (stingray; USNM204770), *Myliobatis californica* (jaws; MCZ886), *Aetobatus narinari* (square tessellation), *Leucoraja erinacea* (polygonal tessellation).

The surface tiling of the skeleton of sharks and rays (elasmobranch fishes) has been recognized for over a century as a diagnostic character of all living members of this group, but the functional significance of this feature remains unclear. The tiled layer of elasmobranch cartilage, like most natural tilings, is comprised of hard inclusions/tiles (tesserae; Fig. 14b) joined by unmineralized collagen fibers (see also Fig. 2c;Seidel et al., 2016a). However, elasmobranch tesserae lack the interdigitations found in many other biological tilings, such as those seen in turtle osteoderms or boxfish scutes (Fig. 14a) (Chen et al., 2015a; Krauss et al., 2009b; Yang et al., 2015). Furthermore, unlike the

dermal scales of fishes, armadillo and some mammals, arrays of tesserae lack appreciable gaps or overlaps, and so can be considered “true tessellations” (Bruet et al., 2008; Chen et al., 2015a; Wang et al., 2016a; Yang et al., 2012). Elasmobranch tesserae also represent an intermediate size class of biological tiles, being typically hundreds of microns in size, an order of magnitude larger than mollusc nacre platelets and at least an order of magnitude smaller than most scales and osteoderms (Chen et al., 2015a; Olson et al., 2012). The tessellation of the elasmobranch skeleton is believed to manage stress distribution in a way that can minimize damage to the cartilage and also provide both flexibility and stiffness (Fratzl et al., 2016a; Liu et al., 2010a; Liu et al., 2014a), the latter being somewhat counterintuitive considering the lack of obvious interlocking features between tesserae. The correlation between the structural and material aspects of tesserae and the mechanical properties of the skeleton at a larger scale remain undemonstrated. In particular, although elasmobranch tessellation is apparently largely comprised of hexagonal tiles (Dean and Schaefer, 2005; Dean et al., 2005; Fratzl et al., 2016a; Seidel et al., 2016a), other shapes are possible (Fig. 14b); however, the role of tile shape in the mechanics of the tessellated composite (i.e. at the level of the skeletal tissue) has never been investigated.

In the current paper, our objectives are to analytically model biologically-inspired tessellated composites constructed with different tile types (triangle, square and hexagon) to observe the effects of (1) tile shape, (2) joint/tile size and (3) joint/tile material properties on the mechanical behavior (specifically, the effective stiffness) of the composite material (variables shown in Fig. 15c). Our results establish a baseline for future analyses of tessellations with more complicated (e.g. biologically relevant) morphologies (e.g. 3D tessellations) and loading conditions (e.g. bending, shear and multi-axial loading). The results presented in this study improve our understandings of the functional significance of the tesseral morphologies observed in elasmobranch skeletons, while also framing form-function laws for engineered tiled composites.

3.2 Methods: Phase 1

3.2.1 Modified Rule of Mixtures model

To estimate the mechanical characteristics of our tessellated composites, we modify traditional Rule of Mixtures methods, which allow calculation of the contributions of constituent phases to the net stiffness of a composite. These methods permit the modeling of different materials arranged either in parallel (Voigt iso-strain model) or in series (Reuss iso-stress model), taking into account their volume fractions (VF) and stiffnesses (E1 and E2) (Bayuk et al., 2008). Geometrical interpretations of the Voigt and Reuss models are shown in Fig. 15a.

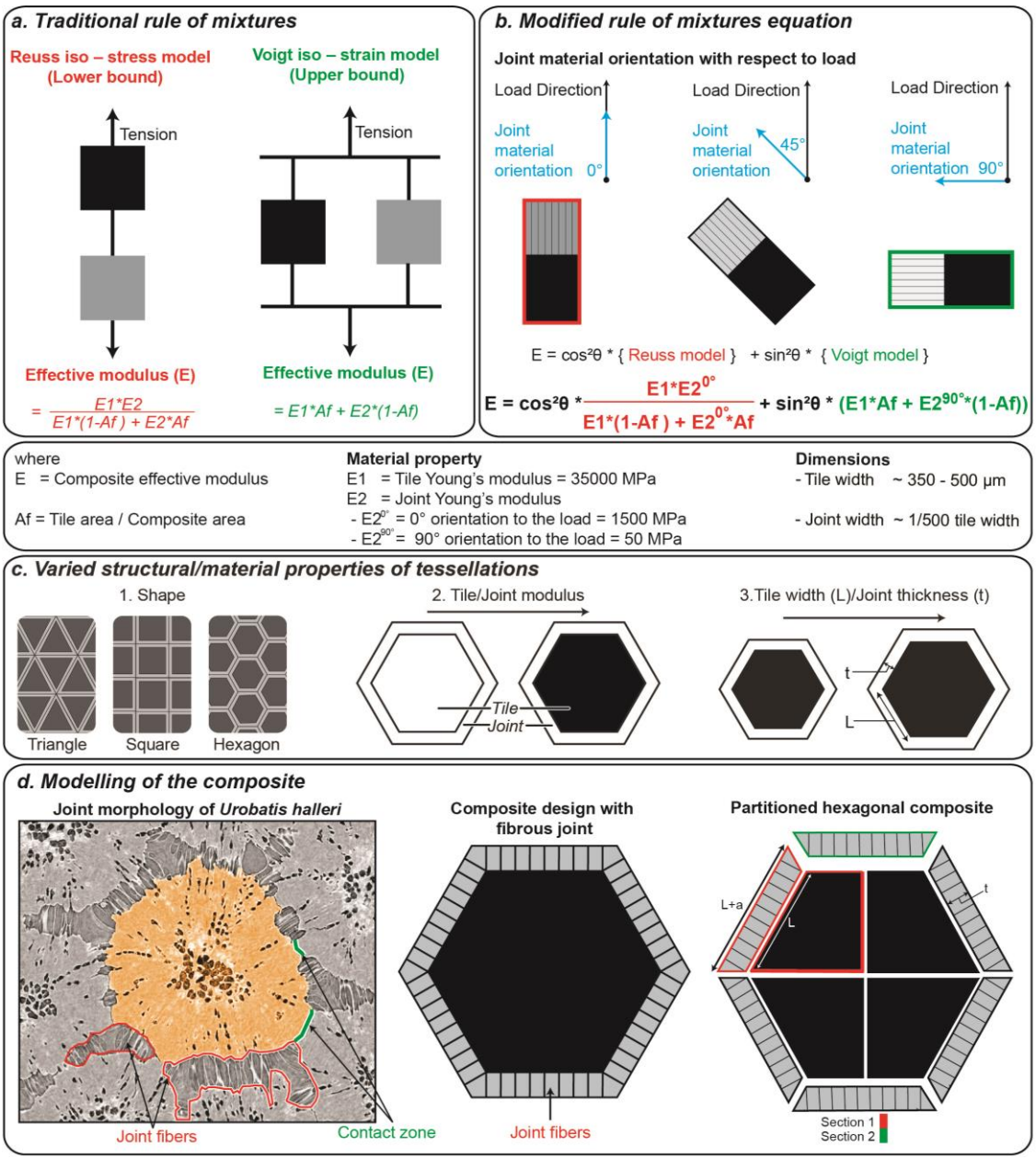

Figure 15: Rule of mixtures and modified rule of mixtures.

a. Rule of Mixtures: Reuss and Voigt models. b. Orientation of model with respect to direction of load and the effect on joint material Young's modulus and composite effective modulus (modified Rule of Mixtures). c. Structural and material properties of tessellations varied in this study, including shape, tile/joint material, and tile area/joint width. d. Modelling of the composite with the inspiration derived from *Urobatis halleri* (see text for explanation); the partition of hexagonal tile composite. See the Appendix for full derivations for all three tile shapes.

The classical Rule of Mixtures models assume monolithic constituent materials with no anisotropy of material properties, arranged either in series with or perpendicular to loading orientation. This assumption is reasonable for calculating the effective modulus

of a composite where materials are arranged in simple geometries and where loading orientation plays no role on a constituent material's properties.

The arrangement and morphology of joint material in tessellated cartilage, however, argue for a degree of orientation-dependent behavior. Intertesseral joints are comprised of linearly arrayed collagen fibers, oriented perpendicular to tesseral edges (Seidel et al., 2016a) (Fig. 15d; see discussion of tesseral ultrastructure below), and given also that our investigated tile models possess edges where joint and tile material are neither in perfect series nor parallel arrangements relative to load (e.g. Section 1 in Fig. 15b), we employ the two following modifications to the traditional Rule of Mixtures models.

In the first modification, to approximate the mechanical behavior of the intertesseral joint material of elasmobranch cartilage (for which no experimental data exist; see Section 2.3 below), we assume the material properties of the joint material to resemble those of other vertebrate fibrous materials. We assume the Young's modulus of the joint material perpendicular to the tesseral edge ($E2^{0°}$, in line with the joint fiber directions) to be 1500 MPa (the tensile modulus of tendon; Shadwick, 1990), whereas we assume the modulus orthogonal to the direction of joint fibers ($E2^{90°}$) to be only 50 MPa (the compressive modulus of periodontal ligament; the compressive modulus of periodontal ligament; Rees and Jacobsen, 1997). The assumption of compressive modulus of periodontal ligament is done because the tendon's compressive modulus is not studied as they don't have compressive behavior. This modification is a matter of a simple substitution of $E2^{90°}$ for $E2^{0°}$ where Voigt (in-parallel) models are used in our calculations (Eq.1 below).

In the second modification, we account for situations where the tile and joint interface is oblique to the loading direction (i.e. neither a pure in-series/Reuss nor parallel/Voigt arrangement), such as can be seen in the equations for triangle and hexagon composites in the Appendix. This is accomplished by the following equation, which exploits the Pythagorean trigonometric identity, $\cos^2\theta + \sin^2\theta = 1$, to scale the relative contributions of Voigt and Reuss models according to the angle of rotation (θ) of the composite relative to loading direction:

Equation 1

$$E=\cos^2\theta * [\text{Reuss model}] + \sin^2\theta * [\text{Voigt model}]$$

Equation 2

$$E = \cos^2\theta * \left[\frac{E1 * E2^{0^\circ}}{E1*(1\text{-}AF) + E2^{0^\circ}*(AF)}\right] + \sin^2\theta * [(E1 * AF + E2^{90^\circ} * (1\text{-}AF)]$$

The equation functions as a pure Reuss model with $E2^{0^\circ}$ joint modulus when in series with the load ($\theta = 0^\circ$: $\sin^2 0^\circ=0$, $\cos^2 90^\circ=1$; Fig. 15b, left image) and a Voigt model with joint modulus $E2^{90^\circ}$ when tissues phases are oriented in parallel with the load ($\theta = 90^\circ$: $\sin^2 90^\circ=1$, $\cos^2 90^\circ=0$; Fig. 15b, right image), with intermediate values of θ resulting in values of E that are proportional mixes of the pure models. This equation therefore accounts for the effects of both fiber orientation and oblique joint-tile interfaces (i.e. whole model orientation) relative to axial loads.

Our equation is more suited to our modeling goals than Krenchel's modified Rule of Mixtures model (Aspden, 1988; Krenchel, 1964), which modifies a Voigt model to formulate the effects of the orientation of stiff fibers within a softer matrix on a composite's stiffness:

Equation 3

$$E_{composite} = \cos^4(\theta) * E_{fiber} * AF + E_{matrix} * (1 - AF)$$

The limitation of Krenchel's model is that it assumes only the effect of fiber material orientation with respect to the Voigt model and so for our purposes could only capture the effects of changing joint fiber orientation in an in-parallel loading scenario.

3.2.2 Application to tessellation models

To apply these models to tessellations constructed from arrays of triangular, square and hexagonal tiles, we divide each composite unit cell (the tile and half of its surrounding joint material) into simple geometric shapes containing tile and joint material for which effective modulus can be calculated using Equation 1. The subdivisions of the hexagonal tile are shown as an example in Fig. 15d. Although we focus on only one composite cell in our approach, this provides an estimate of the stiffness of a periodic array of tiles,

similar to what would be generated in a Finite Element (FE) model employing periodic boundary conditions (PBC; see Section 2.5 below).

The effective modulus of each unit cell portion is then calculated using the modified Rule of Mixture equations provided above (Fig. 15b), as a function of tile side length (L), tile modulus (E1), joint thickness (t) and joint modulus (ranging from $E2^{0°}$ to $E2^{90°}$, depending on the orientation to the loading direction). The effective modulus of the entire tile-joint composite (E) is then determined by combining the contributions of each of the unit cell portions, using traditional Voigt/Reuss models, according to their volume fractions relative to the whole and whether the subunits are arranged in parallel or series (e.g. Section 1 and 2 in Fig. 15d are arranged in series). The full calculations and assumptions of these models are provided in the Appendix. Using this approach, the effective modulus of the three tiled composites (comprised of triangle, square and hexagonal tiles) is evaluated. Alternate partitioning of unit cells (i.e. using other lines of division) had little effect on model results and only for the thickest joint morphologies for triangle and hexagon unit cells; this was a function of the different partitioning schemes altering whether the extreme corners of unit cell were assigned as oblique or in-series elements (data and partition schemes are provided in the Appendix).

The basic Voigt and Reuss models are shown in Fig. 15a. When calculated using the same volume fractions of tile and joint materials as those in our composite models, these models act as upper and lower theoretical bounds, respectively, for our data. The mechanical behavior of the Voigt model (upper bound) is dictated by the properties of the stiffer material (tile = E1), given the assumption that the strains are uniform across the composite, due to the two phases of the composite being in parallel. In the Reuss model (lower bound), the properties are dominated by the softer material at 0° orientation to the load (joint = $E2^{0°}$), due to the in-series orientation of the phases, resulting in uniform stresses across the composite.

3.2.3 Model constraints and biological relevance

In terms of inputs for our models, information on the structural and material properties of tessellated cartilage is limited, with the most information available on tesseral ultrastructure. Tesserae in curved regions of shark and ray skeletal elements may have

more block-like, columnar or spherical morphologies (Fratzl et al., 2016a; Fig. 1 in Liu et al., 2014a; Fig. 2 in Seidel et al., 2016a), but as their interactions with neighboring tesserae are more 3-dimensional, we derive the following synthesis of tesseral morphology from flat regions of the skeleton, where tesserae are more plate-like (e.g. e.g. Fratzl et al., 2016a; see Fig. 10 in see Fig. 10 in Seidel et al., 2016a). Evidence from a variety of species indicates that tesserae can range from four- to twelve-sided, but are mostly hexagonal (Dean and Schaefer, 2005; Dean et al., 2005; Fratzl et al., 2016a; Seidel et al., 2016a) and that tesserae in adult animals are typically between ~200-500µm wide (within the plane of the tesseral mat), with little space between them (Clement, 1992a; Dean, 2009; Dean et al., 2017a; Dean et al., 2009b; Kemp and Westrin, 1979b; Seidel et al., 2016a). The intertesseral joint space (the region of interaction between two adjacent tesserae) has a complex morphology, comprised of regions where neighboring tesserae are in direct contact (intertesseral contact zones: ~1-5µm wide; Fig. 15d) and wider gaps filled with linearly arrayed collagen fibers (intertesseral fibrous zones: ~20-30µm wide; Fig. 15d) (Seidel et al., 2016a).

Material property data for tesserae remain scarce and inconsistent. The Young's modulus for intertesseral joint fibers is unexamined, but we will assume it to be similarly anisotropic to other vertebrate fibrous tissues (see Section 2.1 above). The Young's modulus for hydrated shark and ray mineralized tissue, derived from nanoindentation, has been reported to span a massive range from 79 to 4000 MPa (Ferrara et al., 2013; Wroe et al., 2008a). The reason for this measurement variation is unknown, but is likely due largely to methodology (sample preparation, indenter size), and also perhaps interspecies differences in tesseral shape/properties. Recent data have also shown extensive local variation in mineral density within tesserae (Seidel et al., 2016a). Correlated measurements of mineral density from quantitative backscatter electron imaging and material property data from nanoindentation argue that some sub-regions of tesserae may be up to an order of magnitude stiffer than the previously reported maximum (up to ~35GPa; R Seidel, pers. comm.). A tesseral Young's modulus in the higher range of reported values (e.g. > 1 GPa) is further supported by the comparable properties of other mineralized skeletal tissues (e.g. Carter and Hayes, 1977; Currey, 1988), the observations of extremely high mineral densities in tesserae (R. Seidel, pers. comm.; R. Seidel, pers. comm.; Seidel et al., 2016a) and the direct

relationship between mineral density and indentation modulus in calcified cartilage and bone (Gupta et al., 2005).

3.2.4 Visualization and evaluation of data

Our analytical models were evaluated for $E1/E2^{0°}$ from 1.0 (equal tile and joint moduli) to 25.0 (tile modulus 25x that of joint modulus), and for $t/\sqrt{A}$, from 0.0 (no joints) to 0.10 (e.g. 10% of the square's side length). These values cover a biologically-relevant range of tesseral properties, from the softest to stiffest estimates of tesseral and fiber material properties and from the narrowest to widest measurements of intertesseral gaps and tesserae (Fig. 15c). For reference, we indicate with a red dot in Figs 16b and 17 our best approximation of the properties of the tesserae of round stingray (*Urobatis halleri*), as this species is the most studied in terms of ultrastructure and material properties (e.g. e.g. Dean, 2009; e.g. e.g. Dean et al., 2017a; e.g. e.g. Dean et al., 2009b; Fratzl et al., 2016a; Seidel et al., 2016a; Wroe et al., 2008a).

We generated 2D contour plots for each unit cell shape using compound non-dimensional variables that take into account all elements of our effective moduli equations (Fig. 16). In these plots, the x-axis is the ratio of the stiffness of the tile material relative to the joint material ($E1/E2^{0°}$) and the y-axis is the ratio of the thickness of the joint relative to a linear measure of tile size ($t/\sqrt{A}$), with the "topography" (colored contours) of the graph representing the relative effective modulus (REM) of the composite (the stiffness of the composite relative to its joint stiffness, $E/E2^{0°}$). Therefore, moving in the positive x-direction corresponds to increasingly stiffer tiles (or softer joints) and moving in the positive y-direction, a thickening of the joints relative to tile dimensions. These unitless ratios allow comparison of the effects of both material properties (x-axis) and structural/shape parameters (y-axis) on composite mechanical performance (REM).

The first order parameter controlling mechanical properties of a composite is the volume fraction of the components (Hull and Clyne, 1996; Wang et al., 2011), or area fraction (AF) of joint and tile material, in the case of our 2D tilings. As we are interested in the role of shape and size of tiles with respect to a "biologically relevant" joint layer (i.e. one of a particular, measureable thickness) we chose to compare our predictions for

fixed values of t/√A rather than AF. For comparative purposes, however, we include in the Appendix our results (Fig. A.6) plotted with respect to area fraction. As expected the graphs plotted in terms of AF show little variation among the three unit shapes, underlining the lesser effect of unit cell shape compared with that of area fraction.

Our chosen y-axis size metric (t/√A) produced similar results to other descriptors of tile/joint geometry, such as ratios of joint thickness (t) to tile length (L) or perimeter (p) (data not shown). Given our interest in using a y-axis metric that contains a linear measure of joint thickness, we use t/√A because, among possible tile/joint geometry metrics (e.g. t/p, t/L), it is most comparable to the area fraction (an important element of the Voigt/Reuss equations). Also, as effective modulus calculations for the three unit shapes are most similar when tile areas (rather than side lengths or perimeters) are normalized (data not shown), the results reported below according to t/√A represent a more stringent series of comparisons.

3.2.5 Simulation and experimental verification of models

The three unit cell types can be partitioned in several different ways. To test for consistency between methods, we compare the results of two different partitioning schemes (see Appendix).

To verify the efficacy of our analytical models, Finite Element (FE) models representing the three tilings were generated in ABAQUS from models built in Rhino computer-aided-design (CAD) software with the Grasshopper plug-in. A 1% compressive strain and PBCs were applied and the models tested over a range of E1/E2 values for relatively thick joints (t/√A = ~0.07). The resultant stress-strain curves were used to calculate the models' composite stiffness and those compared to the composite effective stiffnesses estimated by our analytical models using the same input parameters. A more detailed description of the methods can be found in the Appendix.

3.3 Results and discussion

FEA and analytical calculations showed general agreement in their estimates of composite model stiffness as a function of E1/E2 and a given t/√A value (Supplemental

Fig. A.10). This supports our conjecture that our analytical models of a single tile and its surrounding joint material can be used to approximate the behavior of a larger tiled array, in a manner similar to FE models employing periodic boundary conditions (see Appendix). Furthermore, our results were largely consistent, regardless of the unit cell partitioning scheme used (see Appendix, Figs A.4, and A.7).

All data calculated from the analytical models fall within the range of values depicted in the lower bound (Reuss) and upper bound (Voigt) contour plots for their unit cell shape; the upper and lower bound contour plots exhibited similar form and magnitude for all unit cell shapes, therefore, we show only those plots for the square unit cell as an example in the first row of Fig. 16. For the lower bound, close to the x-axis, contour lines showed positive slopes that gradually decreased and leveled off to roughly horizontal lines at higher x-axis values. Such regions of more horizontal contour orientation (i.e. at higher x-axis values) indicate a more geometry-sensitive/material-insensitive system, where changes in joint thickness (y-axis) have an effect on REM, but changes in joint/tile material properties (x-axis) have little effect. In contrast, a more vertical arrangement of contours, like those fanning out from the y-axis in the upper bound plot, signify a more geometry-insensitive/material-sensitive system, where material property (x-axis) changes are important, but there is little effect of changes in joint thickness (y-axis) on the REM of the composite.

In general, all models showed an increase of composite Relative Effective Modulus moving clockwise through the contour plot (i.e. towards thinner joints and stiffer tiles), however the relative widths of their contours became more evenly spaced from square to triangle to hexagon. The three unit cell shapes (triangle, square and hexagon) show a continuum in contour plot topography: starting with the square's stacked, asymptoting contours (which resemble those of the lower bound), and moving from triangle to hexagon, contour slopes steepen, resulting in the hexagon's contours being more similar in shape to those of the upper bound graph (Fig. 16A). This argues for the models, from square to triangle to hexagon, behaving increasingly as hybrid iso-stress/iso-strain composites and less as pure iso-stress models. The relative effective modulus for parameters such as joint area, perimeter of the tile are calculated and found that there are similar patterns across shapes. The structural dimensions of the joint morphology

was chosen such that they are reflective of accurate biological system as joint area was not characterized in the biological system.

The variation in shape and spacing of contour lines among the three unit cell shapes is indicative of differences among models in the degree to which structural and material property changes affect composite performance. For example, the lateral spacing of the contour steps reflects the relationship between x-axis and REM values: if REM values increase more slowly than x-axis values —as in the upper half of the square tiled array graph (Fig. 16A), where contours are comparatively broad— changes in tile modulus have limited effect on the composite's REM (i.e. square is a more material-insensitive unit cell at large joint thicknesses). By contrast, when contour lines/REM values match x-axis values (i.e. contour lines are vertical and $E/E2^{0^\circ} = E1/E2^{0^\circ}$), changes in tile modulus have a direct and corresponding effect on the composite's REM. The more vertically oriented contours of the hexagon array graph therefore illustrate that the mechanical behavior of the hexagonal array is, on average, controlled to a larger degree by the composite's material properties.

In contrast, the vertical spacing of contour steps reflects the relationship between structural properties (i.e. joint thickness) and REM values. The tighter vertical spacing of contours on the lower right-hand side of all graphs illustrates that arrays become more sensitive to changes in joint morphology as tile and joint moduli diverge (i.e. at higher x-axis values). The square array's graph shows the tightest and most horizontal arrangement of contours in this region. This indicates that, in comparison with the other unit cells, and for a given high tile stiffness (i.e. high x-axis value), changes in joint morphology (vertical movements parallel to the y-axis) result in large changes in composite modulus (i.e. the composite is very geometry-sensitive). By contrast, hexagons (and to a lesser degree, triangles) are more influenced by both changes in geometry and material, a function of their contours' stable positive slopes. The narrowing of comparable graph contours (i.e. those representing the same z-value range) from square to triangle to hexagon also represents an increase in composite effective stiffness. Hexagons are therefore overall the most efficient shape in terms of the transfer of constituent material properties to composite modulus.

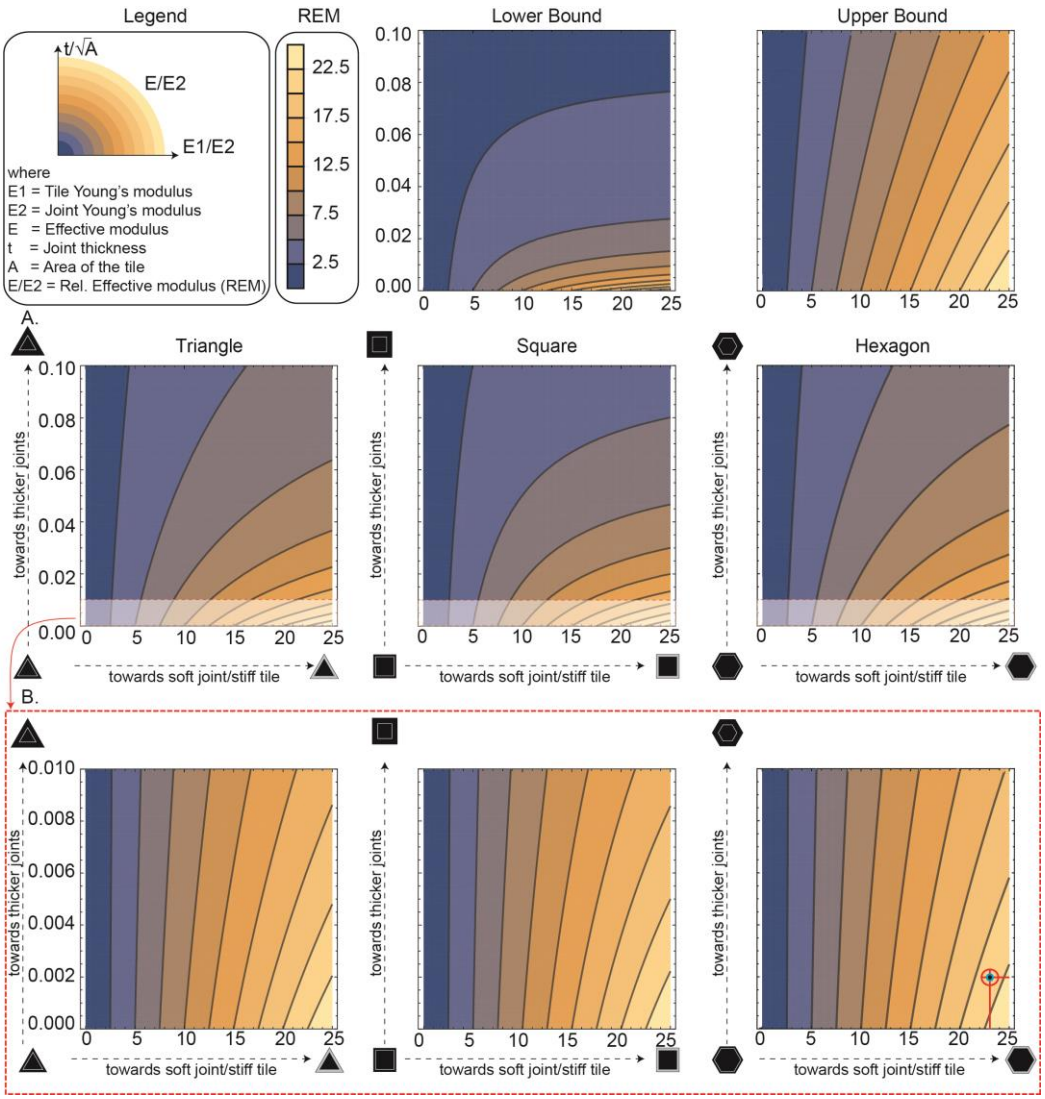

Figure 16: Relative Effective Modulus (REM) for all tile shapes, as a function of E1/E2 (x-axis) and t/√A (y-axis).

The legend for terminology and scale for all graphs is shown in the upper left corner; with increasing x-axis values, tiles become stiffer relative to joints, with increasing y-axis values, joints are thicker relative to tile size. The lower (Reuss iso-stress) and upper bounds (Voigt iso-strain) for the square tile are shown in the upper right corner; upper/lower bound graphs for triangle and hexagon tiles were similar. A. Contour plots for all shapes (y-axis scale: 0.0-0.1). B. A zoomed in view of the contour plot from Fig. 16A, to focus on more biologically relevant y-axis values (0.0 - 0.01). The biologically relevant x- and y-axis values — calculated from the structural and material properties of round stingray (*U. halleri*) tesserae— are marked by a red marker. Note that whereas hexagon result in the stiffest composite behavior overall (i.e. the REM values are highest for any given x-value), all tile shapes have similar contour patterns for the biologically-relevant range in B indicating little effect of unit cell shape on REM for thin joints (low y-axis values).

The maximum y-axis value in Fig. 16A represents comparatively thick joints (e.g. up to 10% of the square tile's side length), whereas those of the natural tessellated cartilage

system are quite narrow (~1/500 width of the tile ~0.002L; ~1/500 width of the tile ~0.002L; Seidel et al., 2016a). The contour plots in Fig. 16B present a more biologically relevant y-axis scale, from 0 to 0.01, indicated by the horizontal white bars in 3a; x- and y-values representing stingray (*U. halleri*) cartilage are marked with red dots in Figs. 16B and 17. In Fig. 16B, all tile shapes exhibit a fanned series of nearly vertical lines that, with increasing x-axis values, gradually tilted away from the y-axis. These nearly vertical contours signify that, when joints are thin, all models are more geometry-insensitive/material-sensitive systems, where material property (x-axis) changes are important, but there is little effect of changes in joint thickness (y-axis) on the REM of the composite. For very thin joints (i.e. Fig. 16B), the triangle model is slightly softer than the square model, a function of the shallower curves of its contours.

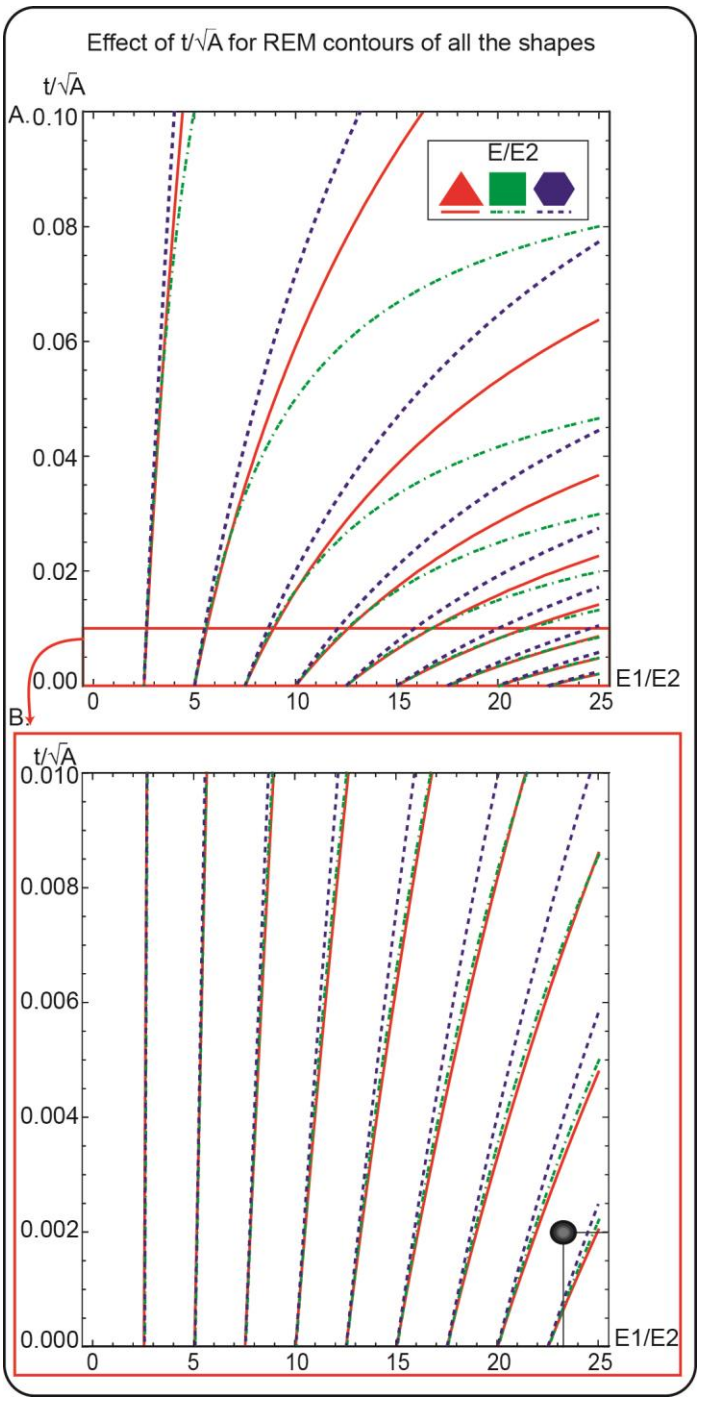

Figure 17: Comparison of the contour plots of all tile shapes from Fig. 16.

Contour lines originating from the same x-axis value (a contour line trio) correspond to the same z-axis value range (e.g. all lines in the first trio on the far left of 4A indicate REM = 2.5). The spread of contour line in a trio reflects the dissimilarity of the topography of the contour plots of the three tile shapes: in particular for the upper right portion of A, where joints are very thick and tiles are far stiffer than joints, the REM for hexagon is considerably higher than that of square. The narrower spread of contour lines in trios in biologically relevant range (B) indicates that unit cells exhibit more similar mechanical behavior at small y-axis values (e.g. narrow joints). A. Contour lines for all shapes (y-axis scale: 0.0-0.1); compare with Fig. 16A. B. A zoomed in view of the contour plot lines from Fig. 17A, to focus on more biologically relevant

y-axis values (0.0 - 0.01); compare with Fig. 16B. Values for the structural and material properties of round stingray (U. halleri) tesserae are marked by a black marker.

The degree of "geometry insensitivity" varies to some degree by shape: moving from triangle to square to hexagon the contours gradually incline more towards the left, indicating decreased susceptibility to changes in joint thickness (Fig. 17). For values of joint morphology measured from stingrays, however, these effects are minimal: from triangle to square to hexagon, the REM values only increase 1.45% of their x-axis (i.e. tile stiffness) values, from 90.77% to 91.45% to 92.22%. This is further illustrated in Fig. 18 in a two-dimensional graph of REM values for the biologically relevant morphologies ($t/\sqrt{A} = 0.002$). Overall, the similarity of the observed trends and the convergence of comparable contour lines near the x-axis of Fig. 17 indicate that the thinner an array's joints, the less of a role tile shape plays in composite stiffness.

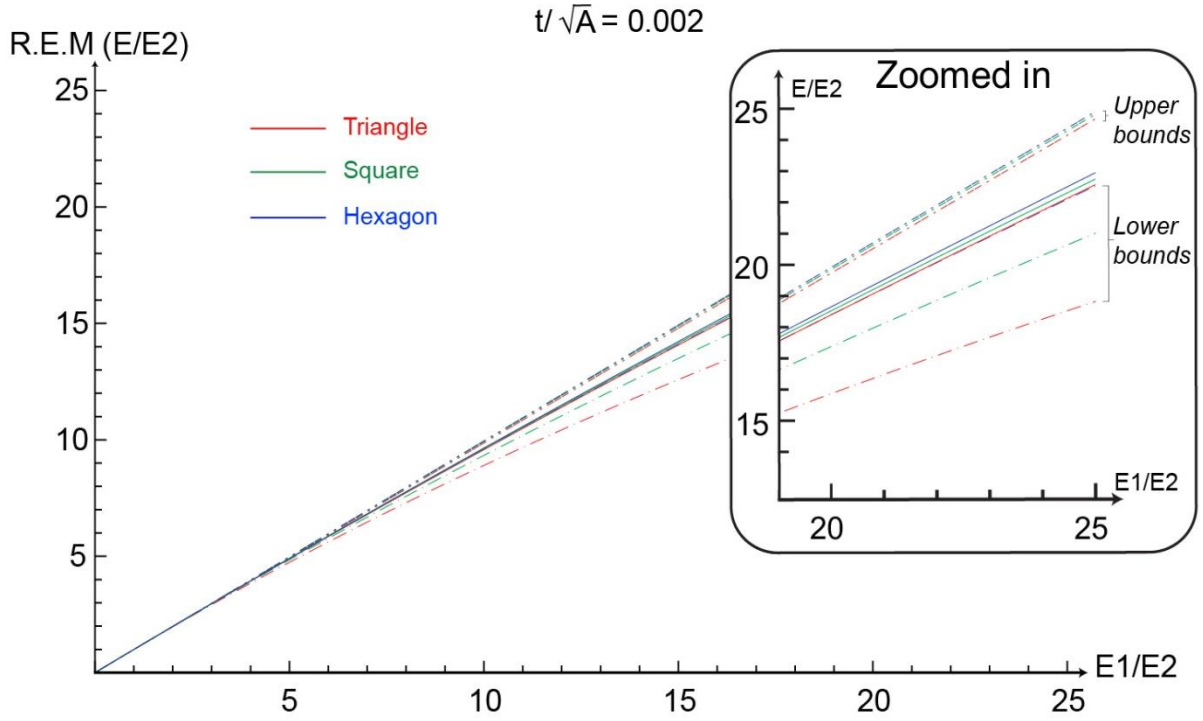

Figure 18: Two dimensional plot of REM at biologically relevant value of tesserae size.

Two-dimensional graphical representation of REM for all tile shapes when t/sqrt(A)= 0.002 (biologically relevant value, derived from *U. halleri* tessellated cartilage), showing the relationship between tile and composite modulus. The zoomed in pane shows the high correspondence of the three unit cells' lines, indicating similar mechanical behavior at small y-axis values (e.g. narrow joints). All shapes fall within their respective upper and lower bounds; note that the upper bound lines are nearly overlapping and the lower bound for hexagon is hidden beneath the REM line for the triangle array. The region above the

upper bound lines represents an unrealistic scenario where the composite is stiffer than its stiffest constituent (E>E1).

3.4 Conclusions

All examined models show stiffening of the composite when joint widths are minimized and/or tile stiffness is maximized. On average, however, the effective modulus of the square array is least sensitive and that of the hexagon array most sensitive to changes in model parameters. This suggests that square arrays would be less sensitive to structural/material variation (e.g. a wide range of $E1/E2^{0°}$ values results in the same effective modulus, particularly when joints are thick), whereas hexagon tiled arrays would be more "tunable". Square tiled arrays also allow the least return on material investment in terms of stiffness, whereas hexagon arrays provide a more optimized solution by maximizing the contribution of the harder tile material to the stiffness of the whole composite, being at a minimum 70.8% as stiff as their stiffest material for the range of values investigated here (as compared with 66.7% for the square unit cell). These differences are even more pronounced when other variables of tile shape are held constant (e.g. tile length or perimeter, rather than area; data not shown), but global trends among unit cell shapes are consistent, with hexagons always out-performing the other shapes in terms of composite stiffness. In models of geometric sutural interfaces, where joint thickness and volume fraction were held constant, stiffness increased as the length of sutural tooth edges in contact with joint material was increased, via addition of extra joint material to bond tooth tips to their corresponding troughs or via increases in tooth tip angle for teeth with bonded tips (Atkins et al., 2014; Balaban et al., 2015; Chen et al., 2014; Lin et al., 2014a; Lin et al., 2014b; Liu et al., 2014a; Seidel et al., 2014; Studart, 2012; Van Wassenbergh et al., 2015; Zhang et al., 2014). In contrast, in our models, for a given thickness of joint, hexagons —the tile that minimizes perimeter length for a given tile area— maximized composite model stiffness, by minimizing joint attachment surface and therefore the overall amount of joint material in the tiled composite. These observations on the mechanical efficiency of tiled composites are relevant to the laws constraining structuring of tiled biological materials, but also to manufacturing perspectives, where specific composite mechanical properties are desired.

The variable behaviors observed for different tile shapes when joints are thick do not apply for thin-jointed tile arrays, which converge on similar mechanical behaviors for the uniaxial loading regime simulated here. However, based on data showing the mechanical anisotropy of cellular solids (Ashby et al., 1995) and co-continuous composites (Wang et al., 2011), and given the large angle between the sides of square tiles, we would expect that square arrays would be particularly sensitive to variations in loading direction and, in biological systems, would only be found in areas with restricted loading orientation. This is supported by our observation of square tesserae in specific areas of the jaws of myliobatid stingrays (Dean, pers. obs.; Fig. 14b), directly beneath the tooth plates used to crush hard shelled prey with high, uniaxial bite forces (Kolmann et al., 2015; Summers, 2000b; Summers et al., 1998).

Square tesserae are, however, otherwise apparently not common in tessellated cartilage, with limited data on shark and ray cartilage tessellations suggesting that hexagons are the most common tiling elements (Dean and Schaefer, 2005; Dean et al., 2005; Fratzl et al., 2016a). Our data show that hexagonal tiles can, under some loading conditions, impart superior mechanical properties to composites, in comparison with square and triangle arrays. The effect of tile shape may be largely irrelevant in the biological system, however, considering that a recent survey of the tessellations of several shark and ray species suggested that intertesseral joints may, as a rule, be extremely narrow (Seidel et al., 2016a). The predominance of hexagonal tiles could also relate to factors besides mechanics, such as biological growth mechanisms. For instance, given that tesserae arise from seed mineralization centers and grow by mineral accretion at their margins (Dean, 2009; Dean et al., 2017a; Dean et al., 2009b; Seidel et al., 2016a), tesseral shape could also be regulated by the initial packing of mineralization seeds and/or variation in the local rates and uniformity of mineral deposition as tesserae and skeletal elements increase in size. In the latter case, tesserae with more sides could represent more uniform radial growth, whereas square tesserae would suggest a simpler biaxial growth pattern.

Our models provide theoretical groundwork for planned Finite Element simulations of more complex 3D tessellation models, but are currently only valid for in-plane, unidirectional loading (tension or compression), along the primary “vertical” axes of our unit cell shapes and for small resultant strains (see Appendix). Our results therefore give

only an estimation of the tensile/compressive properties of tiled composites under instantaneous loading without, for example, capturing non-linear effects of tile-tile contact on mechanics, which may play a fundamental role in the mechanics of tessellated cartilage (Fratzl et al., 2016a) and should also be very geometry dependent (Achrai and Wagner, 2013a; Achrai and Wagner, 2013b; Cadman et al., 2013; Chen et al., 2013; Chen et al., 2014; Ferrara et al., 2013; Liu et al., 2014a; Liu et al., 2014b; Yang et al., 2013a; Yang et al., 2013b; Zhang et al., 2013b; Zhang et al., 2013a). Our future studies will incorporate more detailed investigation through FE simulations and mechanical testing of 3D printed models, as well as the effects of off-axis loading, including shear and Poisson's ratio effects, to better approximate the features of the biological tilings under study and provide insight into tiled composite architectures in general.

4. Phase 2

The phase 2 project is currently under review as a paper titled *"Hierarchical mechanical analysis of stingray inspired tessellations: Implications for skeletal mechanics and biomimetic design"* where I am the first author.

4.1

The skeletal system of sharks and rays (elasmobranch fishes) consists predominantly of unmineralized cartilage (Dean et al., 2009a; Kemp and Westrin, 1979a; Seidel et al., 2019b), a skeletal tissue far less stiff than bone (Wegst and Ashby, 2004a). Unlike mammalian cartilage, however, elasmobranch cartilage is wrapped with a layer of minute, mineralized, polygonal tiles called tesserae, forming a surface shell (Fig. 19A-D) (Clement, 1992b; Dean et al., 2015; Dean et al., 2009a; Kemp and Westrin, 1979a; Seidel et al., 2019b). The composite nature of tessellated cartilage is hypothesized to enhance the mechanical properties of the unmineralized cartilage, particularly through the combination of soft and hard tissues in distinct geometric configurations (Seidel et al., 2019b), but this has never been demonstrated unequivocally. Tesserae are linked by unmineralized, collagenous joint fibers (Fig. 19F, H), which, when the skeleton is under tension, are predicted to allow tesserae to pull apart, loading the fibers primarily (Fratzl et al., 2016b; Seidel et al., 2017a). In contrast, under compression the hard tesserae are expected to come into contact, stiffening the skeleton locally (Fratzl et al., 2016b; Liu et al., 2010b; Liu et al., 2014b). In this way, tesserae and their tissue associations are believed to allow tessellated cartilage to be either flexible or rigid, depending on the nature of the applied loads (Fratzl et al., 2016b; Liu et al., 2010b; Liu et al., 2014b; Seidel et al., 2019b).

The role of the distinct tessellation in load management in shark and ray cartilage has been explored using both physical and computational methods, typically at two disparate size scales: either investigations of whole skeletal elements that disregard the tessellated nature of the mineralized layer or investigations of the interactions of individual tesserae, largely ignoring the geometry of the skeleton. The larger-scale, physical experiments have used mechanical testing techniques like flexural bending,

tension and compression tests and small scale testing like nano-indentation confirm that tesserae add stiffness to the cartilage (Balaban et al., 2014; Liu et al., 2014b; Macesic and Summers, 2012; Wilga et al., 2016b). This is further supported by morphological studies, which show tesserae tend to be thicker in regions where high stresses are predicted to occur (Balaban et al., 2014; Dean et al., 2017b; Seidel et al., 2016b; Wilga et al., 2016b), with some species exhibiting multiple layers of tesserae (Dingerkus and Seret, 1991; Seidel et al., 2017b; Summers, 2000a; Summers et al., 2004).

In contrast, our understanding of the smaller scale, mechanical behaviors and interactions of tesserae is less developed, largely due to the inherent technical difficulties in subjecting tesserae to mechanical tests due to their small size (typically ≤500 μm width and their joints ≤2 μm at their narrowest; Fig. 19 E, F), complex structure, and covering by a fibrous layer (perichondrium) (Dean et al., 2009a; Seidel et al., 2017a; Seidel et al., 2016b). As a result, computational/analytical models have been most helpful in predicting form-function relationships at smaller size scales in tessellated cartilage. For example, a simplified analytical model of the tessellated cartilage cross-section predicted that during compression, stresses will tend to be concentrated in the tessellated layer rather than the unmineralized cartilage (Liu et al., 2010b). This hypothesized 'stress-sink' behavior for tesserae was also supported by larger scale computational structural analyses performed on models derived from CT scans of shark jaws and simulating biological loading conditions (Ferrara et al., 2011b; Wroe et al., 2008b). One of these models also showed that stresses would tend to be lower in jaws composed of tessellated cartilage as compared to jaws modeled in bone, although tissue strains were predicted to be higher (Wroe et al., 2008b). Lastly, in the only study to examine the mechanical effects of tesserae properties on the mechanics of the tessellated cartilage composite, parametric, 2d analytical models of tesserae demonstrated that variations in tesserae geometry and material properties should translate into differences in effective stiffness of the composite at larger scales, suggesting that emergent skeletal properties can be tuned through local structural/material variations at the tesseral level (Jayasankar et al., 2017b).

Computational studies have therefore been important in predicting the role of tesserae in the management of stresses, beyond simply providing stiffness to the underlying unmineralized cartilage. However, all smaller-scale studies of tessellated cartilage mechanics have relied on extremely simplified models of tesserae, which were only two-

dimensional and assumed tesserae to have homogeneous material. However, a recent study showed that tesserae are not simply solid blocks, but rather exhibit complex three-dimensional ultrastructures and local material variations (Fig. 19E, F; see description in Methods below) (Seidel et al., 2016b). In order to better capture the fine scale mechanics of tessellated cartilage, the current work employs 3d models that incorporate the recent, high-resolution ultrastructural and material information obtained from the tessellated cartilage from the round stingray, *Urobatis halleri* (Seidel et al., 2016b). Through parametric CAD modeling, natural ultrastructure and material property variations were simulated and the resultant computational models subjected to finite element analysis (FEA). This allowed evaluation of stress patterns occurring within tesserae during loading, to determine the effects of various tesserae ultrastructural features on mechanics.

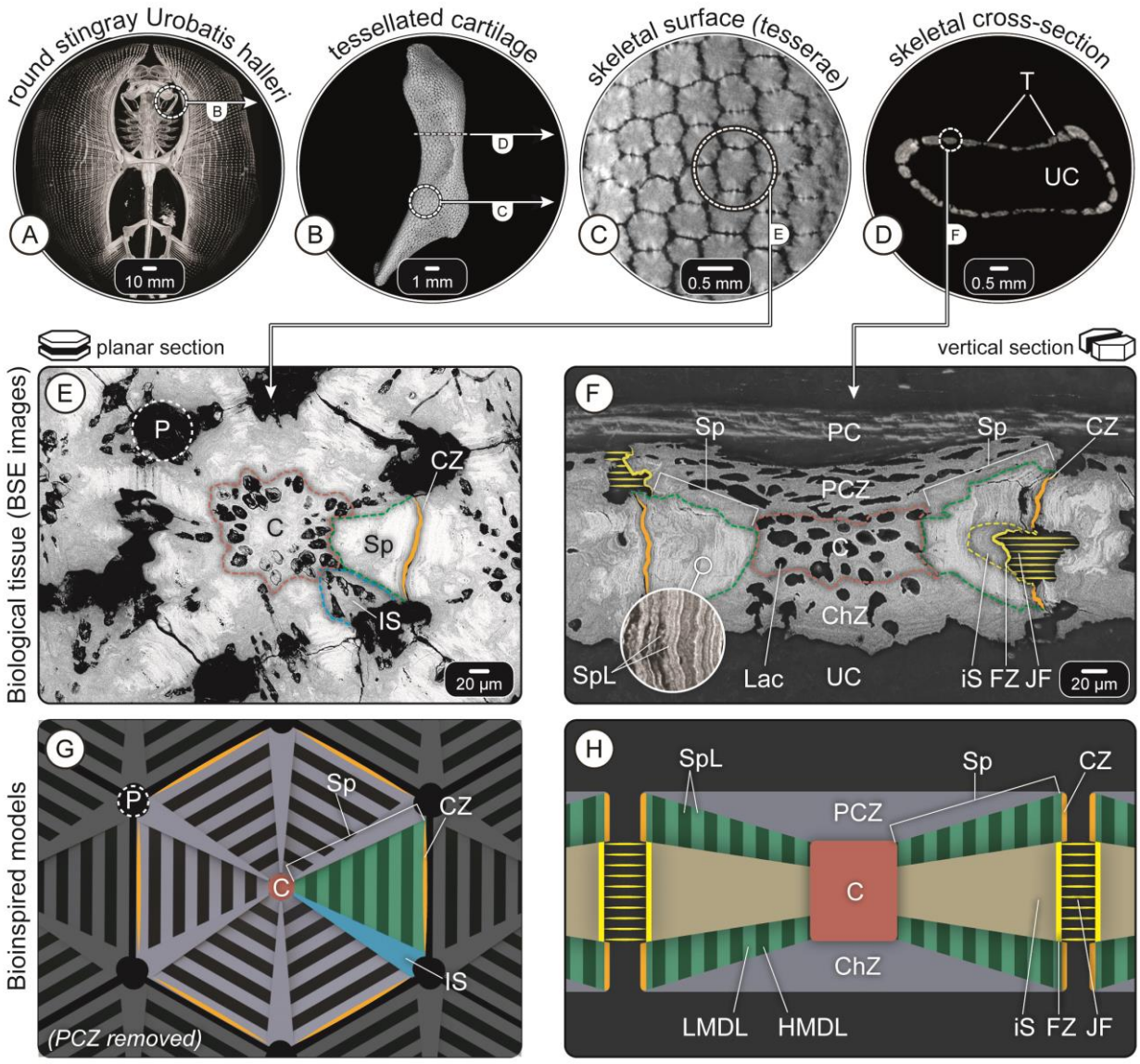

Figure 19: Tessellated cartilage of stingray skeleton and biological translation.

The skeleton of sharks and rays (A-B) is covered with mineralized tiles, called tesserae, roughly hexagonal in surface view (C) and rectangular in transverse cross-section of the skeleton (D). A planar section within the plane of the tesseral mat (E) and a vertical cross-section of a tessera (F), illustrate their diverse ultrastructural components and the joint fibers connecting adjacent tesserae. Corresponding translation sketches of planar and vertical cross-sections are shown in (G) and (H), respectively, with abbreviations (used in all Figures) listed at the bottom of the Fig. Note that the perichondral zone (PCZ) is removed in (G) so that the spokes (Sp) are visible. A-D: MicroCT images; E-F: Backscatter electron microscopy images. Note that these techniques only visualize hard tissues (tesserae) here and not fibrous tissues, such as the joint fibers between tesserae. Panels A-F obtained from

4.2 Methods: Phase 2

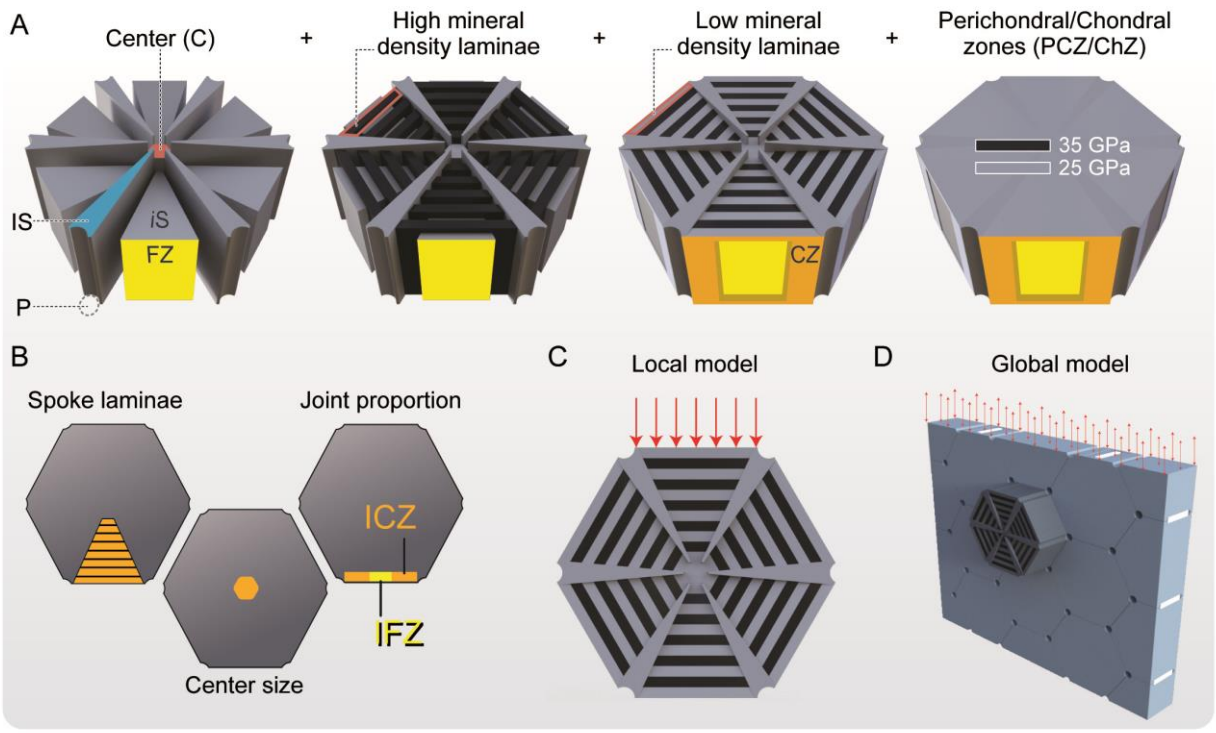

Figure 20: Multiscale models of tesserae constructed in this study.

A) Step-wise construction of tesseral ultrastructure, assigning biologically-relevant material properties; color-coding and abbreviations are the same as Fig. 19. B) Ultrastructural factors (lamina number, center radius and contact surface area) varied parametrically in the local model, to derive their effect on net effective stiffness of tesserae. C) Local model (single tessera, including ultrastructural features) - note that the perichondral zone (PCZ) has been removed, as in Fig. 19G. D) Global model (multi-tesserae array), where tesserae are assigned a homogeneous material property, derived using the local model (see text).

The mineralized tessellated layer was modeled at two length scales (Fig. 20), described in detail below. In a “local” model (Fig. 20C), we investigated the effect of ultrastructural variation on stress distribution and effective stiffness (see below) of individual tesserae (i.e. not including joint material). In the larger scale "global model", we constructed a tessellated array, containing monolithic tesserae with material properties determined from the local model and also incorporating joint material between tesserae (Fig. 20D). This allowed investigation of how local, within-tesserae features relate to the material behavior of tessellations at a larger size scale.

Both the local and global tesserae models were constructed in a commercial computer-aided design (CAD) package, Rhinoceros 3D Version 5 (Robert McNeel & Associates,

Barcelona, Spain), coupled with Grasshopper 3D (0.9.0076), a plug-in for algorithmic programming that allowed ultrastructural features to be varied parametrically (see below).

4.3 Local model: Parametric modeling of tesserae ultrastructure

Natural ultrastructure

Tesserae are polygonal, mineralized tiles that are predominantly six-sided (i.e. bordered by six neighboring tesserae) (Baum et al., 2019)and are typically wider than deep (Dean et al., 2009a; Jayasankar et al., 2017b; Seidel et al., 2016b). As such, they can be considered to be roughly hexagonal when sectioned in the plane of the tesseral mat (planar section: Fig. 19E, G) and rectangular in transverse cross-sections of the skeleton (vertical section: Fig. 19F, H). Tesserae comprise several distinct structural regions, the arrangements and structural features of which acted as guides for our model construction. The summary of tesserae ultrastructure in the paragraph below is synthesized from numerous works which focused predominantly on tesserae from the stingray *Urobatis halleri (Dean et al., 2009a; Dean et al., 2010; Seidel et al., 2017a; Seidel et al., 2016b)*; however, these features of tesserae seem to be largely universal among different species. Anatomical terminology, abbreviated in italics below, is illustrated in Fig. 19 and used throughout the figures.

The tesseral center region (*C*: Fig. 19E-H) occupies the approximate center of mass of the tessera. Extending outward from the center are the 'spokes' (*Sp*: Fig. 19E-H): high mineral density wedges, radiating from the center toward the joints with adjacent tesserae. Intervening between spokes are wedge-shaped 'interspoke' (between spoke) regions (*IS*: Fig. 19E, G); these are a lower mineral density than spokes and communicate to the pores (*P*: Fig. 19E, G) at the vertices of tesserae, rather than the joint surfaces at the tesseral sides. The alternating pattern of spoke and interspoke regions pinwheeling around the tesseral center resembles spokes on a wheel in planar sections (Fig. 19E, G). Spokes are characterized by thin plate-like lamellae (2-3 μm) arranged parallel to the tesseral joint surface. Spoke laminae (*SpL*) alternate between higher and lower mineral density lamellae (*HMDL*, *LMDL*), giving spokes a banded appearance. In vertical sections, spokes often enclose a pyramidal 'intraspoke' (within spoke) region (*iS*: Fig. 19F, H),

comprised of lower mineral density material (similar to interspoke regions) and also communicating to the joint space between tesserae. Between the center region and the outer fibrous perichondrium (*PC*: Fig. 19F) is the perichondral zone of the tessera (*PCZ*: Fig. 19F, H) and between the center and underlying unmineralized cartilage (*UC*: Fig. 19F) is the chondral zone of the tessera (*ChZ*: Fig. 19F, H), both zones with mineral densities similar to inter- and intraspoke regions. All non-spoke regions within tesserae (i.e. center, interspoke, intraspoke, perichondral and chondral regions) are perforated by spheroidal cavities (*Lac*: lacunae, 15-20 μm long), which contain cells and unmineralized matrix.

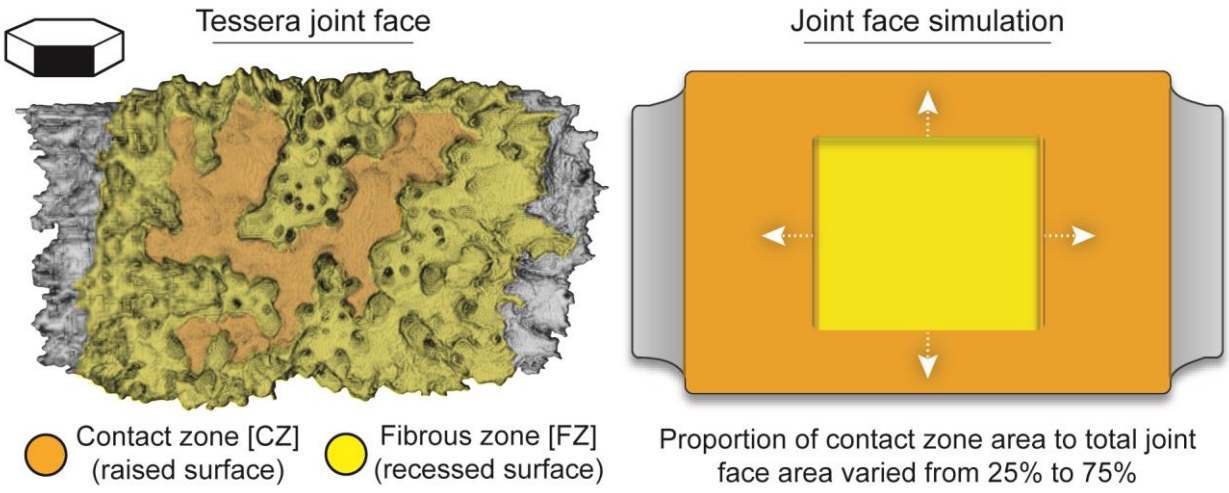

Figure 21: Biological structure (left) and corresponding model (right) of the complex tesseral joint face.

The joint face comprises a flattened, raised region where neighboring tesserae are in contact (contact zone) and a recessed zone where fibrous tissue links neighbors (fibrous zone). The proportion of the joint face occupied by the contact and fibrous zones is reciprocal and in the constructed local model, this could be changed parametrically. Color coding is the same as Fig.s 19 and 20; compare with those figures and note that the contact zone is associated with spokes (Sp), whereas the fibrous zone is associated with the intraspoke region (iS). Both images show a lateral, 'neighbor's eye' view of a tessera. Left image is a pseudo-colored microCT image.

The joints between tesserae are anatomically complex (Fig. 21) and deserve careful consideration from a modeling perspective. The edges of tesserae which border the joint space are comprised of two anatomical regions with distinct morphologies and tissue associations (Figs. 19E-H, Fig. 21A). Where neighboring tesserae come into physical contact, there is a largely flat "contact zone" (*CZ*: Fig. 19E-H), always associated with and flanked by spokes in the tessera. In contrast, the "fibrous zones" (*FZ*: Fig. 19E-H), where

collagen joint fibers (*FB*) tether neighboring tesserae to one another, are recessed and flanked by intraspoke tissue in the tessera. The morphologies and interactions of these two zones on the joint face of a tessera are elaborate, with fibrous and contact zones interweaving considerably (Fig. 21). However, the flanking of contact zones by spoke material and fibrous zones by non-spoke material appears to be a diagnostic feature of tesserae (Seidel et al, 2016).

4.4 Local model construction

In the local model, a tesserae was modeled as a hexagonal block, with the geometries and dimensions of tesseral ultrastructures modeled according to those observed in tesserae from the stingray *Urobatis halleri* (Table 1) (Dean et al., 2009a; Seidel et al., 2016b). The different ultrastructural regions (e.g. spoke, interspoke regions) were modeled as separate pieces and then assembled together to form the complete, integrated tessera (Fig. 20A). This assembly process facilitated the parametric variation of the dimensions and properties of individual ultrastructural features. We describe the arrangement of features and their assembly below, including the same anatomical abbreviations listed in the paragraph above.

The tesseral center (*C*) was modeled as a polygon at the geometric center of the tessera, with wedge-like spoke (*Sp*) and interspoke (*IS*) regions radiating from its vertices towards the outer edges of the tesserae (Fig. 20A). To accommodate the intraspoke (*iS*) region (described below), spokes were modeled with an internal, pyramid-shaped cavity, with the base at the tesseral edge and the tip extending toward the tesseral center. Spokes were divided into laminae of equal thickness parallel to the joint face. Laminae were assigned high or low moduli (*HMDL*, *LMDL*; see below) in alternating order to mimic the banding pattern of alternating high/low mineral density and material properties observed in *Urobatis* tesserae (Fig. 19F) (Seidel et al., 2019c). Both the first lamina near the center and the last lamina at the joint face were assigned a low modulus. This mimicked the biological condition where newly deposited material at tesseral edges has a lower mineral content and material stiffness (Seidel et al., 2019c). Semi-circular cavities were hollowed out at the tesseral vertices (i.e. the distal ends of the interspoke regions) to mimic the pores (*P*) often observed at the intersection points of multiple tesserae in natural tessellations (Fig. 19E, G) (Maisey, 2013a; Roth, 1911; Seidel

et al., 2016b). The tessera model was completed by adding the perichondral and chondral zones (*PCZ*, *ChZ*) on the top and bottom of the tessera, respectively. The addition of these regions creates the planar surfaces of the top and bottom of the model (compare the 3rd and 4th images in Fig. 20A). The lacunar cavities (Fig. 19F), typically present in all non-spoke regions in tesserae, were not modeled, as the 3D structure and material properties of these cavities and their tissues have not yet been described.

The distal end of the intraspoke region was recessed relative to that of the spoke region in order to create a simplified joint surface that captured the primary structural characteristics of the joint face (Fig. 21), while facilitating efficient finite element analysis. In our local model, the distal end of the spoke (i.e. the lamina at the intertesseral joint-end of the spoke) served as the contact zone surface (*CZ*: orange region in Figs. 20A, 21), whereas the distal end of the intraspoke region served as the recessed and rectangular fibrous zone (*FZ*: yellow region in Fig. 20A, 3). In this way, as in the biological system, the contact and fibrous zones were modeled as distinct, but closely associated regions, flanked by different materials. In the 'global model' described below, which models a full tessellation, fibrous joint material is fully bonded to the intraspoke regions to connect tesserae to their neighbors.

4.5 Ultrastructural variations in tesserae

To investigate the effects of ultrastructure on performance (tesserae stiffness and intratesseral stress distribution), three key ultrastructural features were varied in our parametric models (Fig. 20B): 1) the number of laminae in a spoke, 2) the size of the center region (center radius) and 3) the area of the contact zone surface in proportion to the fibrous zone surface. These three ultrastructural variables were chosen to represent the natural variation in tesseral ultrastructure observed among different species of elasmobranch (Fig. 22) (Seidel et al., 2016b). The morphologies of the selected ultrastructural features were varied through a wide range that included morphologies previously observed for tesserae of the stingray *U. halleri* (Table 1; natural character states are marked in red in Fig. 23).

4.5.1 Varying lamina number

Tesserae increase in size as the animal grows, via deposition of new material at their margins (Dean et al., 2009a; Seidel et al., 2016b). As a result, spokes also increase in length with age via the addition of new laminae and therefore the thickness of laminae relative to spoke length varies. In our model, the lamina number was changed by subdividing the spoke along its long axis into different numbers of laminae of equal thickness. The wedge-like shape of spokes, however, meant that laminae decreased in volume from edge to center.

The lamina number was varied from 5, 11, 15, 21, 51 to 151. The chosen values for lamina number were all odd in order to maintain the presence of soft laminae at the outer rim and adjacent to the center. In *U. halleri* tesserae, spoke laminae are 2.52 ± 1.0 µm thick (Seidel et al., 2019c) and therefore the 151-laminae condition (with each lamina having a thickness of ~1 µm) is the most biologically relevant model.

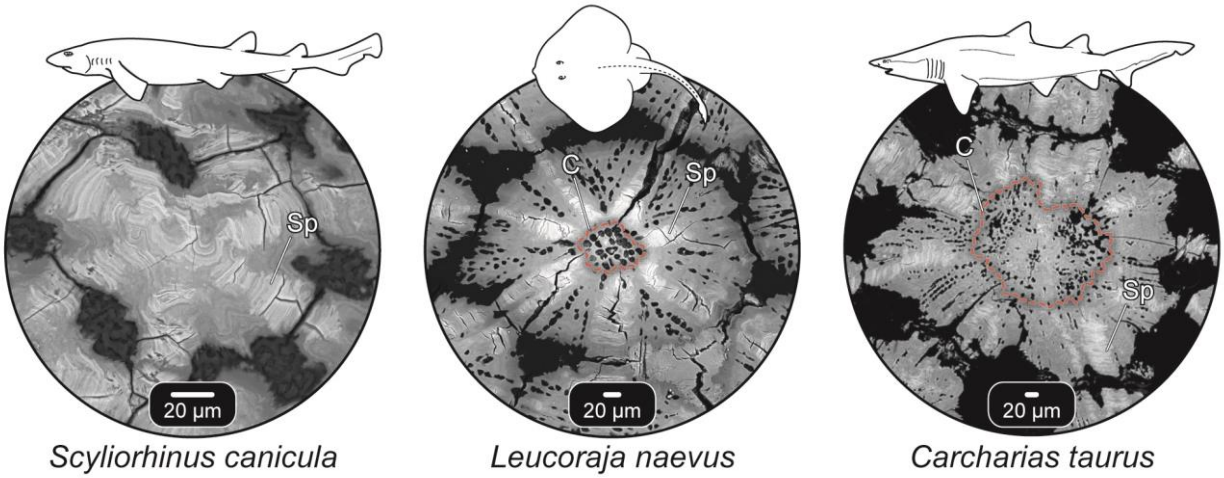

Fig. 22: Natural variation of tesseral ultrastructural features in two species of shark and a skate. Note the variation in the size of the center region (C; outlined in red), the predominance of spokes (Sp), and cellularity (the black holes in tesserae are lacunar spaces, where cells are housed in life).

4.5.2 Varying center size

In the natural system, across species and across age, the proportion of tesseral diameter occupied by the center region is variable (Fig. 22) (Seidel et al., 2016b). In our model, because interspoke and spoke regions are linked to the center region, changes in center diameter result in concomitant inverse changes in the length/volume of interspoke and

spoke regions (i.e. a larger center results in shorter spokes). To investigate the mechanical effect of different center sizes, the diameter of the center was varied from 90, 25, 20 to 15 microns (~40%, 10%, 8% and 6% of tesseral diameter). Tiles with centers 20 µm in diameter (~8% of tesserae diameter) were the most biologically relevant models (Seidel & Dean, pers. obs.).

4.5.3 Varying contact zone area

The complex physical interactions of adjacent tesserae at their joints are expected to play an important role in tessellated cartilage mechanics (Baum et al., 2019; Fratzl et al., 2016b; Seidel et al., 2016b). In our models, each joint face is comprised of a reciprocal combination of contact zone and fibrous zone area. To investigate the effect of this interaction on tesserae stiffness, the contact zone area was varied in proportion to the fibrous zone area, from 25%, 50% to 75%. A contact zone proportion of 50% was the most biologically relevant (Seidel & Dean, unpublished data). As spoke and intraspoke regions are associated in our models with the contact and fibrous zones, respectively, increase in contact zone area resulted in a concomitant increase in spoke volume, decrease in fibrous zone area and decrease in intraspoke volume.

Tesserae (*T*)	width: 448 µm	height: 200µm
Fibrous zone (*FZ*)	width: 180 µm | 40%	height:121 µm | 60.5%
Contact zone (*CZ*)	width: 218 µm | 48%	height:200 µm | 100%
Center (*C*)	radius : 20 µm | 4%	height : 155 µm | 77%
Spoke (*Sp*)	height at center: 155 µm | 77%	height at edge: 200 µm | 100%

Table 2: Ultrastructural features, their dimensions, and their proportions with respect to tesserae dimensions. Ultrastructural dimensions are derived from previous anatomical descriptions of tesserae from the stingray *Urobatis halleri* (see text).

4.6 Finite Element Analysis

Two versions of the local model were used to address the contribution of individual structural and compositional features to tesserae mechanics (Table 2). The model versions differed only slightly: the “bio-model” exhibited ultrastructural features most similar to *U. halleri* tesserae (151 laminae, 20µm center, 50% contact area), whereas the “base model” was a simplified version of the bio-model, with the same dimensions and features, but only 51 laminae. The base model required considerably less computational power as a result of its fewer laminae; this time-saving modification was used where possible, because lamina number was shown to have little effect on tesserae properties (see Results). Table 2 outlines which model version was used in which experiment: The bio-model was used to investigate stress distribution and overall performance of tesseral ultrastructures during loading, whereas the base model was used to study the effects of ultrastructural feature variation on tesserae stiffness (e.g. variation in lamina number, center radius or contact surface area).

Structural features	Base model	Bio model
No. of laminae	**51**	**151**
Center radius	20 µm	
Contact surface area	50%	
Variables tested	**Base model**	**Bio model**
Lamina number (Fig. 23)	5, 11, 15, 21, **51**, **151**	
Center radius (Fig. 23)	90, 25, **20**,15 µm	-
Contact surface area (Fig. 23)	75%, **50%**, 25%	-
Maximum Stress (Fig. 24)	-	✔
Strain energy density (Fig. 25)	-	✔
Stress transect (Fig. 26)	0, 5, 21, **151**	

Table 3: Variations on the local model used for finite element analysis (FEA).

The base and bio-models are defined in the top rows of the table; these models differed only in lamina number. The base model was used when possible to reduce analysis time. Each FEA experiment is placed in the column of the model used and figures where results are shown are listed. For experiments where

ultrastructure was varied parametrically, morphological iterations are listed. Relevant base and bio-model values are listed in green and red respectively. Since base and bio-models differed only in lamina number, experiments where lamina number was varied span both columns.

The models listed in Table 2 (including all parametric iterations for each of the three chosen ultrastructural features) were constructed and exported from Rhinoceros in SAT file format into a finite element analysis package (ABAQUS Version 6.13 Dassault Systèmes, Waltham USA). All components shown in Fig. 20A were modeled as fully bonded with each other. The models were meshed with 10-node quadratic tetrahedral elements (C3D10). After a mesh sensitivity test, the global seeding size was set at 0.015 µm, with each model having a degree of freedom from [3 x minimum node number] to [3 x maximum node number] (see Appendix A.8).

In the local model, each tessera ultrastructure was assigned linearly elastic properties and Poisson's ratio of 0.3 (Zhang et al., 2013a). Mineralized tissue moduli were obtained from a nanoindentation study of stingray tesserae (Seidel et al., 2019c). All tesserae ultrastructures were assigned a modulus of 25 GPa except for the hard laminae in spokes, which were assigned a higher modulus of 35 GPa . The model was constrained at the bottom joint surface and a uniform displacement boundary condition was applied to the top of the model in the y-direction (along the top-bottom axis). The displacement boundary condition simulated an equivalent strain of 1.3%, compressing the tessera in the y-direction.

4.7 Mechanical Performance Assessment

To understand the mechanical role played by each ultrastructural component, the mechanical behavior of the local model was assessed using several metrics. The model's volume-averaged stress ($\bar{\sigma}_{yy}$) in the loading direction was quantified, with

Equation 4

$$\overline{\sigma}_{yy} = \frac{\sum_{i=1}^{n} \sigma_{yy}^{i} \cdot V_{yy}^{i}}{\sum_{i=1}^{n} V_{yy}^{i}}$$

where $\overline{\sigma}_{yy}$ is the stress in the y-y loading plane, V_{yy}^{i} is the volume of each element and i represents the element number. As a representation of maximum stress (σ_{yy}^{Max}), the

average of the top 10% of stress values was calculated. This was used rather than the absolute maximum in order to have a volume-averaged significance rather than a single value and to avoid singularities, if present.

Additionally, the average strain energy density was calculated for loaded tesserae models using the standard ABAQUS output variable identifier, SENER:

Equation 5

$$\textbf{\textit{Strain energy density}} = \frac{\sum_{i=1}^{n} \boldsymbol{SENER \cdot V_{yy}^{i}}}{\sum_{i=1}^{n} \boldsymbol{V_{yy}^{i}}}$$

Strain energy density (strain energy normalized by volume) is a common measure of energy absorption, approximating also the relationship between stress and strain in a structure or material (Sih and Macdonald, 1974). Strain energy density is also a proxy for the extremes of material performance, predicting possible failure regions and areas of crack propagation in materials (Fratzl et al., 2007b).

Additionally, to evaluate the contribution of ultrastructural variation to whole tessera mechanical behavior (and to facilitate construction of the global model, see Section 2.2), a single homogenized effective modulus (E_{eff}) for tesserae was calculated from the most biologically relevant, heterogeneous single tessera model (local model). This effective modulus captures in a single value the mechanical contributions of the complex heterogeneous features modeled within the tesserae, by assuming the heterogeneous tessera will bear the same energy as a tessera of E_{eff} under the same boundary conditions (Chen et al., 2017). With the linearly elastic materials used in our models, the ratio of strain energy density experienced by two tesserae of different material properties loading under the same testing/boundary conditions is proportional to the ratio of their moduli. We exploit this to calculate the homogenized effective modulus (an unknown) by comparing in ABAQUS the strain energy density of the heterogeneous local tessera model with that of a homogeneous tessera of arbitrary mechanical properties modeled:

Equation 6

$$E = \frac{W_{Base\ model}}{W_{Homogeneous\ model}} * E_{Homogeneous\ model}$$

where $W_{Base\ model}$ is the elastic strain energy density of the local bio-model and $W_{Homogeneous\ model}$ is the elastic strain energy density of a tessera of equal volume composed of an arbitrary single material ($E_{Homogeneous\ model}$ = 35 GPa). To verify that the substitutive material (E_{eff}) accurately mimics the energy storage of the biological model, a tessera comprising only effective modulus material was modeled in ABAQUS and its strain energy density derived as in Equation 3.

The effective modulus of whole tesserae was calculated for each of the 13 varied-ultrastructure models. The homogenization method for calculating effective modulus is more relevant for the current work than the traditional Hashin-Strikman method, which calculates effective modulus using only the volume fraction of constituent materials, thereby ignoring any mechanical effect of ultrastructures formed by the different materials (Chen et al., 2017).

Finally, to understand the mechanical role of spoke laminae, the stress at maximum strain was plotted along a path running through the tessera along the loading axis: starting from the loaded contact surface, traversing the spoke to the tesseral center and then exiting distally through the contralateral spoke (see Fig. 27). The stress values as a function of position along the path were plotted for four tesserae models: models with 5, 21, and 151 laminae and a tessera with uniform material property of 25 GPa (i.e. a model with zero spoke laminae).

4.8 Global model: Integration of the local tesserae model into the tesseral matrix

4.8.1 Construction of the global model

A tesseral mat was created using Grasshopper and Rhino, by assembling tesserae with the same structural dimensions as the base model into a 3 by 3 array (Fig. 20D). Tesserae were 1μm apart from each other and connected to their neighbors using a soft,

fibrous joint material projecting from the fibrous zone surface of the intraspoke region (yellow region, Figs. 20A, 21). To facilitate computation, tesserae were modeled as homogeneous (i.e. lacking ultrastructure) and assigned the effective modulus material property (E_{eff} = 26.1 GPa, determined from the homogenization above; see Results) and the Poisson's ratio was modeled as 0.3, common for models of biological tissues (Zhang et al., 2013a).

The material property of the fibrous joint material in the biological tissue is unknown, but due to its construction from parallel-aligned collagen fibers (Clement, 1992b; Dean et al., 2009a; Seidel et al., 2017a) it is hypothesized to be very stiff under tension and soft under compression (Fratzl et al., 2016b; Seidel et al., 2019b) and therefore highly non-linear. To capture this behavior, we constructed a hypothetical material model using the ABAQUS material library, combining the stress-strain curves of tendon in tension (Maganaris and Paul, 1999) and mucosa under compression (Chen et al., 2015b).

The 2nd order Ogden hyperelastic material model provided the closest fit to our composite curve and so was used as our intertesseral fiber material (see Appendix A.12).

The tesseral mat was loaded in both tension and compression while constrained at the bottom surface (Fig. 20D). Similar to the local base model, a 1.3% uniaxial strain was applied within the plane of the tesseral mat. The stress in the tesseral mat was calculated using Equation 2 and stress-strain curves were plotted for both tension and compression. In addition, for comparative purposes and to demonstrate the role of material and structural properties in the mechanics of the tesseral array, three additional models were created where tesserae were modeled with (1) lower stiffness material (25 GPa), (2) higher stiffness material (35 GPa), or (3) with intertesseral joints that were twice as wide as those in the base global model.

4.9 Results and Discussion

4.9.1 Local model: Ultrastructural variations

The hexagonal structure of the modeled tessera has a high tolerance to structural changes or defects, as demonstrated by the fact that not all modeled ultrastructural

variations produced demonstrable effects on tesseral mechanical properties. The variation in spoke lamina number and center radius had essentially marginal effect on the effective stiffness (E_{eff}) of the tessera, which varied less than 1% across models, remaining ~26.1 GPa (Fig. 23A-B). This lack of change is likely a function of the design constraints of the tesseral model (see 2.1 Local model). The majority of the tessera model is comprised of lower modulus material (LMM: 25 GPa); therefore, any increase in the proportion of higher modulus material (HMM: 35 GPa) will increase in tesseral effective stiffness. However, HMM in our model is found only in spokes, the structure of which is not greatly affected by our modeled changes in lamina number or center radius. For example, when the number of laminae was varied from 5 to 151, the volume fraction of hard material (VF_{hard}: volume of HMM relative to whole tessera volume) only increased by 4% (VF_{hard} 5 lamina = 15% vs. VF_{hard} 151 lamina = 19%). The increase in VF_{hard}, however, is not large enough to alter the effective stiffness of the tessera. The increase of VF_{hard} with increasing lamina number (Fig. 23A) is due to the spokes being wedge-shaped structures (in both planar and vertical sections; Figs. 19-20). When there are few laminae, spokes are dominated by the material of the outermost lamina (LMM in our models). However, as the number of laminae increases (i.e. laminae became thinner), the volumetric proportion of higher and lower modulus material in spokes converges on 50%.

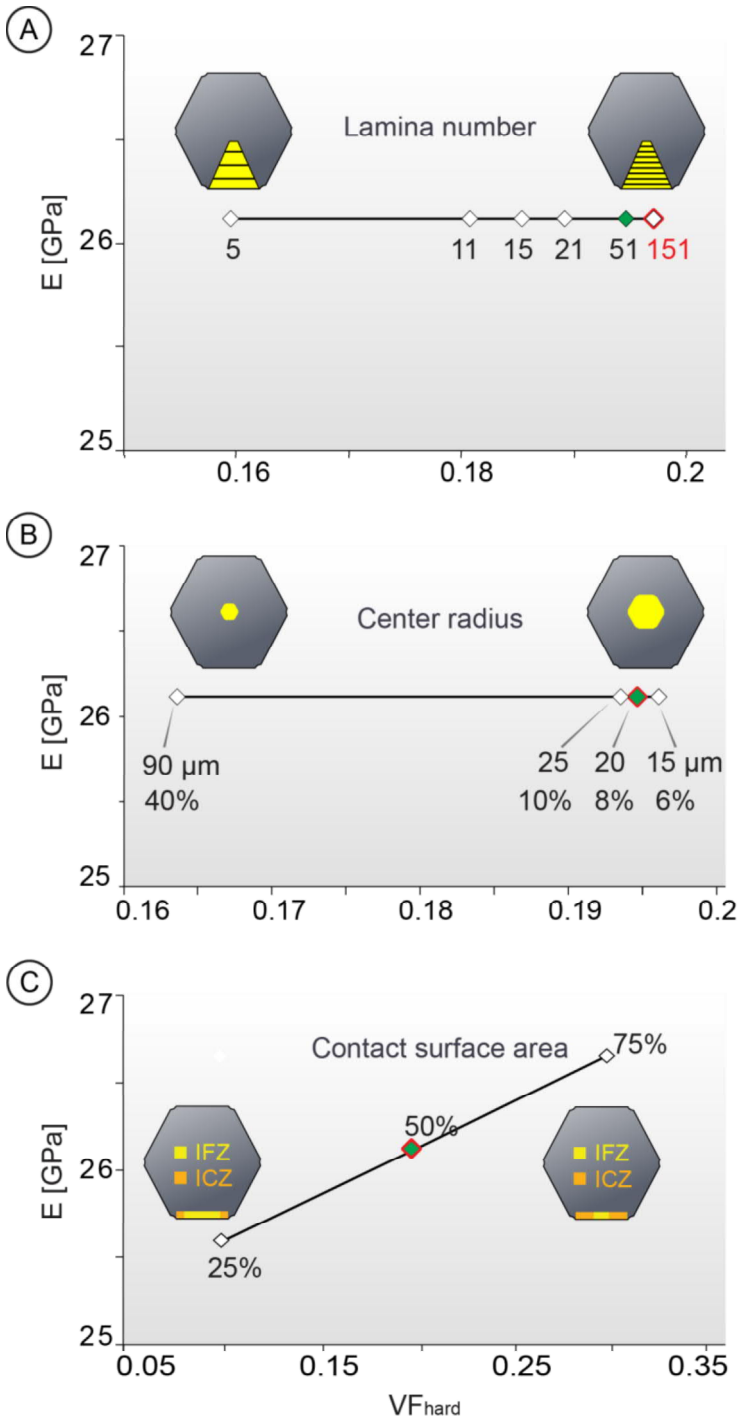

Figure 23: Effect of ultrastructure on tesserae mechanics.

Effect of varied ultrastructure (lamina number, center radius and contact surface area) on the volume fraction of hard material relative to tesserae volume (VF_{hard} : x-axis) and effective modulus (E: y-axis) A) The lamina number varied from 5-151 laminae. B) The radius of the center varied from 90µm to 15µm. C) The contact surface area varied from 25%-75% of the joint surface. Note that the modeled ultrastructural changes had little effect on the net effective stiffness of the tessera, except in the latter model, where stiffness increased by 6%. Green-filled points indicate the 'Base model' and red-outlined points represent the 'Bio-model'.

Similarly, decreasing the center radius size from 40% to 6% of tesserae width had little effect on VF_{hard}, which only increased from ~16% to 19% (Fig. 23B). Although the decrease in center radius increases the radial length of the spokes (which are bound in our model to the vertices of the center region), there is little change in the volume of hard material with respect to whole tesserae volume, and therefore negligible effect on tesserae stiffness.

In contrast, change in the contact zone area had a considerable effect on VF_{hard} and, as a result, also the effective stiffness of the tessera (Fig. 23C). The increase in the contact zone area (from 25% to 75%) resulted in VF_{hard} increasing by 20% (0.09 to 0.29). This is also linked to the design constraints of the model, where joint surfaces of tesserae are comprised of reciprocal combinations of fibrous and contact zone areas (Figs. 20, 21). As a result, an increase in a tessera's contact zone area concomitantly decreases the area of its fibrous zone. In our simulation, the increase of the contact zone area led to an increased volume of the higher mineral density spoke region (flanking the contact zone), and consequently reduced the volume of the lower mineral density intraspoke region (flanking the fibrous zone). Therefore, the overall volume of hard laminae was increased in the tessera model, resulting in an increase in the effective stiffness of the tessera by 6% (from 25.1 to 26.6 GPa).

Our modeled ultrastructural variations suggest that structural changes that result in increases in the proportion of spokes (i.e. increases in the proportion of hard material) in tesserae have the largest effect on tesseral stiffness. As such, the differences in the proportional thickness of spoke laminae and the size of the center region occurring across species and ages (Seidel et al., 2016b) are predicted to have little effect on whole tesseral stiffness. In contrast, alterations that result in changes to the contact zone area should have a pronounced effect on tesseral mechanics. Indeed, Seidel et al.'s (Seidel et al., 2016b) microCT and backscatter SEM survey of several elasmobranch species' tesserae implies that the proportion of high mineral density material does vary by species (Fig. 22), suggesting that changes in spoke volume and contact surface area may be a pathway by which local stiffness is tuned in the tessellated cartilage skeleton.

4.9.2 Mechanics of the bio-relevant model and its ultrastructure

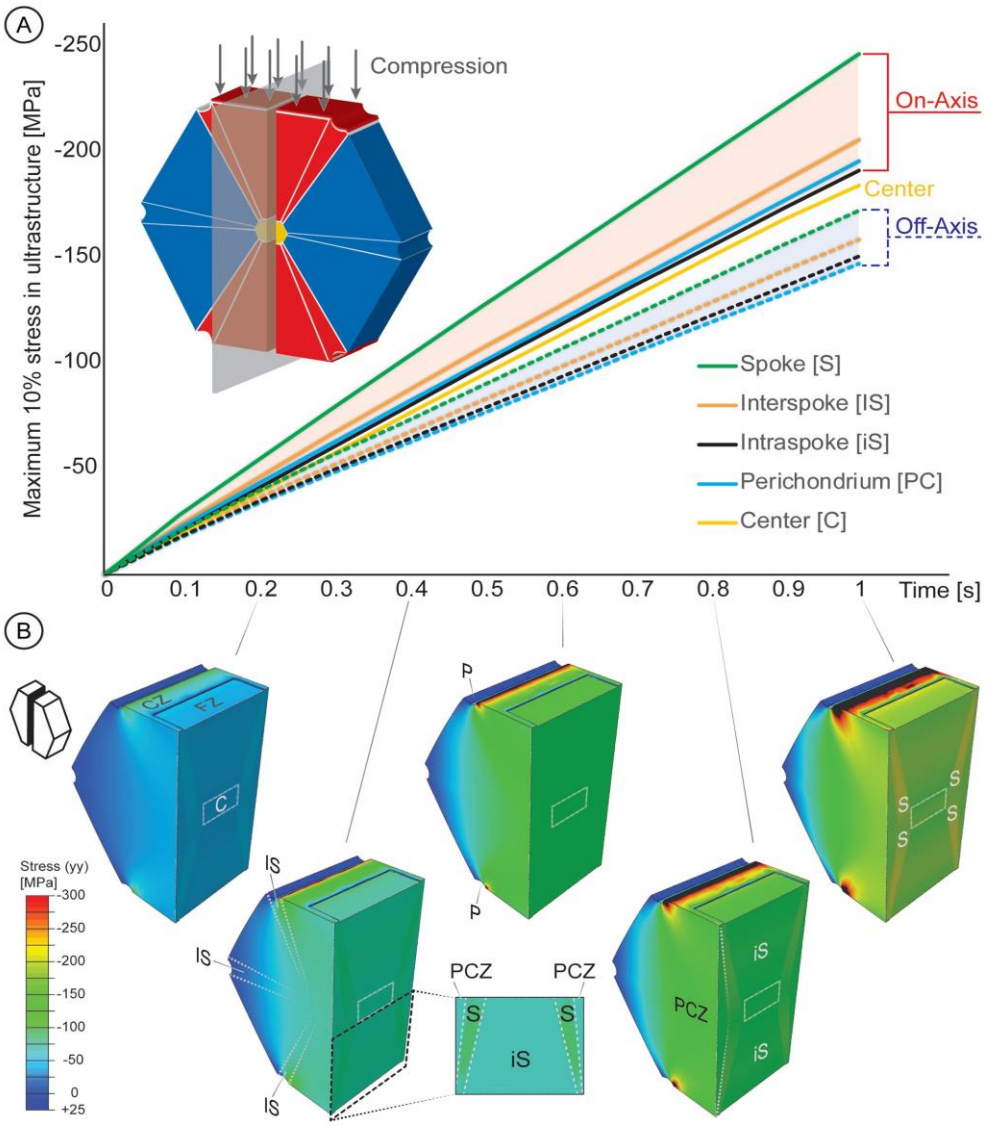

Figure 24: Stress contours in tesseral ultrastructure.

Stress in the loading direction in the local model. A) Plot of maximum 10% stress for each ultrastructural component in the loading direction (Syy) with respect to time. The spokes experience maximum stress while transferring the stresses across the tessera through the center. B) Vertical cross-section of the tessera showing the stress contours of stress (Syy) in the loading direction. Ultrastructural features are indicated by lines and abbreviations (see Fig. 19). Note that maximum stresses occur in the on-axis spoke and interspoke regions, radiating from the contact zone (CZ) across the tessera through the center (C).

Individual tesseral ultrastructures exhibit distinct mechanical behaviors and their mechanical behaviors vary according to their relationship to the axis of loading. This is visible in plots (Fig. 24A) and FEA models (Fig. 24B) showing on-axis stress in the bio-model as a function of time, and particularly when structures are divided into those

directly in line with load and those not (Fig. 24A). When load is applied to the contact surface of the tessera, stress builds up in the on-axis spokes (i.e. those flanking the loaded contact surfaces) and adjacent interspoke regions and radiates towards the center of the tessera (Fig. 24B). Reaching the end of a loading cycle, these stresses also radiate laterally outward from the center to some degree to the off-axis regions.

Our models suggest that the ultrastructural features in line with load —and particularly spokes— will experience maximum stresses, while also acting as channels, ferrying mechanical stimulation to the tesseral center. As a result, the center has the highest strain energy density when compared to other ultrastructural features (from time 0.2s in Fig. 24). This is an important observation, considering that whereas spokes are acellular, the center is filled with cells, housed in lacunar spaces and connected by short canalicular passages (Figs. 19E-F, 25) (Dean et al., 2010; Seidel et al., 2017a; Seidel et al., 2016b). As mammalian chondrocytes have been shown capable of sensing mechanical signals (Chen et al., 2013; Lammi, 2004; Wann et al., 2012; Wu and Chen, 2000), we hypothesize that the cells in the center region of tesserae may act sensors, collecting mechanical loading information within tessera. This particular role may explain the spherical appearance of chondrocytes in the center of tesserae, distinguishing them from the more ubiquitous, flattened spheroidal chondrocytes elsewhere and suggests a division of labor among the different shaped cells throughout tessellated cartilage (i.e. in unmineralized cartilage, joints and tesserae) (Dean et al., 2009a; Dean et al., 2010; Seidel et al., 2016b). Additionally, it should be noted that the stresses in non-spoke/non-center regions (interspoke, intraspoke, perichondral and chondral regions) are comparatively low during loading, suggesting that by ferrying stresses through the acellular spokes to the center region, spokes may protect cells in non-spoke/non-center regions (e.g. interspokes; Fig. 25).

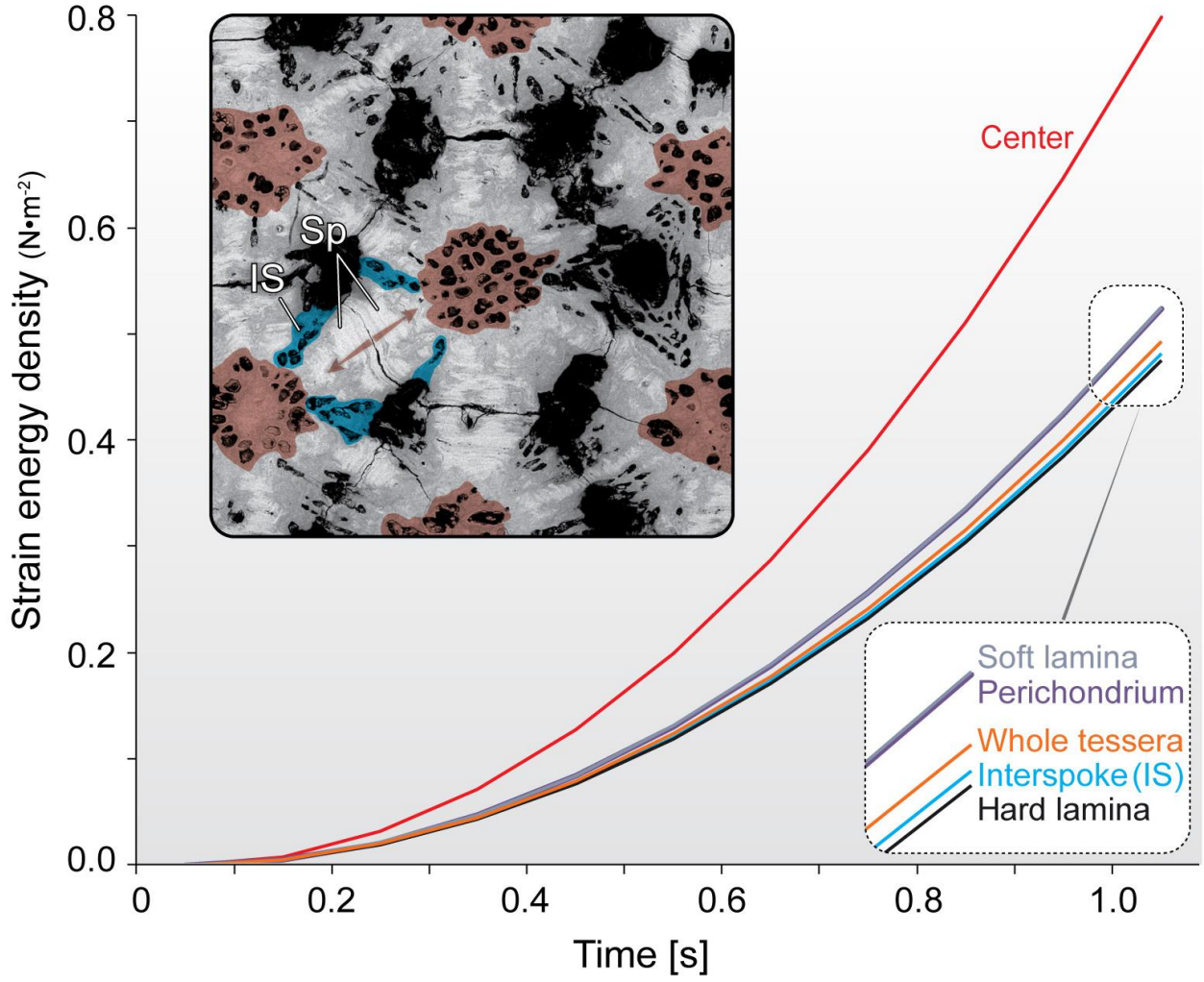

Figure 25: Strain energy density in tesseral ultrastructure.

Strain energy density in tesseral ultrastructural components with respect to loading time. The center experiences maximum strain energy density compared to other ultrastructures. As shown in the inset backscatter electron microscopy image, the center is filled with cells (shaded red), which may act as mechanosensors for stresses (indicated by red arrows) ferried through spokes (Sp). The interspoke (IS) region (colored blue) is also cell-rich, but is off-axis from predicted intertesseral stresses.

We provide support for this hypothesis through an altered version of our CAD model, which simulated a tessera where non-spoke/non-center regions were assigned negligible mechanical properties, simulating a tessera lacking these regions. The resultant model exhibited nearly the same effective modulus as the complete bio-model (data for non-center tesserae are shown in Appendix A.9), arguing that non-spoke/non-center regions may perform a non-mechanical role, perhaps acting as repositories for cells for tissue growth. This also explains the geometries of the recently described stellate (asterisk-shaped) 'trabecular tesserae' (Atake et al., 2019) (Fig. 26). Published

images from a variety of species (Atake et al., 2019; Knötel et al., 2017; Leydig, 1857; Seidel et al., 2016b) indicate that the stellate morphology of these tesserae is due to a reduction or lack of interspoke regions (Fig. 26B-C). The stellate morphology may represent tesserae stripped down to their mechanical necessities (i.e. just their spoke and center regions); the reason for this 'reduced' morphology requires investigation.

In addition to the stresses observed in spokes, notably high stresses are also visible at the corners of the contact surfaces, adjacent to tesseral pores (Fig. 24B). We verified that these are largely artifacts of the sharp corners bordering pores in our models, by comparing the bio-model with a similar CAD model lacking pores, with such stress concentrations being considerably reduced in the latter model (data not shown). It should be noted, however, that tesseral pores are natural features (see Fig. 19E) (Maisey, 2013a; Roth, 1911; Seidel et al., 2016b) and that holes, edges and corners are common stress concentrators in tissues (Petrie and Williams, 2005). Therefore, it is possible that tesseral pores create a unique stress environment in tessellated cartilage that is perhaps stimulating for tissue growth.

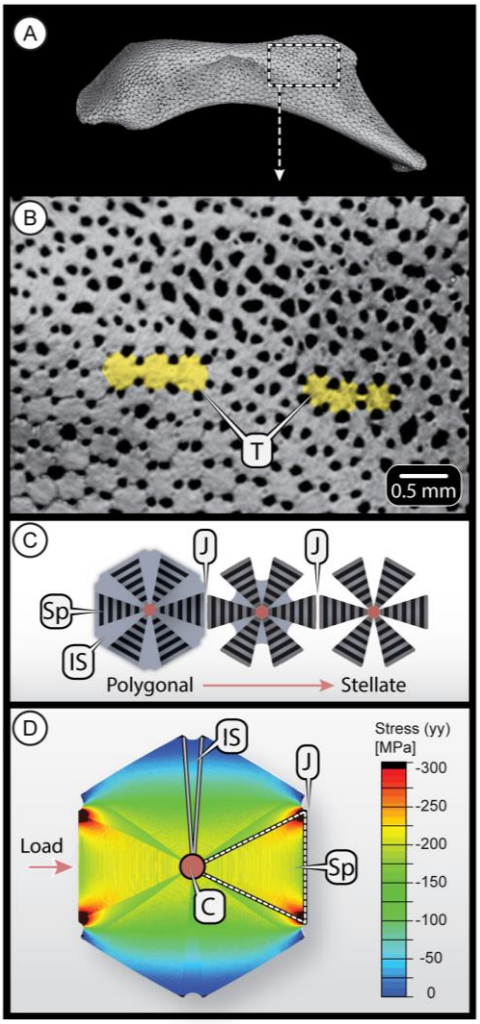

Figure 26: Trabecular tesserae.

A) MicroCT of the hyomandibula from Fig. 19B and B) a zoomed in region, showing a gradient in tesseral shape with two sets of three exemplar tesserae (T) marked in yellow: more typical polygonal tesserae on the left and stellate 'trabecular' tesserae on the right. C) Schematic of the structural differences between polygonal and stellate tesserae, showing the reduction of the interspoke region (IS) and the predominance of spokes (Sp) in stellate tesserae. Note that joints (J) are located approximately midway between the centers (C) of adjacent tesserae in the microCT image in B, although they are not always visible. D) Maximum stress in a finite element simulation, illustrating stresses passing predominantly through on-axis spokes. This renders interspoke regions largely mechanically redundant, perhaps explaining the observed morphology of stellate tesserae. Abbreviations as in Fig. 19.

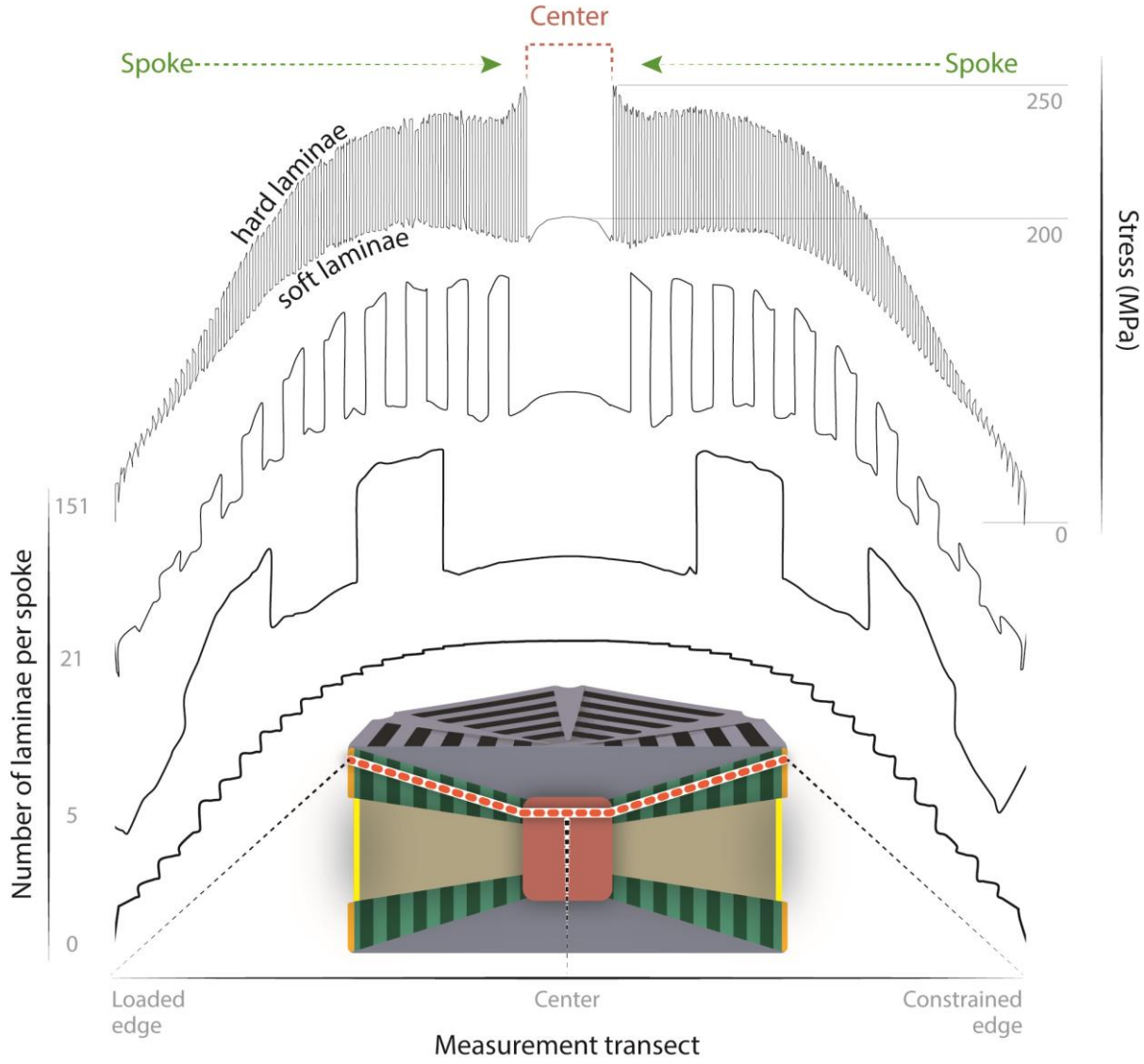

Figure 27: Comparison of stresses across tesserae with varied lamina number.

Comparison of stresses through a measurement transect —from the loaded edge to the constrained edge, through the on-axis spokes and center— for models with increasing spoke lamina number (from bottom to top: 0, 5, 21, 151 laminae). The shape of the graphs is more telling than the absolute values, but the stress y-axis at the top right applies to all models: the absolute minimum is zero MPa, the stress in the center is approximately 200 MPa and the absolute maximum is 250 MPa. Note that with increase in lamina number, the stress oscillation wavelength decreases, suggesting thinner laminae may protect tesserae by causing crack to follow more circuitous paths when damage evolves. The measurement transect is illustrated by the red dashed line on the cross-sectioned tessera schematic at the bottom of the figure.

The mechanical importance of on-axis spokes and their structure is also evident from stress traces plotted along measurement transects running through the tessera along the loading axis, from the loaded tesseral edge to the constrained edge (Fig. 27). Comparing models with 0, 5, 21 and 151 laminae per spoke, the stress behavior was

always similar in contralateral spokes (left and right sides of the graph) under the applied loading conditions, and therefore, all stress line maps were symmetrical around the center. Whereas in the homogeneous model (i.e. no laminae model) stress increased smoothly from the intertesseral contact zone along the spoke to the center, in heterogeneous models (i.e. models with laminated spokes), stress oscillated according to the periodicity of spoke laminations, with local maxima in high mineral density laminae (HMDL), local minima in low mineral density laminae (LMDL), and frequency increasing as the number of laminae increased. This indicates a potential protective advantage in having tesseral spoke laminae be very thin. Since spokes are the highest modulus features in tesserae (Seidel et al., 2019c) and are associated with contact zones (Seidel et al., 2016b), they will regularly experience high stresses, increasing their chance of material failure relative to adjacent, richly cellular ultrastructures. The high frequency of stress oscillations predicted for the biological model (151 laminae, Fig. 27), however, indicate that the laminar structure of spokes may function to contain any damage resulting from a load. Periodic material inhomogeneities (i.e. oscillating local variation in tissue structure and/or modulus) are common strategies in biological materials for reducing the driving force of cracks forming in tissue (Fratzl et al., 2007b; Fratzl et al., 2016b). These function to dissipate the energy of fracture, often by deflecting growing cracks at points of a sudden change in material or structural properties (e.g. weak interfaces, modulus mismatches between tissue layers) (Fratzl et al., 2007b; Fratzl et al., 2016b; Kolednik et al., 2011). The fine lamellar structure (i.e. small wavelength of modulus variation) of tesseral spokes should increase the toughness of tesserae by increasing the predicted path length for forming cracks, and thereby the rate by which they are robbed of energy. This is supported by the zig-zagging cracks that can form in spokes during dehydration in sample preparation (see *Leucoraja* image in Fig. 22), indicating that forming radial cracks were periodically re-routed to run parallel to and not through laminae. The natural fracture behavior of tesserae, however, remains to be investigated, as does the ultrastructure of spoke laminae (in particular in 3d), which may involve additional structural means of controlling fracture energy (e.g. via the architecture of underlying fibrous material).

4.9.3 Global behavior of tesserae

Our global model indicates that the tesseral network could also respond flexibly to different loading scenarios at larger size scales. The stress-strain curves are plotted for tension and compression regimes of the tesseral mat in Fig. 28. In tension, the joint material accommodates stress as the tesserae are pulled apart from one another (Fig. 28A). In compression, there are two phases in the material behaviour. Before tesserae coming into contact, they behave like rigid bodies squeezing the soft fibrous joints, which take all the load and undergo large deformations. Once in contact, however, the tesserae induce sharply increased stresses in themselves (inset, Fig. 28B). This supports hypotheses that tesseral mats will exhibit a tension-compression asymmetry in loading, being softer in tension and stiffer in compression (Fratzl et al., 2016b; Liu et al., 2010b; Liu et al., 2014b). In addition, our structural variations on the base model show that increasing the size of tesseral joints delays tesseral collision to higher strains (i.e. note the shift of the curve's inflection point in Fig. 28B). Altering tesseral material properties changes the slope of the post-inflection curve (compare the 25 and 35 GPa models in Fig. 28B).

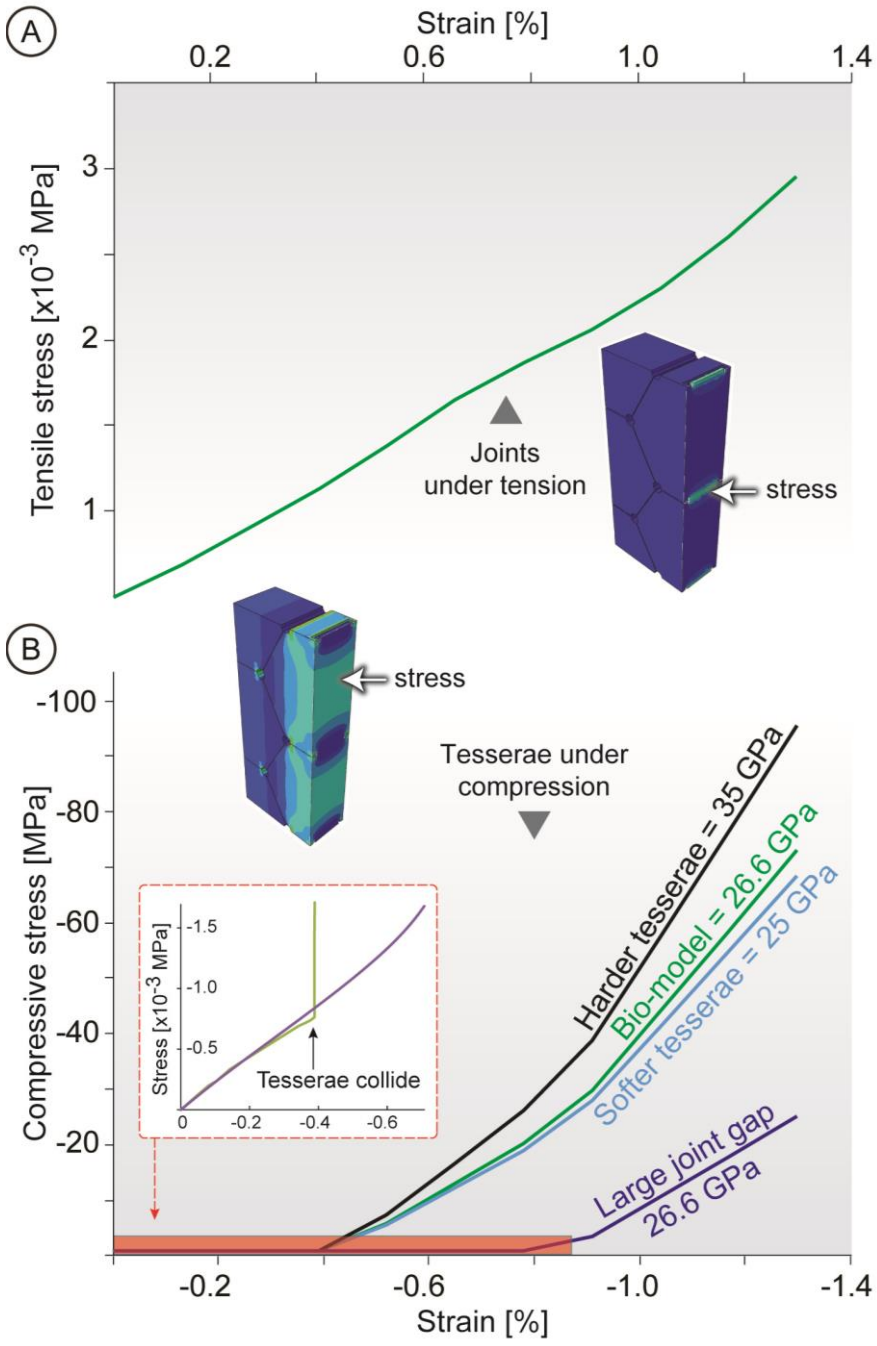

Figure 28: Tensile and compressive stress vs. strain curves for a tessellated mat (global model).
The biphasic properties of the mat —hard tiles and soft joints— result in strikingly different tensile and compressive behaviors. A) In tension, the tesserae are pulled apart and the joint material takes all the load. B) In contrast, in compression, the joint bears all the load until tesserae come into contact, inducing dramatically rising stresses. To demonstrate the tunability of the tesseral mat, three additional models are shown: with stiffer tesserae (35 GPa), with less stiff tesserae (25 GPa), and with joints 2x wider than in the base model. Note that changes in tesseral stiffness cause changes in the slope of the stress-strain curve after the tesserae-collision inflection point, whereas changes in the width of tesseral joints shifts the position of the inflection point along the x-axis.

4.10 Conclusions

The parametric models designed here illustrate that the effective stiffness of the tesserae and the tesseral mat can be tuned at multiple size scales via changes to structural and/or material properties, allowing variable response to different loading conditions. At the size scale of the tessera (i.e. the local model), ultrastructural changes that cause an increase in the volume of spokes in a tessera stiffen the tessera. Since spokes and contact zones seem to be linked (Seidel et al., 2016b), this could suggest that the deposition of spoke laminae (and the concomitant effect on tesseral stiffness) is a direct response to a tessera's loading environment. Tesseral structure being shaped by the loading environment is also suggested by the predicted stress-leading of spokes and the existence of stellate tesserae, where extraneous (non-load-bearing) regions are absent. Our global model suggests further tuning capability at the scale of the tesseral array, where the geometry (e.g. the distance between tesserae) and material properties (tesseral effective modulus) can control tessellation-level properties. This indicates that the species-level and anatomically local variations observed in tesseral shape and ultrastructure (Atake et al., 2019; Maisey, 2013a; Seidel et al., 2016b) may have important mechanical implications, properties that could be translated into guidelines for the bio-inspired design of tessellated materials.

5. Evolution of tessera models

The modeling and optimization of the tesserae model required several iterations of design and subjecting of the model to finite element analysis. Finite element analysis results were used to improve the design features in the tesserae CAD model, as they allowed visualization of abnormal stress contours. All models were constructed in the parametric CAD software Rhinoceros 3D Version 5 (Robert McNeel & Associates, Barcelona, Spain), coupled with Grasshopper 3D (0.9.0076), a plug-in for creating algorithms which allows parametric modelling of tesserae ultrastructure. The first version of the tessera CAD model acted as a prototype to observe and formulate further design rules for tesserae design. A simple two-dimensional sketch of tesserae (horizontal cross-section) was developed, all ultrastructural features were extruded according to their dimensional height, and joint material was filled in the gap between two tesserae. It was observed that due to the design process of this first model in Rhino-Grasshopper, all the ultrastructural features that shared borders were linked to one other. In a sense, when the size of the center was decreased, the length of the spoke was also increased or when the size of the pore has increased the width of the spoke was decreased. This meant that ultrastructural features could not be changed independently of one another, a necessary feature for testing the functional role of individual variables. Additionally, in FEA, the tessera version 1 model exhibited high-stress concentrations at the edges of pores and lamina steps. In this model, the laminated structure of spokes was mimicked by stacking rectangular laminae that decreased in dimension from center to margin. This, however, resulted in the spoke having a jagged stepwise margin, where stress was concentrated in the model (Fig. 29). These artificial high-stress concentrations at the edges of spokes and pores were overcome by altering the design in version 2.

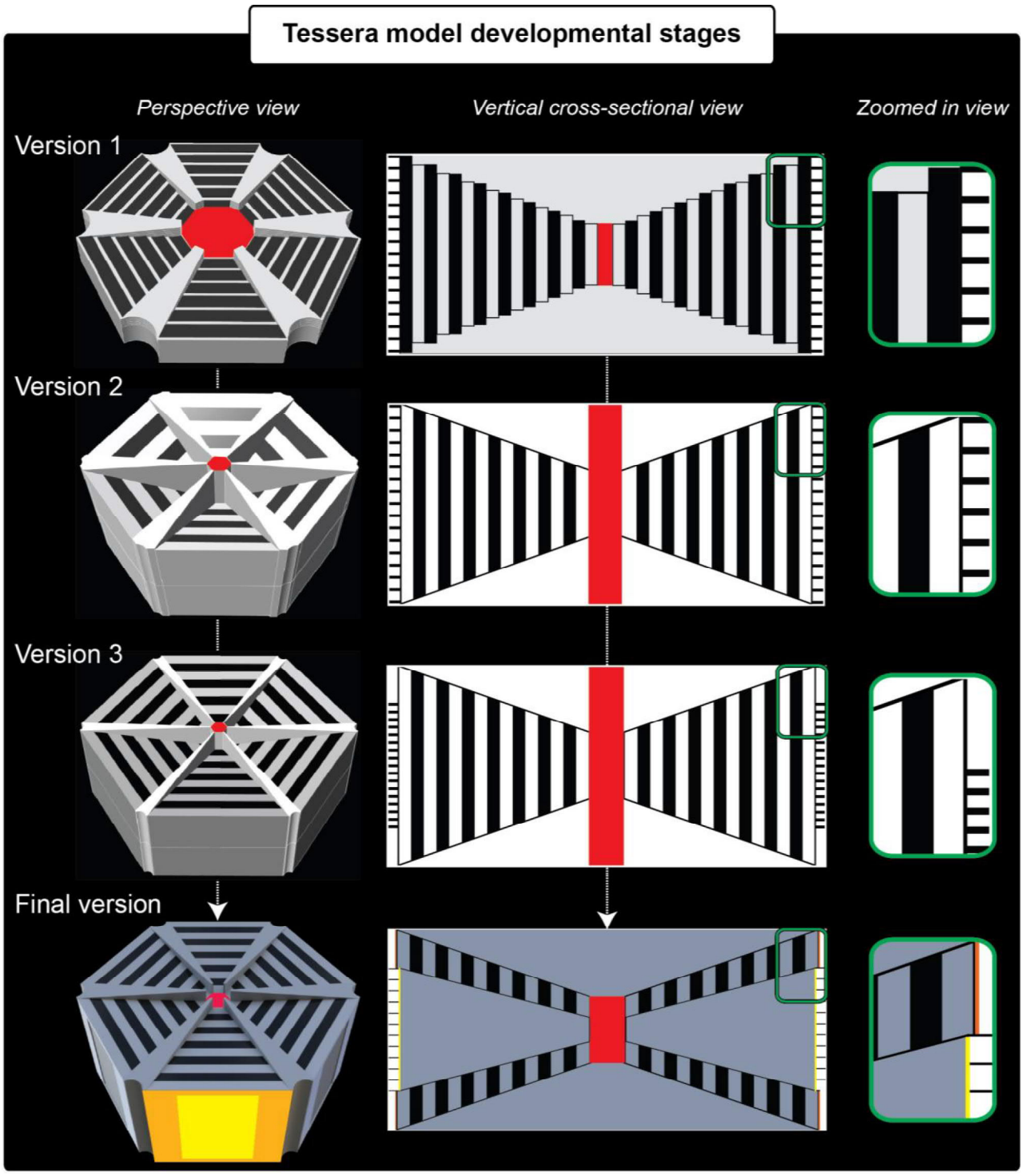

Figure 29: Evolution of tessera models used in this dissertation presented in perspective and vertical cross-sectional views.

The perichondral and chondral regions were removed to show the ultrastructural alterations within the tesserae model. In version 1, laminae in spokes are in steps (creating jagged margins) and the spokes are attached to the pores (meaning the two could not be altered independently). These features created high-stress concentrations, and were eliminated. In version 2 the spokes were constructed as a smooth ramp, and the spoke edge was moved away from the pores to prevent the spokes from experiencing high stress

artifactually. The joint material in version 1 and 2 was included in the gap between the two tesserae and this lead to convergence error in FEA as the joint was constrained from expanding in compression. The center region (red) was merged with the perichondral and chondral regions to facilitate model assembly; in the end, this limited the ability to vary center morphology independently, and was abandoned in the final version. In version 3, the joint height was shortened to better match the localization of joint material in the biological system. This again led to convergence error, as joints were restricted in expansion in the plane normal to loading as they were squeezed between tesserae. The final tessera model incorporated all the rectifications and captured all the morphological information from biological data, introducing a recessed joint attachment surface, inspired by the biology and avoiding the joint material compression convergence issue.

In the second version of the tessera CAD model, ultrastructural components were disconnected from each other such that altering one dimension of an ultrastructure did not affect the dimensions of others. Additionally, the steps in the laminae were converted into a smooth ramp such that high-stress concentrations were removed from spoke margins. The edges of the spokes width were moved away from the pores to better reflect the biological condition and to protect the spoke from high stresses occuring at the pores. Since the spokes were expected from biological data to be regions which experience high stress due to channeling of loads (Seidel et al., 2016a), it was essential to reduce all artificial (i.e. design-linked) sources of stress, in order to make aspects of the natural load response more evident. Since the perichondral, chondral and center regions are assigned with the same material, the center was extruded the same height as the tessera to facilitate the modeling process. This, however, resulted in later issues regarding the ability to independently alter center morphology, and this design aspect was abandoned in the final model (Fig. 29) On subjecting the version 2 tesserae model to simulated load in FEA software, the FEA solver was not able to converge to an optimal solution. This was predominantly due to the structural design of the joint material: the joint material was modeled to be very soft in compression and, as there was no space into which the joint material could expand, when the compression load was applied on the tesserae it was squeezed between the flat edges of the tesserae, resulting in convergence errors. To facilitate accurate structural behavior in the FEA software, the joint structure was redesigned in version 3.

In the third version of the tessera CAD model, the vertical height of the joint was decreased, to allow a sufficient gap for the joint material to expand under compression,

but also to account for the more localized arrangment of joint material in the biological system. This design, however, again led to a convergence error in the FEA software, due to the joint material not having space to expand once tesserae edges collide in compressive loading.

To address the design complications recorded for version 3, I returned for further analysis of the morphological data (Seidel et al., 2016a), where several consistent anatomical features were observed that were pertinent to the design of the final CAD model. First, it was observed that, in addition to the lower mineral density "interspoke" regions bewteen adjacent spokes, lower mineral density regions also exist within the spokes, swaths of uniform (non-lamellated) tissue running through the center of spokes. Second, these "interspoke" regions extend to the joint edge of tesserae, where they connect to the surface where joint material attaches (the intertesseral fibrous zone, IFZ). Third, the IFZ zone is recessed relative to the surface wheere tesserae come into physical contact (the intertesseral contact zone, ICZ). Incorporating these features into the final version of the tessera model addressed the convergence issues observed in version 3. The intraspoke region was created by making a pyramidical cavity within the spokes. A recessed, rectangular cavity was made on the face of the intraspoke region to attach the joint material (IFZ: yellow zone in Fig. 29), which ensured a sufficient gap for the joint material to expand. The face of the most distal spoke lamina then acted as a contact zone of the tesserae (ICZ: orange zone in Fig. 29), the dimensions of which could be altered dimensionally. On subjecting the final version tesserae model to FEA, it was observed that the stress concentrations were optimized when compared to previous models and convergence errors were eliminated. The final version of tesserae incorporates all appropriate morphological information from the biological model, and the structural features can be varied parametrically and largely independently for testing in FEA.

Summary

This dissertation “Structural modeling and computational mechanics of stingray tesserae and bio-inspired tessellation” provides detailed biological hypotheses and mechanical insights into the tessellated shark and stingray cartilage and its ultrastructure, while also offering perspectives on principles of tessellation design and the challenges of modeling complex biological tissues. Previous studies of tessellated cartilage focused largely on entirely on whole skeletal elements, largely ignoring the ultrastructural information present in them (Seidel et al., 2016a). Tesserae are, however, the fundamental structural subunit of shark and ray skeletons and therefore a detailed perspective on their contribution to the tissue is vital to an understanding of skeletal mechanics and growth.

The principal objective of this dissertation was to characterize the mechanical properties of tesseral structural and ultrastructural features and evaluate their mechanical performance in order to understand their contribution to the mechanics of the tessellated shark cartilage. Tesserae are visible in the skeletons of stem Chondrichthyes in the fossil record for millions of years (Long et al., 2015; Maisey, 2013b), yet their functional importance has remained unknown. The results from the two phases of this dissertation project provide unique insights into the functional role of these ancient structures in the performance of shark and ray skeletons.

In phase 1 of the dissertation, two-dimensional analytical models (triangle, square and hexagon) of tiles surrounded with soft joints allowed investigation of the effects of structural parameters (joint thickness, tile shape, joint/tile Young’s modulus) on the effective modulus of the tiled composite. These iterative models showed that by decreasing joint thickness and maximizing the difference in joint and tile modulus, the effective modulus of the tiled composite could be maximized. In this way, the structural and material ratios of the tile to joint can be used to optimize the overall stiffness of the skeletal element. The modulus could be further tuned by adjustments in tile shape. Among all the shapes, square tessellations were least sensitive to the changes in the structural parameters, whereas hexagons were the most sensitive. These results provide useful estimates of tensile and compressive properties of 2-dimensional tiled composites under uniaxial loading. These results paved groundwork for the more

complex three-dimensional models of phase 2, which incorporated complex ultrastructural features within them.

Phase 2 of this dissertation used parametric modeling and FEA approaches to vary the ultrastructural parameters of tesserae to evaluate the effect of ultrastructure on tesserae stiffness and stress distribution in loading. By incorporating biologically-relevant structural variables, from finite element analysis results. The stress contours generated by finite element analysis illustrated the importance of spokes in tesseral mechanics, through their consolidation and leading of maximum stress and, through their lamellated structure, the prevention of crack propagation. FEA results also demonstrated that the center likely experiences high strain energy density, an indicator that the center may play an essential role in sensing loading conditions within tesserae. Additionally, through generation of the first model of the global behavior of the tesseral mat, it was demonstrated that skeletal mechanics can also be controlled through 'meso-scale' structural/material changes (e.g. in joint thickness, whole tile modulus). For example, increasing the gap between the tesserae delays their coming into contact during compression, resulting in a larger soft "toe" region in the composite's stress-strain curve. The results from phase 2 improve the understanding of the contribution of tesserae —at multiple size scales— to mechanics, growth and load management and help us build hypotheses regarding the same.

The combined results of phase 1 and phase 2 of this dissertation provide insight into fine-scale details in the structural mechanics of tesserae, which was not provided by the previous studies. The results show that the tessellated cartilage is both flexible and stiff according to the specific loading regimes and the contribution of the ultrastructure is protecting the cartilage from damage. The engineering results of the tesseral ultrastructure mechanics combined with their morphological information will help us in building guidelines for engineering tiled composites with suitable materials according to the required function.

Appendix

We apply modified Rule of Mixtures models to tessellations constructed from arrays of triangular, square and hexagonal tiles, by dividing each composite unit cell (the tile and its surrounding joint material) into simple geometric shapes containing tile and joint material. The justifications for these models are discussed in the Methods; we describe and illustrate the partitioning of each unit cell shape below.

1. Triangle

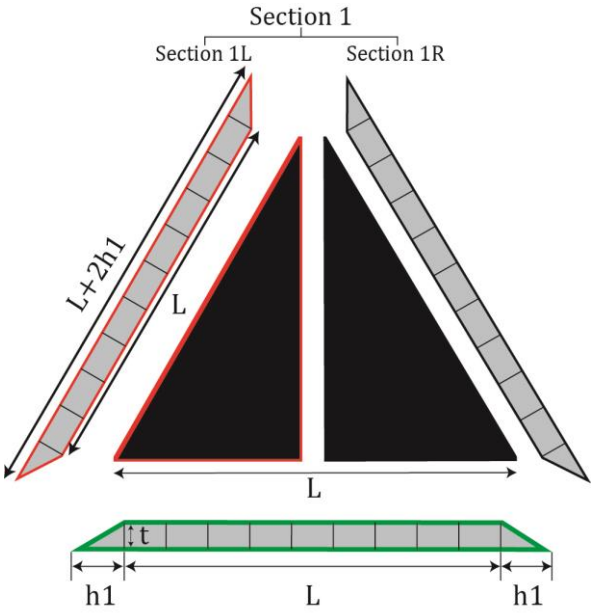

Figure A.1: Dimensions and partitions of triangle composite

a. Dimensions and areas of the triangle composite

Length of the tile = L

Thickness of the joint = t

Length of the composite = L+2*h1

$h1 = \frac{t}{\tan 30°}$

Area of the composite = $\frac{\sqrt{3}}{4}*(L+2h1)^2$

Area of the tile = $\frac{\sqrt{3}}{4}*(L)^2$

Orientation of the fiber material relative to load = θ

b. Triangle partitions

Section 1 is marked with red lines whereas Section 2 is marked with a green line. Section 1L and Section 1R are mirror images of each other, therefore it is enough to solve the effective modulus of just Section 1L, which will have the same effective modulus as Section 1R and as the complete Section 1 (combination of Section 1L and Section 1R).

c. Effective modulus of Section 1L ($E_{section1L}$)

Area of tile region in Section 1L = $\frac{1}{2}*\frac{\sqrt{3}}{4}*(L)^2$

Joint region in the Section 1L is trapezoid.

Area of joint region marked in red in Section 1L = $\frac{(L+L+2*h1)}{2}*t$

Total Area of Section 1L = TA_1

$$TA_1 = \frac{1}{2}*\frac{\sqrt{3}}{4}*(L)^2 + \frac{(L+L+2*h1)}{2}*t$$

Area fraction of tile region in Section 1L = AF_1

$$AF_{section1L} = \frac{\frac{1}{2}*\frac{\sqrt{3}}{4}*(L)^2}{\frac{1}{2}*\frac{\sqrt{3}}{4}*(L)^2 + \frac{(L+L+2*h1)}{2}*t}$$

$$E_{section1L}=\cos^2\theta * \frac{E1 * E2^{0°}}{E1*(1-AF_{section1L}) + E2^{0°}*(AF_{section1L})} + \sin^2\theta * (E1*AF_{section1L} + E2^{90°}*(1-AF_{section1L}))$$

d. Effective modulus of the triangle composite ($E_{composite}$)

Total area of composite = $TA_{composite}$

$$TA_{composite} = \frac{\sqrt{3}}{4} * [\, L + 2\left(\frac{t}{\tan 30°}\right) \,]^2$$

Total area of Section 1 (L and R combined) = $\frac{\sqrt{3}}{4} * (L)^2 + 2 * (\frac{(L+L+2*h1)}{2} * t)$

Area fraction of the composite= $AF = \frac{\text{Total area of Section 1 and 2}}{TA_{composite}}$

$$AF = \frac{\frac{\sqrt{3}}{4} * (L)^2 + 2 * (\frac{(L + L + 2*h1)}{2} * t)}{\frac{\sqrt{3}}{4} * [\, L + 2\left(\frac{t}{\tan 30°}\right) \,]^2}$$

$$E_{composite} = \frac{E_{section1} * E2^{0°}}{E_{section1} * (1\text{-}AF) + E2^{0°} * (AF)}$$

2. Square

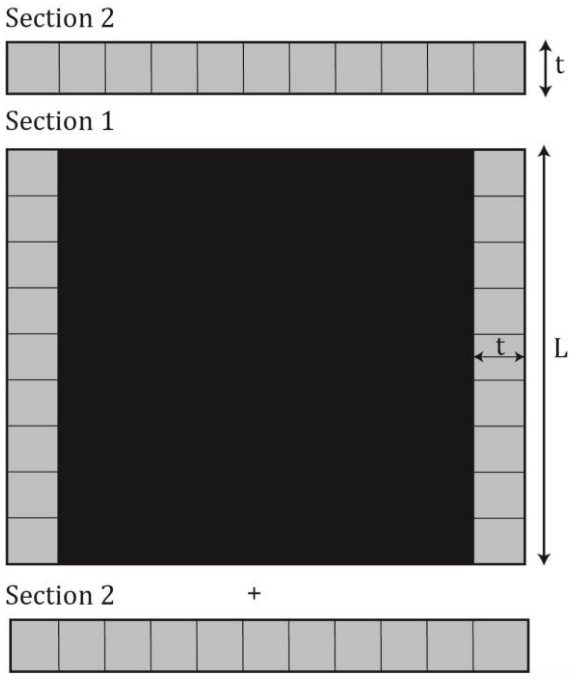

Figure A.2: Dimensions and partitions of square composite

a. Dimensions and areas of the square composite

Length of the tile = L

Joint thickness = t

Length of the composite = L+2*t

Area of the composite $=(L+2*t)^2$

Area of the tile = $(L)^2$

b. Effective modulus for Section 1

Area of Section 1 =(L+2*t)*L

Area fraction of the Section 1 (AF_1) = $\frac{\text{Area of the tile}}{\text{Area of composite}}$

$$AF_{section1} = \frac{L^2}{L*(L+2*t)}$$

Effective modulus of Section 1= $E_{section1}$

$$E_{section1} = E_1 * AF_1 + E2^{90°} * (1 - AF_1)$$

c. Effective modulus of the square composite

$$\text{Area fraction (AF)} = \frac{\text{Total area of Section 1}}{\text{Total area of composite}} = \frac{L*(L+2*t)}{(L+2*t)^2} = \frac{L}{L + 2 * t}$$

Since Section 1 and Section 2 are in series and since both Section 2 elements (top and bottom joints) are composed only of joint material at 0° orientation, the net effective modulus of the square composite is:

$$E_{composite} = \frac{E_{section1} * E2^{0°}}{E_{section1} * (1-AF) + E2^{0°} * (AF)}$$

3. Hexagon

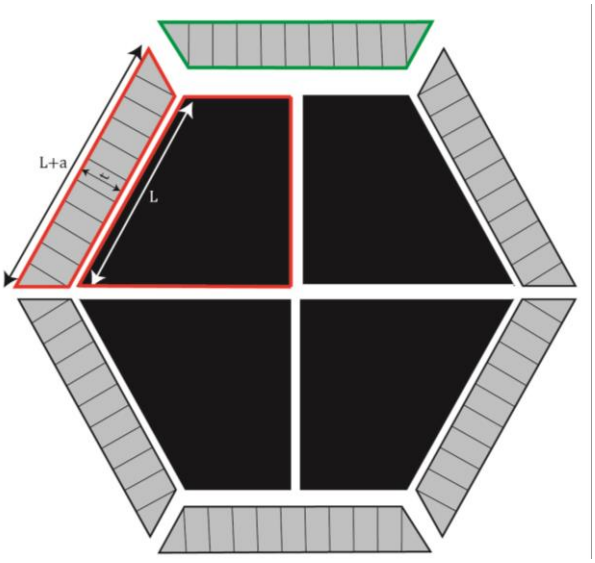

Figure A.3: Dimensions and partitions of hexagonal composite

a. Dimensions and areas of the hexagon composite

Length of the tile = L

Joint thickness = t

Length of the composite = L+a

$$a = \frac{t}{\sin 60°}$$

$$\text{Area of the composite} = \frac{3\sqrt{3}}{2} * (L+a)^2$$

$$\text{Area of tile} = \frac{3\sqrt{3}}{2} * (L)^2$$

θ = Orientation of the fiber material relative to load

b. Hexagon partitions

Section 1 is marked with red lines, whereas Section 2 is marked with a green line. Similar to triangle, Section 1 appears several times in the unit cell in mirrored, identical parts. It is enough to solve the effective modulus of the single Section 1 element shown

in Figure A.3, which equals the effective modulus of all three additional Section 1 elements.

c. Effective modulus of Section 1:

Area of the tile in Section 1 = $\frac{1}{4} * \frac{3\sqrt{3}}{2} * (L)^2$

Area of the joint in Section 1 = $\frac{(2*L+a)}{2} * t$

$$AF_{section1} = \frac{\text{(Area of tile in Section 1)}}{\text{Area of tile in Section 1 + Area of joint in Section 1}} = \frac{(\frac{1}{4} * \frac{3\sqrt{3}}{2} * (L)^2)}{(\frac{1}{4} * \frac{3\sqrt{3}}{2} * (L)^2 + \frac{(2*L+a)}{2} * t)}$$

The effective modulus of the Section 1 is calculated below:

$$E_{section1} = \cos^2\theta * \frac{E1 * E2^{0°}}{E1*(1-AF_{section1}) + E2^{0°} * (AF_{section1})} + \sin^2\theta * (E1*AF_{section1} + E2^{90°} * (1-AF_{section1}))$$

d. Area fraction of Section 2:

Area of the joint in Section 2 = $\frac{(2*L+a)}{2} * t$

Total area of all four Section 1 elements = $(\frac{3\sqrt{3}}{2} * (L)^2 + 4 * \frac{(L+L+a)}{2} * t)$

$$\text{Area fraction of the composite} = AF = \frac{\text{Total area of Section 1}}{\text{Total area of composite}} = \frac{(\frac{3\sqrt{3}}{2} * (L)^2 + 4 * \frac{(2*L+a)}{2} * t)}{\frac{3\sqrt{3}}{2} * (L+a)^2}$$

e. Effective modulus of the hexagon composite

$$E_{composite} = \frac{E_{section1} * E2^{0°}}{E_{section1} * (1-AF) + E2^{0°} * (AF)}$$

4. Alternative partition schemes:

The three unit cell types can be partitioned in several different ways. We present two schemes below, Schemes A and B, and compare their results in Figure A.5. We consider Scheme A to be the more intuitive and so use it to generate our datasets.

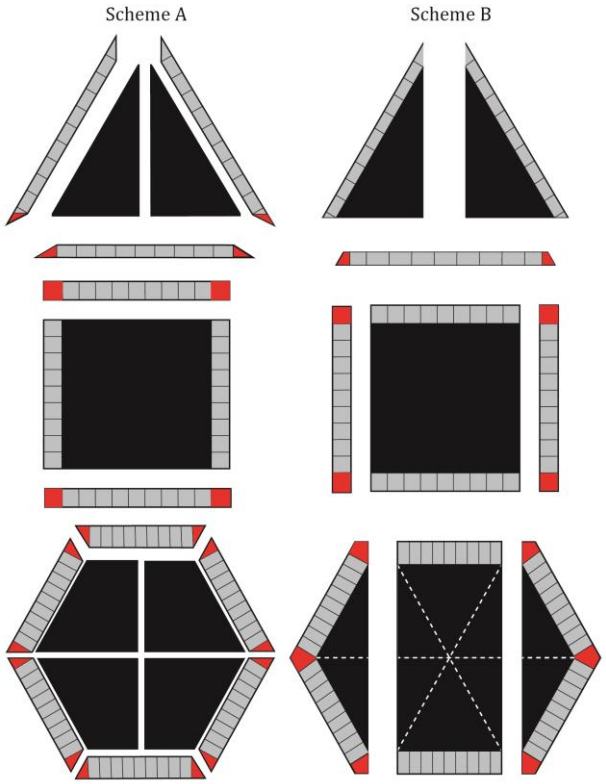

Figure A.4: Partioning schemes. Regions colored in red indicate corner joint elements that are partitioned differently in the two schemes. As a result, some joint elements switch from in-series to oblique elements; since our analytical model adjusts the joint element modulus (E2) according to fiber orientation, some of these elements also experience changes in joint modulus.

a. Comparison of results between partition schemes

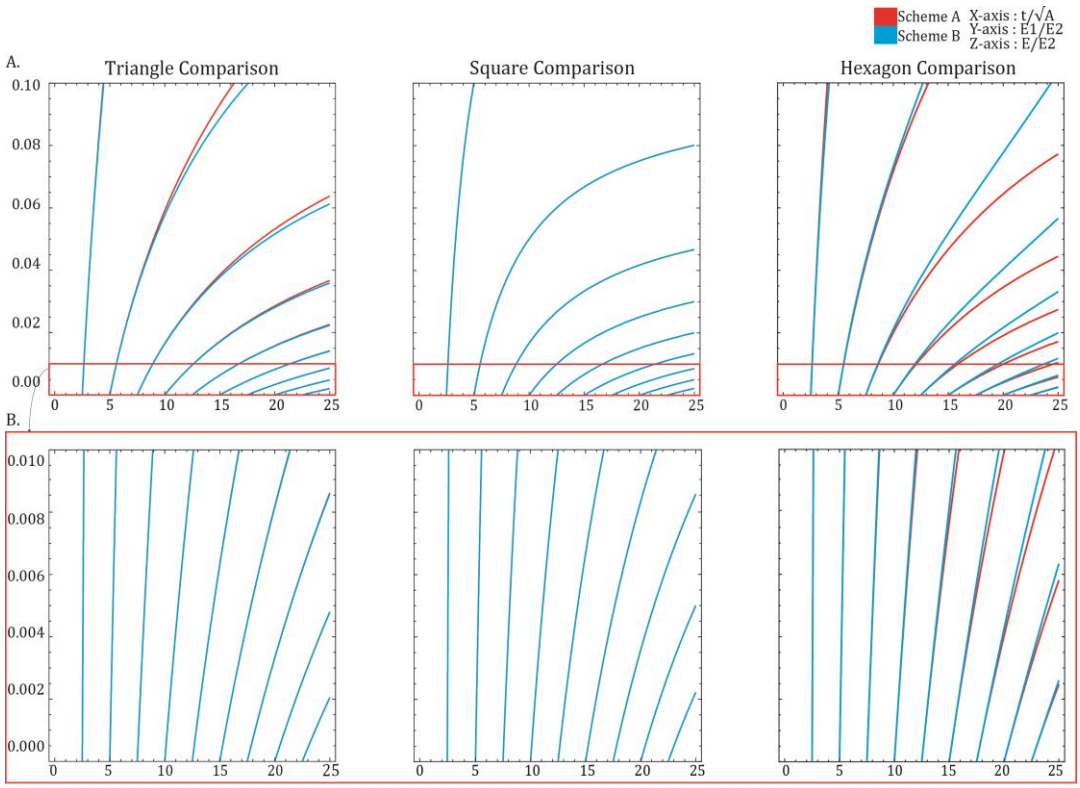

Figure A.5: Comparison of REM contour lines for the two partition schemes shown in Fig. A.4. Overlap of red and blue lines represents strong agreement of the results of the two schemes; correspondence is particularly high in the biological region of interest (bottom row), where joints are very thin.

The effective modulus calculations for Schemes A and B are compared with each other by overlaying both schemes' contour lines (Figure A.5). The further apart two comparable contour lines are (i.e. when both blue and red lines are visible), the more different the results generated by the schemes. There is little difference between the two schemes with regard to REM, particularly for biologically relevant values (lower graphs, marked in red). Differences are most pronounced for very thick joints for hexagon and triangle tiles (upper graphs); this is due to the corner regions in the oblique elements (e.g. Section 1 of triangle and hexagon), marked in red in Figure A.4, which can be considered either as pure in-series elements (Reuss) or off-axis elements (hybrid Reuss-Voigt; see 2. Methods).

6. Effect of area fraction on relative effective modulus of all shapes

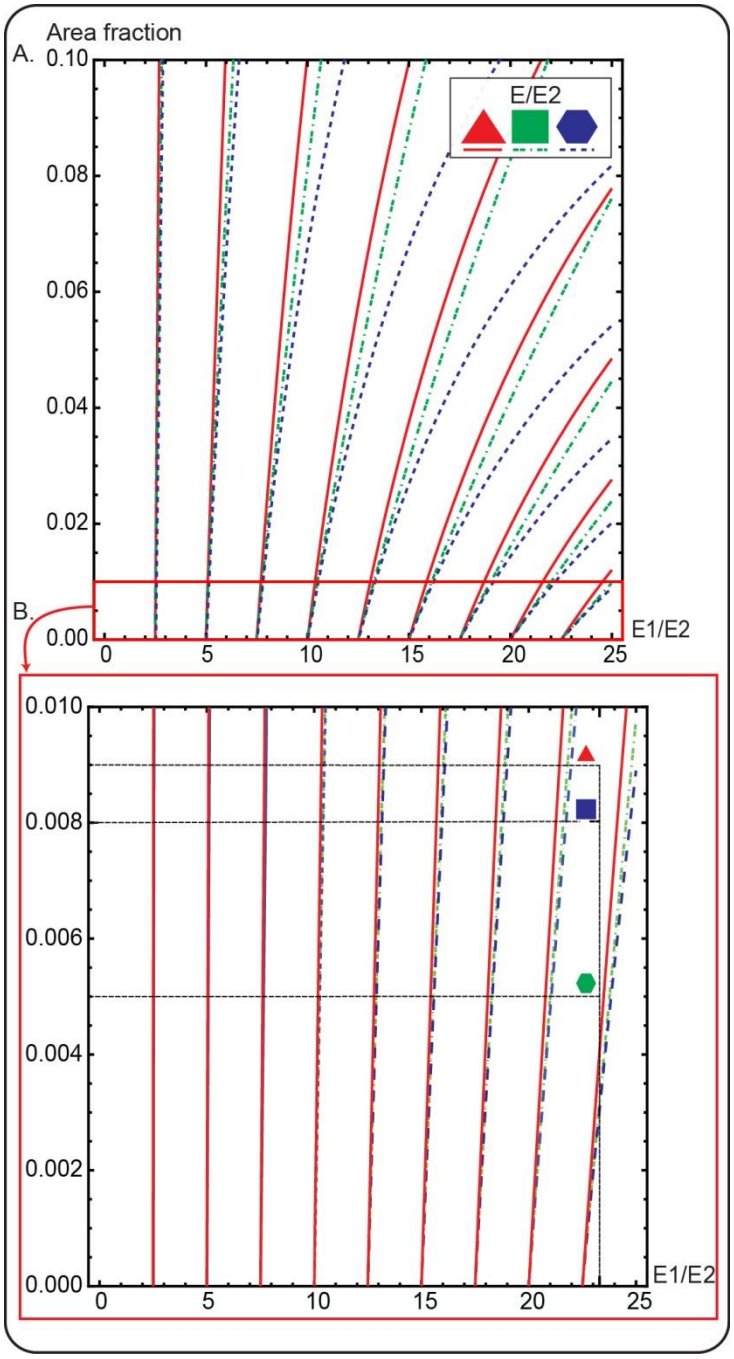

Figure A.6: Comparison of relative effective modulus for all shapes with respect to area fraction (y-axis). Differences in REM among unit cell shapes are less pronounced than when $t/\sqrt{A}$ is held constant (compare with Figure 4).

7. Verification and Experimental methods

The verification procedure for the derived analytical equations was performed using finite element analysis (FEA). The tiling network is modeled in the CAD software Rhino,

using the Grasshopper plugin for parameterized modelling. Since the structure of the tiling network is complex (e.g. the joints are very thin compared tiles and would require a fine meshing to capture their performance), modeling a large tiled network would demand considerable computational power and time. We overcame this by using Periodic Boundary Conditions (PBC) (Li et al., 2013; Overvelde and Bertoldi, 2014), sets of equations to model large systems by breaking them into small parts (representative volume elements RVE; Fig. A.7) that can be repeated periodically over the space to approximate the larger network. Since RVEs are identical in terms of structural and material properties, their responses to the acting forces are the same.

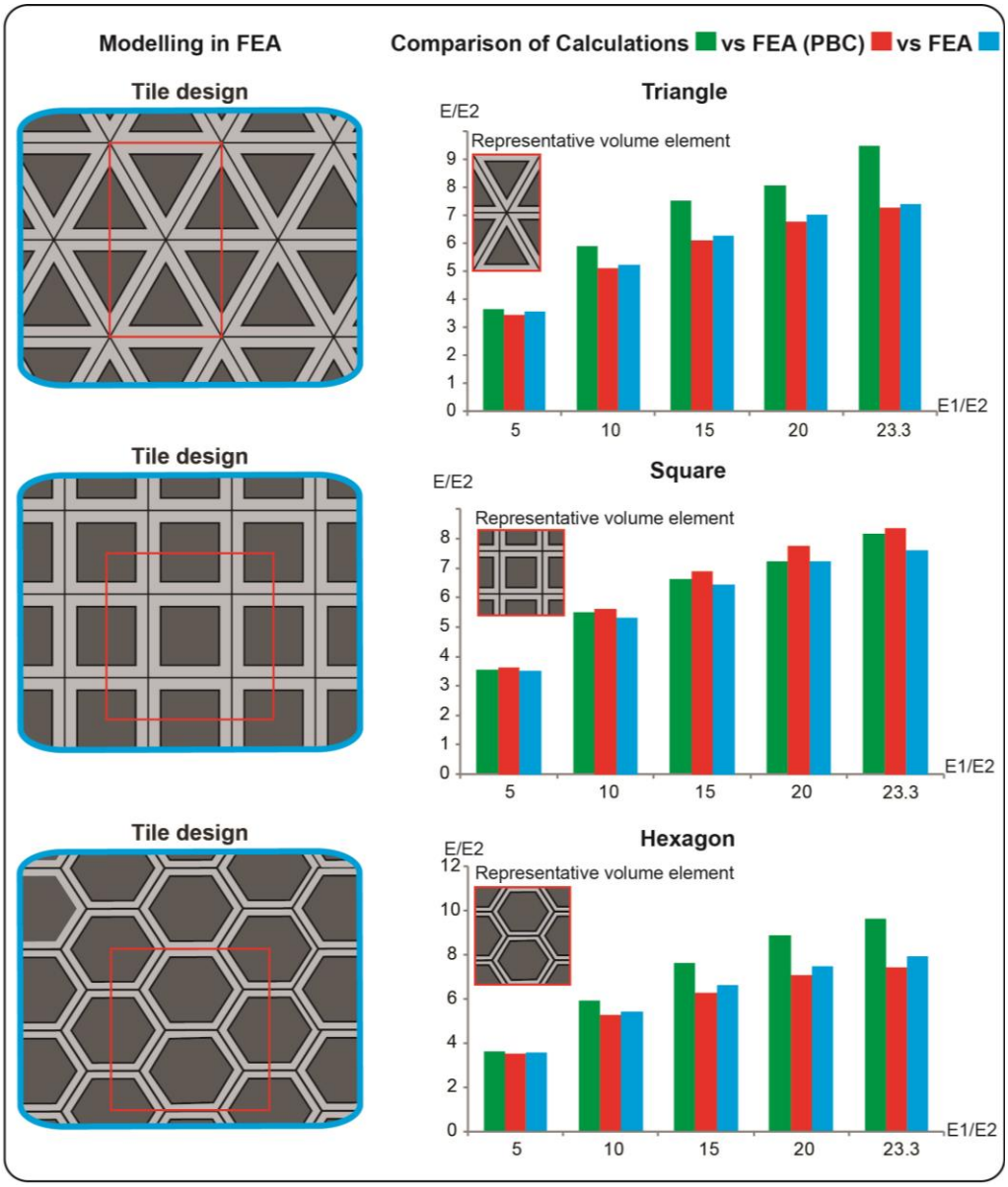

Figure A.7: Comparison of relative effective modulus (E/E2) between analytical calculations, FEA (using periodic boundary conditions) and FEA (tiled array) with E1/E2 on x-axis and E/E2 on y-axis, for $t/\sqrt{A}$ ~0.07.

In our models, a 2-dimensional RVE (with biologically relevant morphology, $t/\sqrt{A}$ = 0.07) was modeled for hexagon, square and triangle tilings using Rhino and Grasshopper. RVEs were imported into ABAQUS (FEA) software and simulations performed for simple compression (1% strain) of the models, with PBCs applied via a readily available PYTHON code (Overvelde and Bertoldi, 2014). Models were tested over a range of E1/E2 values (Fig. A.7), from E1/E2 = 5.0 to 23.3, the biologically relevant tile to joint material stiffness ratio. Each composite model's stiffness was measured as the ratio between the average stress (Total Reaction Force on the boundary / RVE side length) and the average strain (the 1% imposed to the RVE). A uniform joint material property ($E2^{0^\circ}$ = 1500 MPa) was used (i.e. with loading orientation having no effect on joint modulus), as orientation-dependent material properties are beyond the scope of the current paper.

8. Summary

Triangle	Square	Hexagon
Area of the composite $\frac{\sqrt{3}}{4}*(L+2*\frac{t}{0.57})^2$	**Area of the composite** $(L+2*t)^2$	**Area of the composite** $\frac{3\sqrt{3}}{2}*(L+\frac{t}{0.86})^2$
Area of the tile $\frac{\sqrt{3}}{4}*L^2$	**Area of the tile** L^2	**Area of the tile** $\frac{3\sqrt{3}}{2}*L^2$

<table>
<tr>
<td>Area of the joint

$3*(2*L+\frac{t}{0.57})*t/2$</td>
<td>Area of the joint

$(L+2*t)^2 - L^2$</td>
<td>Area of the joint

$3*t*(2*L+\frac{t}{0.86})$</td>
</tr>
<tr>
<td>Perimeter

<table><tr><td>Tile</td><td>3*L</td></tr><tr><td>Composite</td><td>$3*(L+2*\frac{t}{0.57})$</td></tr></table></td>
<td>Perimeter

<table><tr><td>Tile</td><td>4*L</td></tr><tr><td>Composite</td><td>4*(L+ 2 * t)</td></tr></table></td>
<td>Perimeter

<table><tr><td>Tile</td><td>6*L</td></tr><tr><td>Composite</td><td>$6*(L+\frac{t}{0.86})$</td></tr></table></td>
</tr>
<tr>
<td>Area fraction:
<u>Area of tile</u>
Area of composite

$\frac{L^2}{(L+2*\frac{t}{0.57})^2}$</td>
<td>Area fraction:
<u>Area of tile</u>
Area of composite

$\frac{L^2}{(L+2*t)^2}$</td>
<td>Area fraction:
<u>Area of tile</u>
Area of composite

$\frac{L^2}{(L+\frac{t}{0.86})^2}$</td>
</tr>
</table>

Table A.1: Summary of structural parameters and their formulae for all tile shapes.

9. Mesh sensitivity analysis

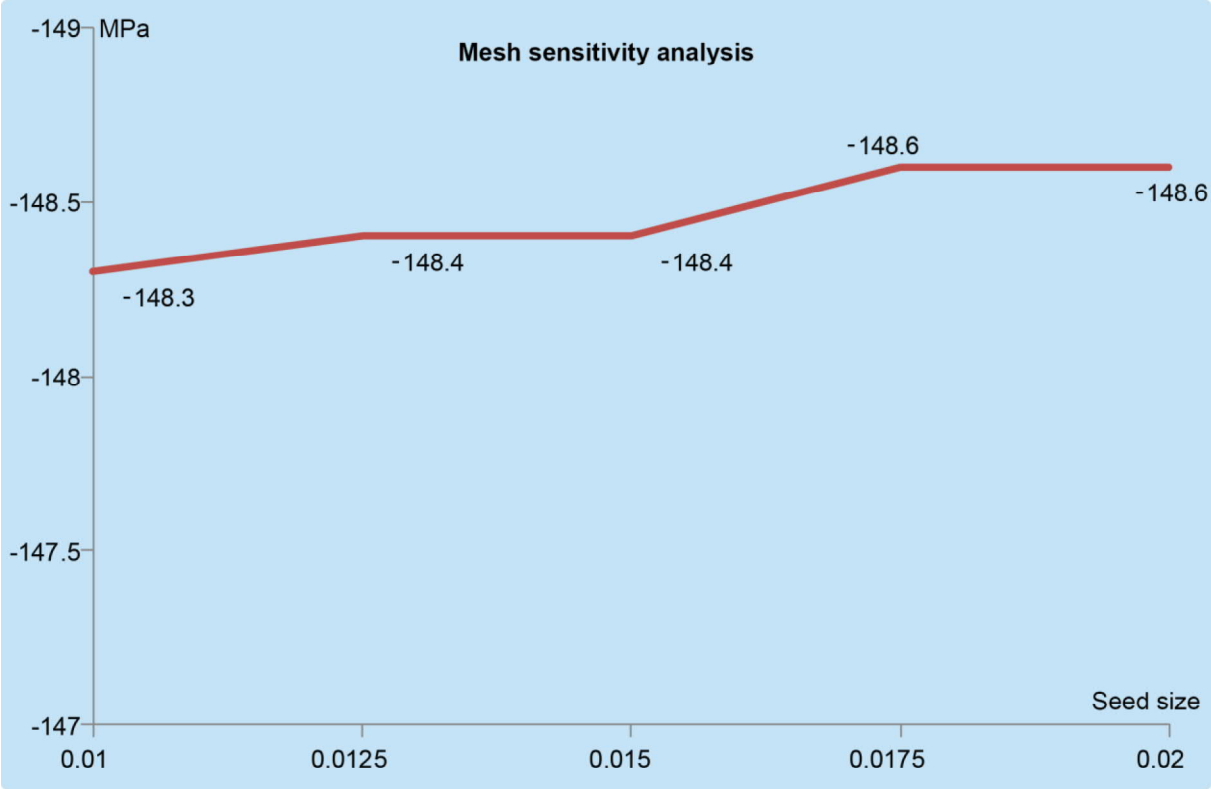

Figure A.8: The Syy stress values are plotted in y-axis against various seed size in x-axis.

Mesh sensitivity analysis is performed to check the effect of seed size on average stress measured in the models. The volume average stress was calculated and it is explained in methods section. The plot of the volume averaged stress is shown below (Fig. A.1). When the seed size was decreased from 0.02 by an interval of 0.015 until 0.01 the stress values changed from -148.6 to -148.3. The decrease of stress by 0.2% is acceptable approximation and seed size of 0.015 is used such that the models use reasonable amount of computational time.

10. Absence of center

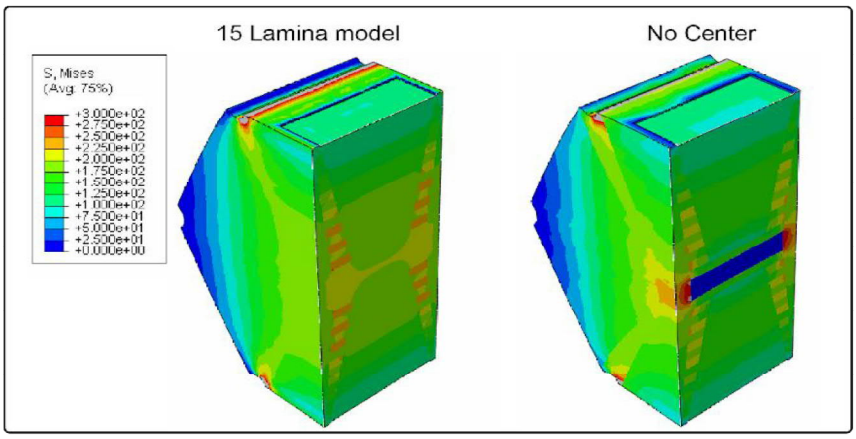

Figure A.9: The stress contours are comparable in the model with center and no center. The center plays no mechanical significance in tesserae stiffness.

To verify the effect of center on ultrastructural mechanics a 15 lamina model was used and the center region was assigned with a material property ~0 MPa. This enables us to simulate tessera without any center. The effective modulus of the whole tesserae was calculated and it was observed that the tesserae model with no center is 26.1 GPa. From the stress contour values (Von Mises) one can observe that there are similar stress contours in the tessera. In the absence of the center in the tesserae the stresses are taken up by the perichondral and chondral region. So all the stresses are funneled by the spokes through the center, and it is being filled with cells may act as mechanical sensors for collecting the loading information within the tesserae.

11. Homogeneous model

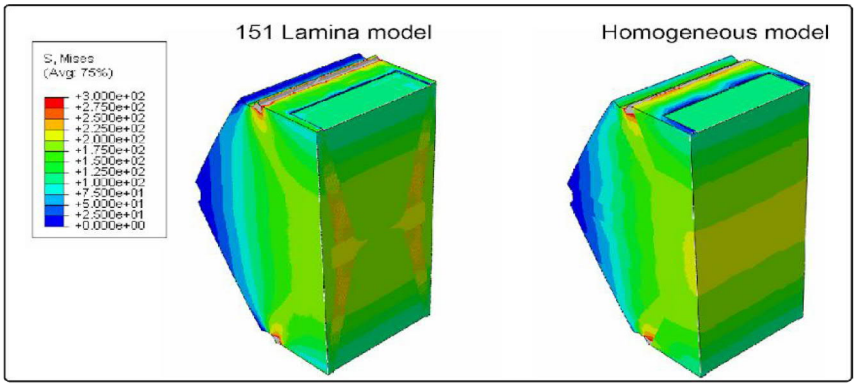

Figure A.10: Von Mises of 151 lamina model vs Homogeneous model. There are high stresses at the center in homogeneous model which may lead to damage of cells in the center. The laminas help in transferring stress through the center and prevent cracks in the spokes.

The effective modulus calculated from the 151 lamina model (26.1 GPa) was assigned to all the ultrastructural regions and FEA was performed as discussed in the methods section. We can observe from the 151 lamina models helps in mitigating high stresses at the center region and protecting the cells from damage. The maximum stresses occur in spoke regions and homogeneous material aids in crack propagation. And the alternating laminas prevent crack propagation and also transfers stress through the center.

And it is very evident from the homogeneous models that the laminas play a crucial role in funneling the stresses through the center and the alternating laminas prevent crack propagation.

12. OGDEN coefficients

The material coefficients used to model the joint material are listed in table below. The material model was built by combining the stress-strain values of tendon in tension (Maganaris and Paul, 1999) and mucosa in compression (Chen et al., 2015b). The ABAQUS material editor has a library of hyperelastic material models which can be used to generate the coefficients for the stress-strain data.

μ1	α1	μ2	α2	D1	D2
0.497324729	7.40136068	-0.426810081	1.76390678	2.33119738	0

Table A.2: Coefficients of Ogden 2nd order hyperelastic material model.

References

Achrai, B., Wagner, H.D., 2013a. Micro-structure and mechanical properties of the turtle carapace as a biological composite shield. Acta Biomaterialia 9, 5890-5902.

Achrai, B., Wagner, H.D.J.A.b., 2013b. Micro-structure and mechanical properties of the turtle carapace as a biological composite shield. 9, 5890-5902.

Ashby, M., Gibson, L., Wegst, U., Olive, R., 1995. The mechanical properties of natural materials. I. Material property charts, Proceedings of the Royal Society of London A: Mathematical, Physical and Engineering Sciences. The Royal Society, pp. 123-140.

Aspden, R.M., 1988. The theory of fiber-reinforced composite-materials applied to changes in the mechanical-properties of the cervix during pregnancy. J Theor Biol 130, 213-221.

Atake, O.J., Cooper, D.M.L., Eames, B.F., 2019. Bone-like features in skate suggest a novel elasmobranch synapomorphy and deep homology of trabecular mineralization patterns. Acta Biomater. 84, 424-436.

Atkins, A., Dean, M.N., Habegger, M.L., Motta, P.J., Ofer, L., Repp, F., Shipov, A., Weiner, S., Currey, J.D., Shahar, R., 2014. Remodeling in bone without osteocytes: Billfish challenge bone structure–function paradigms. Proceedings of the National Academy of Sciences 111, 16047-16052.

Balaban, J.P., Summers, A.P., Wilga, C.A., 2014. Mechanical properties of the hyomandibula in four shark species. J. Exp. Zool. A Ecol. Genet. Physiol. 323, 1-9.

Balaban, J.P., Summers, A.P., Wilga, C.A., 2015. Mechanical properties of the hyomandibula in four shark species. Journal of Experimental Zoology Part A: Ecological Genetics and Physiology 323, 1-9.

Barthelat, F., Zhu, D.J., 2011. A novel biomimetic material duplicating the structure and mechanics of natural nacre. Journal of Materials Research 26, 1203-1215.

Baum, D., Weaver, J.C., Zlotnikov, I., Knötel, D., Tomholt, L., Dean, M.N., 2019. High--throughput segmentation of tiled biological structures using random walk distance transforms. Integr. Comp. Biol. In review.

Bayuk, I.O., Gay, J.K., Hooper, J.M., Chesnokov, E.M., 2008. Upper and lower stiffness bounds for porous anisotropic rocks. Geophysical Journal International 175, 1309-1320.

Boots, B., Okabe, A., Sugihara, K.J.G.i.s., 1999. Spatial tessellations. 1, 503-526.

Bruet, B.J., Song, J., Boyce, M.C., Ortiz, C., 2008. Materials design principles of ancient fish armour. Nat Mater 7, 748-756.

Cadman, J., Chang, C.-C., Chen, J., Chen, Y., Zhou, S., Li, W., Li, Q., 2013. Bioinspired lightweight cellular materials-Understanding effects of natural variation on mechanical properties. Materials Science and Engineering: C 33, 3146-3152.

Carter, D.R., Hayes, W.C., 1977. The compressive behavior of bone as a two-phase porous structure. The Journal of Bone & Joint Surgery 59, 954-962.

Chang, W., 2018a. Application of Tessellation in Architectural Geometry Design, E3S Web of Conferences. EDP Sciences, p. 03015.

Chang, W.J.E.S.W.C., 2018b. Application of Tessellation in Architectural Geometry Design. 38, 03015.

Charbonnier, M.-C., Cammas, C., 2016. Micromorphological analysis of roman roads functioning: Evidence of rhythms of human trampling and vehicle traffic (Northeast of France), World Archaeological Congress WAC-8, Kyoto, Japan.

Chen, C., Tambe, D.T., Deng, L., Yang, L., 2013. Biomechanical properties and mechanobiology of the articular chondrocyte. Am. J. Physiol. Cell Physiol. 305, C1202-1208.

Chen, I.H., Yang, W., Meyers, M.A., 2014. Alligator osteoderms: Mechanical behavior and hierarchical structure. Materials Science and Engineering: C 35, 441-448.

Chen, I.H., Yang, W., Meyers, M.A., 2015a. Leatherback sea turtle shell: A tough and flexible biological design. Acta Biomater 28, 2-12.

Chen, J., Ahmad, R., Li, W., Swain, M., Li, Q., 2015b. Biomechanics of oral mucosa. J. R. Soc. Interface 12, 20150325.

Chen, J., Chen, L., Chang, C.-C., Zhang, Z., Li, W., Swain, M.V., Li, Q., 2017. Micro-CT based modelling for characterising injection-moulded porous titanium implants. Int. j. numer. method. biomed. eng. 33.

Chon, M.J., Daly, M., Wang, B., Xiao, X., Zaheri, A., Meyers, M.A., Espinosa, H.D.J.J.o.t.m.b.o.b.m., 2017. Lamellae spatial distribution modulates fracture behavior and toughness of african pangolin scales. 76, 30-37.

Clement, J., 1992a. Re-examination of the fine structure of endoskeletal mineralization in Chondrichthyans: implications for growth, ageing and calcium homeostasis. Marine and Freshwater Research 43, 157-181.

Clement, J.G., 1992b. Re-examination of the fine structure of endoskeletal mineralization in chondrichthyans: implications for growth, ageing and calcium homeostasis. Aust. J. Mar. Freshw. Res. 43, 157-181.

Currey, J.D., 1988. The effect of porosity and mineral content on the Young's modulus of elasticity of compact bone. Journal of Biomechanics 21, 131-139.

Damiens, R., Rhee, H., Hwang, Y., Park, S., Hammi, Y., Lim, H., Horstemeyer, M., 2012. Compressive behavior of a turtle's shell: experiment, modeling, and simulation. Journal of the mechanical behavior of biomedical materials 6, 106-112.

Dean, M., Schaefer, J., 2005. Patterns of growth and mineralization in elasmobranch cartilage, FASEB JOURNAL. FEDERATION AMER SOC EXP BIOL 9650 ROCKVILLE PIKE, BETHESDA, MD 20814-3998 USA, pp. A247-A247.

Dean, M.N., 2009. Ontogeny, morphology and mechanics of the tessellated skeleton of cartilaginous fishes. University of California, Irvine.

Dean, M.N., Bizzarro, J.J., Clark, B., Underwood, C.J., Johanson, Z., 2017a. Large batoid fishes frequently consume stingrays despite skeletal damage. Royal Society open science 4, 170674.

Dean, M.N., Bizzarro, J.J., Clark, B., Underwood, C.J., Johanson, Z., 2017b. Large batoid fishes frequently consume stingrays despite skeletal damage. Royal Society Open Science 4, 170674-170611.

Dean, M.N., Ekstrom, L., Monsonego-Ornan, E., Ballantyne, J., Witten, P.E., Riley, C., Habraken, W., Omelon, S., 2015. Mineral homeostasis and regulation of mineralization processes in the skeletons of sharks, rays and relatives (Elasmobranchii). Semin. Cell Dev. Biol. 46, 51-67.

Dean, M.N., Mull, C.G., Gorb, S.N., Summers, A.P., 2009a. Ontogeny of the tessellated skeleton: insight from the skeletal growth of the round stingray Urobatis halleri. J. Anat. 215, 227-239.

Dean, M.N., Mull, C.G., Gorb, S.N., Summers, A.P., 2009b. Ontogeny of the tessellated skeleton: insight from the skeletal growth of the round stingray Urobatis halleri. J Anat 215, 227-239.

Dean, M.N., Seidel, R., Knoetel, D., Lyons, K., Baum, D., Weaver, J., Fratzl, P., 2016. To build a shark-3D tiling laws of tessellated cartilage. Integrative and Comparative Biology pp. E50–E50.

Dean, M.N., Socha, J.J., Hall, B.K., Summers, A.P., 2010. Canaliculi in the tessellated skeleton of cartilaginous fishes. J. Appl. Ichthyol. 26, 263-267.

Dean, M.N., Wilga, C.D., Summers, A.P., 2005. Eating without hands or tongue: specialization, elaboration and the evolution of prey processing mechanisms in cartilaginous fishes. Biology Letters 1, 357-361.

Deger, K.O., Deger, A.H.J.P.-S., Sciences, B., 2012. An application of mathematical tessellation method in interior designing. 51, 249-256.

Dingerkus, G., Seret, B., 1991. Multiple prismatic calcium phosphate layers in the jaws of present-day sharks (Chondrichthyes; Selachii). Experientia 47, 38-40.

Fahle, S., Thomason, J., 2008. Measurement of jaw viscoelasticity in newborn and adult lesser spotted dogfish Scyliorhinus canicula (L., 1758). Journal of Fish Biology 72, 1553-1557.

Ferrara, T., Clausen, P., Huber, D., McHenry, C., Peddemors, V., Wroe, S., 2011a. Mechanics of biting in great white and sandtiger sharks. Journal of biomechanics 44, 430-435.

Ferrara, T.L., Boughton, P., Slavich, E., Wroe, S.J.P.o., 2013. A Novel Method for Single Sample Multi-Axial Nanoindentation of Hydrated Heterogeneous Tissues Based on Testing Great White Shark Jaws. 8, e81196.

Ferrara, T.L., Clausen, P., Huber, D.R., McHenry, C.R., Peddemors, V., Wroe, S., 2011b. Mechanics of biting in great white and sandtiger sharks. J. Biomech. 44, 430-435.

Fratzl, P., Gupta, H.S., Fischer, F.D., Kolednik, O., 2007a. Hindered crack propagation in materials with periodically varying Young's modulus—lessons from biological materials. Advanced Materials 19, 2657-2661.

Fratzl, P., Gupta, H.S., Fischer, F.D., Kolednik, O., 2007b. Hindered crack propagation in materials with periodically varying Young's modulus—Lessons from biological materials. Adv. Mater. 19, 2657-2661.

Fratzl, P., Kolednik, O., Fischer, F.D., Dean, M.N., 2016a. The mechanics of tessellations–bioinspired strategies for fracture resistance. Chemical Society Reviews 45, 252-267.

Fratzl, P., Kolednik, O., Fischer, F.D., Dean, M.N., 2016b. The mechanics of tessellations - bioinspired strategies for fracture resistance. Chem. Soc. Rev. 45, 252-267.

Gao, C., Hasseldine, B.P.J., Li, L., Weaver, J.C., Li, Y., 2018. Amplifying Strength, Toughness, and Auxeticity via Wavy Sutural Tessellation in Plant Seedcoats. Adv Mater 30, e1800579.

Gao, C., Li, Y., 2019. Mechanical model of bio-inspired composites with sutural tessellation. Journal of the Mechanics and Physics of Solids 122, 190-204.

Grunbaum, B., Shephard, G.C., 1977. Tilings by Regular Polygons. Mathematics Magazine 50, 227-247.

Gupta, H., Schratter, S., Tesch, W., Roschger, P., Berzlanovich, A., Schoeberl, T., Klaushofer, K., Fratzl, P., 2005. Two different correlations between nanoindentation modulus and mineral content in the bone–cartilage interface. Journal of Structural Biology 149, 138-148.

Hasseldine, B.P.J., Gao, C., Collins, J.M., Jung, H.D., Jang, T.S., Song, J., Li, Y., 2017. Mechanical response of common millet (Panicum miliaceum) seeds under quasi-static compression: Experiments and modeling. J Mech Behav Biomed Mater 73, 102-113.

Hosseini, M., Garner, S., Naleway, S., McKittrick, J., 2018. Role of Architecture in Controlling Crack Propagation Direction Bio-Inspired From Boxfish Scute.

Hull, D., Clyne, T.W., 1996. An introduction to composite materials, 2nd ed. Cambridge University Press, Cambridge ; New York.

Jayasankar, A.K., Seidel, R., Naumann, J., Guiducci, L., Hosny, A., Fratzl, P., Weaver, J.C., Dunlop, J.W.C., Dean, M.N., 2017a. Mechanical behavior of idealized, stingray-skeleton-inspired tiled composites as a function of geometry and material properties. Journal of the Mechanical Behavior of Biomedical Materials 73, 86-101.

Kemp, N., Westrin, S.K., 1979a. Ultrastructure of calcified cartilage in the endoskeletal tesserae of sharks. J. Morphol. 160, 75-101.

Kemp, N.E., Westrin, S.K., 1979b. Ultrastructure of calcified cartilage in the endoskeletal tesserae of sharks. Journal of Morphology 160, 75-101.

Khaira, J.J.Y.S.J., 2009. What are Tilings and Tessellations and how are they used in Architecture? 2, 35.

Knötel, D., Seidel, R., Prohaska, S., Dean, M.N., Baum, D., 2017. Automated segmentation of complex patterns in biological tissues: Lessons from stingray tessellated cartilage. PLoS One 12, e0188018-0188024.

Kolednik, O., Predan, J., Fischer, F.D., Fratzl, P., 2011. Bioinspired Design Criteria for Damage-Resistant Materials with Periodically Varying Microstructure. Adv. Funct. Mater. 21, 3634-3641.

Kolmann, M.A., Huber, D.R., Motta, P.J., Grubbs, R.D., 2015. Feeding biomechanics of the cownose ray, Rhinoptera bonasus, over ontogeny. Journal of anatomy 227, 341-351.

Krauss, S., Monsonego-Ornan, E., Zelzer, E., Fratzl, P., Shahar, R., 2009a. Mechanical Function of a Complex Three-Dimensional Suture Joining the Bony Elements in the Shell of the Red-Eared Slider Turtle. 21, 407-412.

Krauss, S., Monsonego-Ornan, E., Zelzer, E., Fratzl, P., Shahar, R., 2009b. Mechanical function of a complex three-dimensional suture joining the bony elements in the shell of the red-eared slider turtle. Advanced Materials 21, 407-412.

Krenchel, H., 1964. Fibre Reinforcement: Theoretical and Practical Investigations of the Elasticity and Strength of Fibre-reinforced Materials. Akademisk Forlag, Copenhagen.

Lammi, M.J., 2004. Current perspectives on cartilage and chondrocyte mechanobiology. Biorheology 41, 593-596.

Leydig, F., 1857. Lehrbuch der Histologie des Menschen und der Thiere.

Li, Y., Ortiz, C., Boyce, M.C., 2011. Stiffness and strength of suture joints in nature. Phys Rev E Stat Nonlin Soft Matter Phys 84, 062904.

Li, Y., Ortiz, C., Boyce, M.C., 2012. Bioinspired, mechanical, deterministic fractal model for hierarchical suture joints. Phys Rev E Stat Nonlin Soft Matter Phys 85, 031901.

Li, Y., Ortiz, C., Boyce, M.C., 2013. A generalized mechanical model for suture interfaces of arbitrary geometry. J Mech Phys Solids 61, 1144-1167.

Lin, E., Li, Y., Ortiz, C., Boyce, M.C., 2014a. 3D printed, bio-inspired prototypes and analytical models for structured suture interfaces with geometrically-tuned deformation and failure behavior. Journal of the Mechanics and Physics of Solids 73, 166-182.

Lin, E., Li, Y.N., Weaver, J.C., Ortiz, C., Boyce, M.C., 2014b. Tunability and enhancement of mechanical behavior with additively manufactured bio-inspired hierarchical suture interfaces. Journal of Materials Research 29, 1867-1875.

Liu, X., Dean, M.N., Summers, A.P., Earthman, J.C., 2010a. Composite model of the shark's skeleton in bending: A novel architecture for biomimetic design of functional compression bias. Materials Science and Engineering: C 30, 1077-1084.

Liu, X., Dean, M.N., Summers, A.P., Earthman, J.C., 2010b. Composite model of the shark's skeleton in bending: A novel architecture for biomimetic design of functional compression bias. Mater. Sci. Eng. C 30, 1077-1084.

Liu, X., Dean, M.N., Youssefpour, H., Summers, A.P., Earthman, J.C., 2014a. Stress relaxation behavior of tessellated cartilage from the jaws of blue sharks. J Mech Behav Biomed Mater 29, 68-80.

Liu, X., Dean, M.N., Youssefpour, H., Summers, A.P., Earthman, J.C., 2014b. Stress relaxation behavior of tessellated cartilage from the jaws of blue sharks. J. Mech. Behav. Biomed. Mater. 29, 68-80.

Liu, Z., Jiao, D., Weng, Z., Zhang, Z., 2016. Structure and mechanical behaviors of protective armored pangolin scales and effects of hydration and orientation. Journal of the mechanical behavior of biomedical materials 56, 165-174.

Long, J.A., Burrow, C.J., Ginter, M., Maisey, J.G., Trinajstic, K.M., Coates, M.I., Young, G.C., Senden, T.J., 2015. First Shark from the Late Devonian (Frasnian) Gogo Formation, Western Australia Sheds New Light on the Development of Tessellated Calcified Cartilage. PLOS ONE 10, e0126066.

Macesic, L.J., Summers, A.P., 2012. Flexural stiffness and composition of the batoid propterygium as predictors of punting ability. J. Exp. Biol. 215, 2003-2012.

Maganaris, C.N., Paul, J.P., 1999. In vivo human tendon mechanical properties. J. Physiol. 521 Pt 1, 307-313.

Maisey, J.G., 2013a. The diversity of tessellated calcification in modern and extinct chondrichthyans. Revue de Paléobiologie, Genève 32, 355-371.

Maisey, J.G.J.R.d.P., 2013b. The diversity of tessellated calcification in modern and extinct chondrichthyans. 32, 355-371.

Marcroft, T.A., 2015. Evolution of the boxfish carapace: functional consequences of shape. UCLA.

Martini, R., Barthelat, F., 2016. Stability of hard plates on soft substrates and application to the design of bioinspired segmented armor. Journal of the Mechanics and Physics of Solids 92, 195-209.

Olson, I.C., Kozdon, R., Valley, J.W., Gilbert, P.U.P.A., 2012. Mollusk Shell Nacre Ultrastructure Correlates with Environmental Temperature and Pressure. Journal of the American Chemical Society 134, 7351-7358.

Overvelde, J.T.B., Bertoldi, K., 2014. Relating pore shape to the non-linear response of periodic elastomeric structures. J Mech Phys Solids 64, 351-366.

Oxman, N., Material-based design computation: Tiling behavior.

Oxman, N., 2010. Material-based design computation. Massachusetts Institute of Technology.

Petrie, C.S., Williams, J.L., 2005. Comparative evaluation of implant designs: influence of diameter, length, and taper on strains in the alveolar crest. A three-dimensional finite-element analysis. Clin. Oral Implants Res. 16, 486-494.

Porter, M.M., Ravikumar, N., Barthelat, F., Martini, R., 2017. 3D-printing and mechanics of bio-inspired articulated and multi-material structures. J Mech Behav Biomed Mater 73, 114-126.

Rees, J., Jacobsen, P., 1997. Elastic modulus of the periodontal ligament. Biomaterials 18, 995-999.

Rhee, H., Horstemeyer, M.F., Hwang, Y., Lim, H., El Kadiri, H., Trim, W., 2009. A study on the structure and mechanical behavior of the *Terrapene carolina* carapace: A pathway to design bio-inspired synthetic composites. Materials Science and Engineering: C 29, 2333-2339.

Rivera, G., Stayton, C.T., 2011. Finite element modeling of shell shape in the freshwater turtle *Pseudemys concinna* reveals a trade-off between mechanical strength and hydrodynamic efficiency. 272, 1192-1203.

Roth, W., 1911. Beiträge zur Kenntnis der Strukturverhältnisse des Selachier-Knorpels. Morphologisches Jahrbuch, 485-555.

Rudykh, S., Ortiz, C., Boyce, M.C., 2015. Flexibility and protection by design: imbricated hybrid microstructures of bio-inspired armor. Soft matter 11, 2547-2554.

Schattschneider, D., Emmer, M., 2003. MC Escher's legacy. Springer.

Seidel, R., Blumer, M., Pechriggl, E.-J., Lyons, K., Hall, B.K., Fratzl, P., Weaver, J.C., Dean, M.N., 2017a. Calcified cartilage or bone? Collagens in the tessellated endoskeletons of cartilaginous fish (sharks and rays). J. Struct. Biol. 200, 54-71.

Seidel, R., Blumer, M., Zaslansky, P., Knötel, D., Huber, D.R., Weaver, J.C., Fratzl, P., Omelon, S., Bertinetti, L., Dean, M.N., 2017b. Ultrastructural, material and crystallographic description of endophytic masses - A possible damage response in shark and ray tessellated calcified cartilage. J. Struct. Biol. 198, 5-18.

Seidel, R., Jayasankar, A.K., Shahar, R., Dean, M.N., 2019a. The Multiscale Architectures of Fish Bone and Tessellated Cartilage and Their Relation to Function, in: Estrin, Y., Bréchet, Y., Dunlop, J., Fratzl, P. (Eds.), Architectured Materials in Nature and Engineering: Archimats. Springer International Publishing, Cham, pp. 329-353.

Seidel, R., Jayasankar, A.K., Shahar, R., Dean, M.N., 2019b. The multiscale architectures of fish bone and tessellated cartilage and their relation to function, in: Estrin, Y., Bréchet, Y.,

Dunlop, J., Fratzl, P. (Eds.), Architectured Materials in Nature and Engineering, pp. 329-353.

Seidel, R., Knötel, D., Baum, D., Weaver, J.C., Dean, M.N., 2014. Material and structural characterization of mineralized elasmobranch cartilage–lessons in repeated tiling patterns in mechanically loaded 3D objects.

Seidel, R., Lyons, K., Blumer, M., Zaslansky, P., Fratzl, P., Weaver, J.C., Dean, M.N., 2016a. Ultrastructural and developmental features of the tessellated endoskeleton of elasmobranchs (sharks and rays). Journal of Anatomy 229, 681-702.

Seidel, R., Lyons, K., Blumer, M., Zaslansky, P., Fratzl, P., Weaver, J.C., Dean, M.N., 2016b. Ultrastructural and developmental features of the tessellated endoskeleton of elasmobranchs (sharks and rays). J. Anat. 229, 681-702.

Seidel, R., Roschger, A., Li, L., Zhang, Q., Yin, J., Yang, T., Weaver, J.C., Fratzl, P., Roschger, P., Dean, M.N., 2019c. Mechanical properties of stingray tesserae: High-resolution correlative analysis of mineral density and indentation moduli in tessellated cartilage. Acta Biomater. In review.

Sih, G.C., Macdonald, B., 1974. Fracture mechanics applied to engineering problems-strain energy density fracture criterion. Eng. Fract. Mech. 6, 361-386.

Soto, Á.D.C., 2009. Ecuaciones cohomológicas sobre espacios de embaldosados. Universidad de Chile.

Spearman, R.I.C., 1967. On the nature of the horny scales of the pangolin. 46, 267-273.

Studart, A.R., 2012. Towards high-performance bioinspired composites. Adv Mater 24, 5024-5044.

Summers, A.P., 2000a. Stiffening the stingray skeleton—An investigation of durophagy in myliobatid stingrays (Chondrichthyes, Batoidea, Myliobatidae). J. Morphol. 243, 113-126.

Summers, A.P., 2000b. Stiffening the stingray skeleton - an investigation of durophagy in myliobatid stingrays (Chondrichthyes, batoidea, myliobatidae). J Morphol 243, 113-126.

Summers, A.P., Ketcham, R., Rowe, T., 2004. Structure and function of the horn shark (Heterodontus francisi) cranium through ontogeny - the development of a hard prey specialist. J. Morphol. 260, 1-12.

Summers, A.P., Koob, T.J., Brainerd, E.L., 1998. Stingray jaws strut their stuff. Nature 395, 450-451.

Van Wassenbergh, S., van Manen, K., Marcroft, T.A., Alfaro, M.E., Stamhuis, E.J., 2015. Boxfish swimming paradox resolved: forces by the flow of water around the body promote manoeuvrability. J R Soc Interface 12.

Vernerey, F.J., Barthelat, F., 2010. On the mechanics of fishscale structures. International Journal of Solids and Structures 47, 2268-2275.

Vernerey, F.J., Barthelat, F.J.J.o.t.M., Solids, P.o., 2014. Skin and scales of teleost fish: Simple structure but high performance and multiple functions. 68, 66-76.

Wang, B., Yang, W., Sherman, V.R., Meyers, M.A., 2016a. Pangolin armor: overlapping, structure, and mechanical properties of the keratinous scales. Acta biomaterialia 41, 60-74.

Wang, B., Yang, W., Sherman, V.R., Meyers, M.A.J.A.b., 2016b. Pangolin armor: overlapping, structure, and mechanical properties of the keratinous scales. 41, 60-74.

Wang, L.F., Lau, J., Thomas, E.L., Boyce, M.C., 2011. Co-continuous composite materials for stiffness, strength, and energy dissipation. Adv Mater 23, 1524-1529.

Wann, A.K.T., Zuo, N., Haycraft, C.J., Jensen, C.G., Poole, C.A., McGlashan, S.R., Knight, M.M., 2012. Primary cilia mediate mechanotransduction through control of ATP-induced Ca2+ signaling in compressed chondrocytes. The FASEB Journal 26, 1663-1671.

Wegst, U.G.K., Ashby, M.F., 2004a. The mechanical efficiency of natural materials. Philos. Mag. 84, 2167-2186.

Wegst, U.G.K., Ashby, M.F., 2004b. The mechanical efficiency of natural materials. Philosophical Magazine 84, 2167-2186.

Wilga, C.A.D., Diniz, S.E., Steele, P.R., Sudario-Cook, J., Dumont, E.R., Ferry, L.A., 2016a. Ontogeny of Feeding Mechanics in Smoothhound Sharks: Morphology and Cartilage Stiffness. Integrative and Comparative Biology 56, 442-448.

Wilga, C.A.D., Diniz, S.E., Steele, P.R., Sudario-Cook, J., Dumont, E.R., Ferry, L.A., 2016b. Ontogeny of feeding mechanics in smoothhound sharks: Morphology and cartilage stiffness. Integr. Comp. Biol. 56, 442-448.

Wilga, C.D., Motta, P.J., 2000. Durophagy in sharks: feeding mechanics of the hammerhead Sphyrna tiburo. J Exp Biol 203, 2781-2796.

Wroe, S., Huber, D., Lowry, M., McHenry, C., Moreno, K., Clausen, P., Ferrara, T., Cunningham, E., Dean, M., Summers, A., 2008a. Three-dimensional computer analysis of white shark jaw mechanics: how hard can a great white bite? Journal of Zoology 276, 336-342.

Wroe, S., Huber, D.R., Lowry, M., McHenry, C., Moreno, K., Clausen, P., Ferrara, T.L., Cunningham, E., Dean, M.N., Summers, A.P., 2008b. Three-dimensional computer analysis of white shark jaw mechanics: how hard can a great white bite? J. Zool. 276, 336-342.

Wu, Q.Q., Chen, Q., 2000. Mechanoregulation of chondrocyte proliferation, maturation, and hypertrophy: ion-channel dependent transduction of matrix deformation signals. Exp. Cell Res. 256, 383-391.

Yamashita, M., Gotoh, M.J.I.J.o.I.E., 2005. Impact behavior of honeycomb structures with various cell specifications—numerical simulation and experiment. 32, 618-630.

Yang, S.Y., O'Cearbhaill, E.D., Sisk, G.C., Park, K.M., Cho, W.K., Villiger, M., Bouma, B.E., Pomahac, B., Karp, J.M., 2013a. A bio-inspired swellable microneedle adhesive for mechanical interlocking with tissue. Nat Commun 4, 1702.

Yang, W., Chen, I.H., Gludovatz, B., Zimmermann, E.A., Ritchie, R.O., Meyers, M.A., 2013b. Natural flexible dermal armor. Advanced Materials 25, 31-48.

Yang, W., Chen, I.H., McKittrick, J., Meyers, M.A., 2012. Flexible Dermal Armor in Nature. Jom 64, 475-485.

Yang, W., Naleway, S.E., Porter, M.M., Meyers, M.A., McKittrick, J., 2015. The armored carapace of the boxfish. Acta Biomater 23, 1-10.

Zhang, W., Soman, P., Meggs, K., Qu, X., Chen, S., 2013a. Tuning the Poisson's Ratio of Biomaterials for Investigating Cellular Response, Adv. Funct. Mater.

Zhang, W., Soman, P., Meggs, K., Qu, X., Chen, S., 2013b. Tuning the Poisson's Ratio of Biomaterials for Investigating Cellular Response. Adv Funct Mater 23, 3226-3232.

Zhang, Y.H., Fu, H.R., Xu, S., Fan, J.A., Hwang, K.C., Jiang, J.Q., Rogers, J.A., Huang, Y.G., 2014. A hierarchical computational model for stretchable interconnects with fractal-inspired designs. Journal of the Mechanics and Physics of Solids 72, 115-130.

Zhu, D., Ortega, C.F., Motamedi, R., Szewciw, L., Vernerey, F., Barthelat, F.J.A.E.M., 2012. Structure and mechanical performance of a “modern” fish scale. 14, B185-B194.

Acknowledgements

The completion of this doctoral thesis would not have been possible with the help of several people, and I would firstly like to thank Dr. Mason Dean. It all started way back in 2015, he gave me this opportunity to pursue my doctoral research, and I am indebted to him. I would like to profusely thank Dr. Dean, providing me with constant encouragement, opportunity and mentoring. He taught me fundamentals of scientific research, right from scratch and always been there to support me for whenever I needed advice and guidance. To summarize in a nutshell, I would give Dr. Dean most of the credit for the kind of scientist I aspire to become.

Thank you, Mason.

Prof. Peter Fratzl, I would like to thank you for providing us such a fantastic work environment with positive vibes and friendly work environment. I want to take this opportunity to express my gratitude for all the fruitful discussions we had and all the insights and perspectives you gave about science. Every meeting with you left an encouraging and positive impact on my thought process, and it did change the way and attitude I had about science.

Thanks a lot, Prof. Fratzl.

I would like to thank Prof. Claudia Fleck for being my supervisor from TU Berlin and providing all the necessary support to facilitate me to graduate my PhD.

"It is the long history of humankind (and animal kind, too) that those who learned to collaborate and improvise most effectively have prevailed." – Charles Darwin.

Collaborations have been a critical aspect of my Ph.D. thesis, and I would like to take this opportunity to thank Dr. Dean for introducing me to several of his collaborators, who immensely helped me to complete my research.

The starting point of my Ph.D. was at Wyss Institute at Harvard University. Under the supervision of Dr. James Weaver, I worked with Ahmed Hosny on learning several modeling techniques, which laid a solid foundation of my thesis. I would like to take this

opportunity to thank both for hosting me for three months in Boston and providing me with adequate skillsets required for my thesis.

Thank you, James and Ahmed.

My first project would not have been realized without the contribution and support from Prof. John Dunlop and Dr. Lorenzo Guiducci. They supported me in understanding the fundamentals and basics of analytical modeling and always there to support me and help me in building and interpreting the data.

Thank you, John and Lorenzo.

On progressing to my second project, I would like to thank Dr. Junning Chen. Junning is a friendly and helpful person, who is always there to support his collaborators. His views on FEA and interpretation of FE data gave me new perspectives on understanding the relevance of mechanical data concerning biology. The trip to Exeter was one of the good experiences I would always cherish.

Thank you Junning.

"Coming together is a beginning, staying together is progress, and working together is the success." – Henry Ford

Working in a friendly group is what always a Ph.D. student strives for.

Dr. Ronald Seidel. Group member, collaborator, and a great friend. Thanks for all the good vibes, conversations about science and all the train talks about the drones. I really had a good learning experience and thanks for being the to-go man for any opinion and advice. I cherish all the good times we had in Klausar and our trip to London.

Thank you, Ronald.

A stressful project sometimes brings the best out of people. One such was the grueling and more demanding trip to DESY, where we had to perform and monitor experiments over a 14-hour window. I realized such times can be more fun when you have group mates like Julia Chaumel, Dr. Chuang Liu and Dr. Shahrouz Amini around. It is always fun to work with you guys, and all your inputs and suggestions regarding my work were towards enhancement and progression.

Thank you, guys.

The following people deserve special mention as they made the work environment livelier, friendly and made me look forward to coming to work. Dr. Anna Pohl has a very positive outlook on everything and took time to help me out with things related to work and outside. She is someone who I always looked up to in times of need, motivation, and encouragement. A good friend, amazing backerin and a nice office mate, anyone, could ever imagine.

Thank you, Anna.

Dr. Bente as well fondly call Dr. Klaas Bente, is another office mate anyone would like to have in their working tenure. Klaas is always up for science, and it is very intriguing to learn the thinking process in solving any problem. Amazing times in Chez brille and pub quiz.

Thank you, Dr. Bente.

Of course, all the other colleagues and friends Felix Bachmann, Jacob Naumann, Dr. Erika Guenther, Franziska Jehle, Dr. Ignacio Rodrigues, and Dr. Cathleen Oschatz thank you guys for all the good times and conversations. I will cherish them.

Thank you, guys.

I would like to thank Dr. Daniel Baum for supporting me with ABAQUS license which is essential for the completion of my Ph.D. I would like to extend my gratitude to Company of Biologists and Dr. Overvelde for providing me with a travel grant lab access and training at AMOLF, The Netherlands.

Lastly, I would like to thank my family. My parents have always been a massive support in every endeavor I pursue. They always nurtured my dreams, passion, morally and financially supported me in pursuit of my education and my goals.

Thank you Appa and Amma for everything.

I also would like to thank my brother and sister in law for supporting my little niece for all the laugh and positive vibes and me. My friends, Srini, DD, Kannan, Bharath and Raveena and friends back home, ever since childhood, thank you guys, one more time.

Thank you, everyone.